Title
A High-order Eulerian-Lagrangian Finite Element Method for Coupled Electro-mechanical Systems

Author
Brandstetter, Gerd

Publication Date
2015

Peer reviewed|Thesis/dissertation

A High-order Eulerian-Lagrangian Finite Element Method for Coupled Electro-mechanical Systems

by

Gerd Brandstetter

A dissertation submitted in partial satisfaction of the
requirements for the degree of
Doctor of Philosophy

in

Engineering – Mechanical Engineering

in the

Graduate Division

of the

University of California, Berkeley

Committee in charge:

Professor Sanjay Govindjee, Co-chair
Professor Panayiotis Papadopoulos, Co-chair
Professor David J. Steigmann
Professor Clark T.-C. Nguyen

Spring 2015

A High-order Eulerian-Lagrangian Finite Element Method for Coupled Electro-mechanical Systems

Abstract

A High-order Eulerian-Lagrangian Finite Element Method for Coupled Electro-mechanical Systems

by

Gerd Brandstetter

Doctor of Philosophy in Engineering – Mechanical Engineering

University of California, Berkeley

Professor Sanjay Govindjee, Co-chair

Professor Panayiotis Papadopoulos, Co-chair

The main focus of this work is on the development of a high-order Eulerian-Lagrangian finite element method for the simulation of electro-mechanical systems. The coupled problem is solved by a staggered scheme, where the mechanical motion is discretized by standard Lagrangian finite elements, and the electrical field is solved on a fixed Eulerian grid with embedded boundary conditions. Traditional Lagrangian-Lagrangian or arbitrary Lagrangian-Eulerian (ALE) methods encounter deficiencies, for example, when dealing with mesh distortion due to large deformations, or topology changes due to contacting bodies. The presented Eulerian-Lagrangian approach addresses these issues in a natural way. Within this context we develop a high-order immersed boundary discontinuous-Galerkin (IB-DG) method, which is shown to be necessary for (i) the accurate representation of the electrical gradient along nonlinear boundary features such as singular corners, and (ii) to achieve full convergence during the iterative global solution. We develop an implicit scheme based on the mid-point rule, as well as an explicit scheme based on the centered-difference method, with the incorporation of energy conserving, frictionless contact algorithms for an elastic-to-rigid-surface contact. The performance of the proposed method is assessed for several benchmark tests: the electro-static force vector around a singular corner, the quasi-static pull-in of an electro-mechanically actuated switch, the excitation of a carbon nanotube at resonance, and the cyclic impact simulation of a micro-electro-mechanical resonant-switch. We report improved accuracy for the high-order method as compared to low-order methods, and linear convergence in the iterative solution of the staggered scheme. Additionally, we investigate a Newton-Krylov shooting scheme in order to directly find cyclic steady states of electro-mechanical devices excited at resonance– as opposed to a naive time-stepping from zero initial conditions. For the examples discussed, we observe power law computational speed-ups of the form $S = 0.7\xi^{-0.8}$, where ξ is the damping ratio of the corresponding resonance frequency.

To my parents.

Contents

List of Figures

List of Tables

List of Algorithms

Acknowledgments

First and foremost, I would like to thank my advisor Professor Sanjay Govindjee for the great opportunity to conduct these doctoral studies at the University of California in Berkeley. It has been the most inspiring time, and I am honored by his brilliant mentorship and guidance to explore such new areas in research. I greatly acknowledge all the help and support throughout these years. His thoughtful advice, steady encouragement, and patience lead to an extremely fruitful and unique learning experience, that I will keep in my best memories.

I would also like to thank Professors David Steigmann and Panos Papadopoulos for their time to serve in my dissertation committee and to co-advise me on this work. The invaluable advice and lectures on electro-mechanics and computational mechanics opened fascinating new perspectives to me. Moreover, I would like to thank Professor Clark Nguyen for being in my dissertation committee and the valuable feedback on the MEMS modelling.

It is with great pleasure, that I would like to thank Dr. Manish Chandhok, Dr. Seh-Jin Park, Dr. Erik Anderson, and Professor Andy Neureuther for the lively collaboration on the EUV mask chucking project in the beginning of this PhD.

Finally, I want to thank all my colleagues and friends, especially Sunny Mistry, Koki Sagiyama, Toby Mitchell, Giuseppe Montella, Paul Drazin, Ahmed Bakhaty, Aurélie Azoug, Jerome Hauselle, Tsuyoshi Koyama, Ahmet Can Tanyeri, Marco Broccardo, James Goulet, Jeff Clarkson, Niels Quack, Marcus Lehmann, Varun Mishra, Juan Pablo, Juan Mussat, Houfu Fan, Neal Simon Kwong, Neil Hodge, Kranthi Mandadapu, Matti Morzfeld, Brett Collins, Debanjan Mukherjee, and Jyothi Krishnan, for sharing so many moments and helpful discussions throughout these years!

Last but not least, I want to thank my family for their unconditional support and help in every situation of this adventure. If it wasn't for you, I would not be where I am standing today.

Chapter 1

Introduction

The major motivation of this work resulted from various challenges of traditional technology facing today's needs for highly accurate and efficient simulations of electro-mechanical systems. Throughout this study, we have had many great collaborations on the theoretical aspect of the continuum modeling, the computational treatment, as well as on the actual design of real-world systems. In the beginning of this dissertation, we have worked on the modeling and simulation of electro-static chucking of photo-masks in next generation extreme-ultraviolet-lithography (EUVL), which was a collaborative project with the Intel Corporation ®. A typical mask and chuck system is pictured in Fig. 1.1. EUVL has a great chance to become the new standard for chip fabrication, using EUV light with a wavelength of around 13 nm [6]. As the EUV light is absorbed by classical photo-masks, reflective masks as in Fig. 1.1(left) must be used. Considering the overall mask dimensions of $152 \times 152 \times 6.35$ mm, one faces extremely small tolerances on the mask surface out-of-plane deformation < 10 mm, which is very difficult to achieve in practice. When the mask is hold by the electro-static chuck in the exposure tool, any nonflatness of the mask and chuck surface will result in a deformation of the mask during the chucking process, which will lead to a pattern placement error due to the out-of-plane and in-plane deformation of the mask. We have examined the effect of the mask deformation on the pattern placement error during electro-static chucking by finite element models as well as enhanced analytical estimates. Such models have been tested to pre-correct for the pattern placement during the e-beam write step [1]. Particular focus has been put upon the effect of the mask back-side non-flatness features on the deformation, the estimates of critical particulate contamination, and the effect of pin-chucks [7, 8].

From Macro to Nano

As another application of our interest, we have studied micro-electro-mechanical systems (MEMS). In particular, we have examined a micro-electro-mechanical disk resonator / resonance switch as pictured, for example, in Fig. 1.2. Such resonators / switches show high potential to replace classical transistors, e.g. for on-chip power amplification, as they are

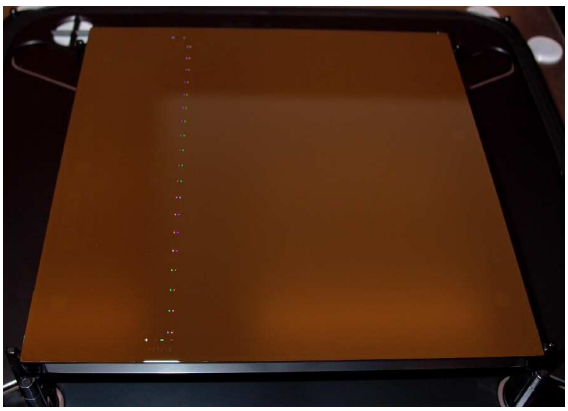

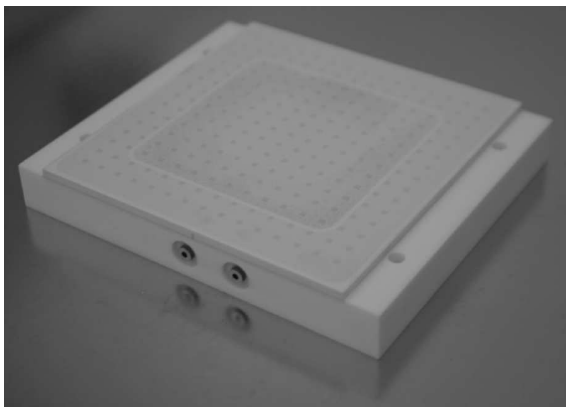

Figure 1.1: Extreme-ultraviolet-lithography mask-chuck system: (left) image of mask by [1]; (right) image of Coulomb-type electro-static pin-chuck by [2].

much more energy-efficient [9, 10, 3, 11, 12]. The disk in Fig. 1.2(left) is excited in the wine-glass mode by a set of driving electrodes and the electrical pressure will force the disk into a dynamic steady contact with the output electrode. The developed simulation tool in this thesis allows not only for a full-field simulation of the coupled problem with the occurring topological changes, but also respects the capacitor charge loading in the presence of a load resistance R_L during '*off*'-mode, as well as the jump in the electrical boundary conditions during electrical breakdown, or when the disk touches the output electrode as pictured in Fig. 1.2(right) (see Sections 4.9 and 5.5).

On an even smaller scale, we have considered the dynamical excitation of carbon nanotubes (CNTs) by an external electrical field as pictured in Fig. 1.3. CNTs possess very unique and promising characteristics for the use in nano-electro-mechanical systems (NEMS) [13, 14, 15, 4, 16]. Under certain assumptions, the use of continuum mechanical theory to analyze such small-scale devices at the nanometer scale can be justified [17]. As demonstrated in the picture, an electrical potential difference between the nanotube and an external electrode will largely bend the nanotube [Fig. 1.3(b)]. Our numerical method as developed in Chapter 4 will enable us to efficiently calculate the response of such a strongly coupled problem considering the full nonlinear mechanical response, as well as the interaction with the electrical field that penetrates all space (see Section 4.8 and 5.4). Particular focus is here on the accurate evaluation of the tip force, where small radii or corners will dominate the electrical force due to the singular, or nearly singular charge accumulation (see also Chapter 3 and Section 4.6 and 5.4).

From Statics to GHz

For the modeling of systems such as in Fig. 1.1, a quasi-static analysis has been used, whereas a MEMS resonator as in Fig. 1.2 operates at 25 MHz, and NEMS resonators made of CNTs

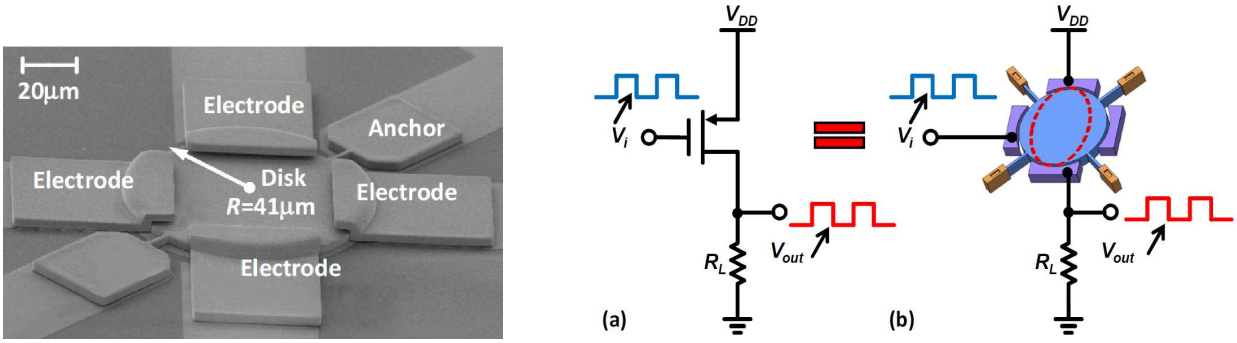

Figure 1.2: Metal micromechanical resonant switch by [3]: (left) SEM image of a 25 MHz nickel resonant switch; (right) schematic of power-gain circuit of (a) a traditional transistor switch, and (b) a resonant switch.

are predicted to have fundamental frequencies of 1 GHz or higher. In order to accommodate this range of frequencies, we develop second order explicit as well as implicit time-integration schemes, which allow for the incorporation of mechanical impact (see Section 4.5). The method as presented in Section 4.5 is based on a staggered scheme, that relies on an operator split for the evolution of the mechanical and electrical field. As one is typically interested in the analysis of the steady state response, time-stepping throughout the transient phase becomes very expensive– especially for modern systems with high quality factors in the thousands as in [18, 3]. We discuss the use of a direct method to solve for cyclic steady states, and observe substantial speed-ups in comparison to a naive time-stepping from zero initial conditions (Chapter 5).

From Analytics to Numerics

The full-field simulation of the electro-mechanical boundary value problem by high-order numerical methods is absolutely necessary for the accurate analysis of systems such as CNTs in Fig. 1.3 or the reso-switch pictured in Fig. 1.2– especially when singular forces due to corners occur, or when nonlinearities due to large deformation or impact are involved. However, we do acknowledge the power of analytical estimates under certain assumptions. Analytical formulas have been used throughout this thesis in order to benchmark the numerical methods. Such estimates have also been developed in order to deliver fast methods to estimate effects of system parameters during the design process, as well as for real-time systems where the model response must be obtained immediately. In our work with the Intel Corporation ®, we have developed enhanced analytical methods to predict for the deformation of EUVL photomasks during mask-chucking (see Fig. 1.1). Those methods have been successfully tested in an overlay error compensation experiment for pattern placement correction, and they serve as estimates for critical particle contamination during EUV mask-chucking. Since this work

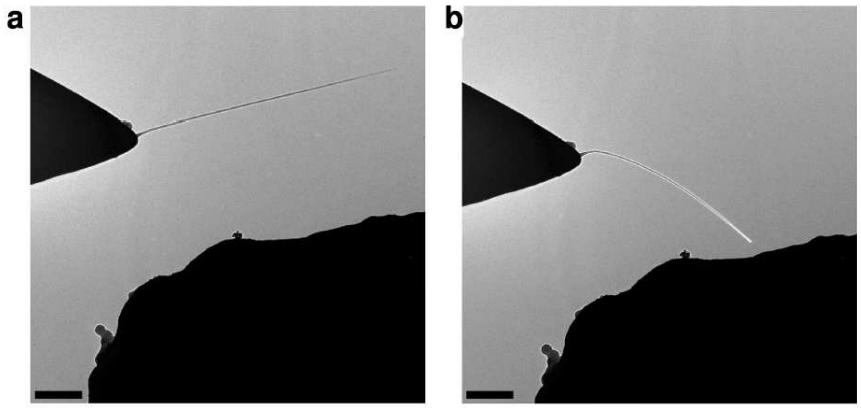

Figure 1.3: TEM image of a carbon nanotube by [4]: (a) zero bias voltage; (b) deformed nanotube due to bias voltage (scale bar is 500 nm).

has been documented elsewhere, and there are no implications of the developed analytical estimates for the remainder of this document, we refer the interested reader to [7, 8]. In the following we will focus on the numerical treatment of the electro-mechanical continuum problem.

State of The Art

Until today, many software packages have been developed for the simulation of electro-mechanical systems. One of the main challenges is solving the electrical field in a computational domain that differs from the computational domain of the mechanical deformation. In particular the electrical field penetrates all space, with boundary conditions at infinity, and the material parameters and internal boundary conditions within this domain change as mechanical bodies move and possibly collide with each other. Without the claim of completeness, we shortly discuss two traditional approaches to solve the electro-mechanical problem that are related to the finite element method. In particular we mention the coupled finite-element/boundary-element method (FEBE), with its early development by [19, 20, 21] for the design of micro-electro-mechanical systems (MEMS). In [22, 23] the authors developed a staggered algorithm, which was subsequently enhanced by [24, 25, 26], and which is now the basis for the MEMS simulation software by Coventor Inc®. Further developments of the method can be found in [27, 28, 29, 30, 31, 32]. Very recently, a new algorithm has been developed by [33, 34, 35], which allows for penetrating fields as necessary, for example, to simulate nonlinear electro-elastic materials. The FEBE method is very attractive since the far-field effect of the external electrical field can be captured by a minimum amount of degrees of freedom associated with the boundary of the mechanical continuum. However, the boundary element method faces difficulties when boundaries come close or contact due to the singular integration involved. Moreover, the boundary element method is not capable

to model a surrounding dielectric medium, where Green's function does not exist.

Alternatively, Lagrangian finite element methods have been developed to capture both the mechanical motion, as well as the internal and external electrical fields. As a popular method we note the arbitrary Lagrangian-Eulerian method (ALE), which has been developed to simulate fluid structure interaction (see for example [36, 37]). In the context of electro-mechanical systems, many groups have been using the ALE approach (for example [20, 38, 39, 40]), and the Lagrangian approach has become a standard in the COMSOL®package [41, 42]. In every Lagrangian formulation the mesh motion of the electrical domain has to be defined. When the mechanical structure experiences large deformations, elements of the surrounding space may get distorted and ill-conditioned, which necessitates remeshing. Moreover, when two bodies come into contact, elements of the surrounding space may collapse as the gap closes, which will require special consideration to render meaningful results.

Eulerian Methods – A Promising Approach

Due to the shortcomings mentioned, Eulerian finite element methods with embedded boundary conditions have recently gained attention for the simulation of electro-mechanical systems [43, 44]. Immersed boundary methods have become a standard in related fields, such as the simulation of fluid-structure interaction, crack propagation, or phase transitions. However, in the electro-mechanical community there are only limited studies available– despite the apparent advantages: the Eulerian method will naturally avoid any element-distortions or element-collapse when two bodies come into contact and the surrounding topological space changes. Moreover, the use of finite elements enables one to model any non-linear surrounding dielectric media, which is not possible, in general, by the boundary element method. Finally, such a method will allow for an extension of this work, for example, to electro-fluid-structure interaction problems, where the fluid-field can be solved on the Eulerian grid that surrounds the mechanical body. Nonetheless, all these attractive features come along with the challenge to enforce Dirichlet boundary conditions on an immersed boundary, and the need to accurately represent the gradients along this boundary. In [43] the fictitious domain method is used with a distributed Lagrange multiplier, whereas in [44] the eXtended finite element technique is employed in order to solve the electrostatic problem on a fixed grid. Low-order immersed boundary methods as in [43, 44] encounter issues, when gradients along nonlinear geometric boundaries such as curved boundaries or corners have to be resolved. In this work, we promote the use of a newly developed high-order immersed boundary method [45]. The method relies on a higher-order approximation to the immersed boundary shape, as well as a higher-order interpolation space in all intersected elements based on the analytical solution of the underlying partial differential equation in the close neighborhood of the boundary. This will enable a very accurate direct evaluation of the Maxwell-traction along the immersed boundary– without the need of any post-processing smoothing operation. Moreover, any singular gradients due to corners can be captured in a natural way. As will be demonstrated in the numerical examples, such higher-order accuracy is needed not only to obtain any physically meaningful results, but also to achieve full convergence during

the global iterative solution of the coupled equations.

The Outline

In Chapter 2 we outline the governing equations of the continuum electro-mechanical boundary value problem together with the material model used throughout this thesis. In Chapter 3 we develop a novel high-order immersed boundary discontinuous-Galerkin method, that puts emphasis on the accurate representation of the field gradient for higher-order boundary features such as curved boundaries or corners where singularities are present. In Chapter 4 we present the algorithmic treatment of the coupled electro-mechanical problem in the quasi-static, as well as the dynamic setting. For both cases, we discuss an elastic-to-rigid-surface contact driver that enables the simulation of pull-in as well as impact for electrically actuated devices. In Chapter 5 an efficient method is discussed in order to simulate electro-mechanical devices excited at resonance. Such an approach will deliver substantial computational speed-ups in comparison to the transient time-stepping from zero initial conditions– especially when low damping is present.

Chapter 2

Electro-mechanical Continuum Model

To begin with, let us state the governing equations of the coupled electro-mechanical problem of interest, as well as the material models used in this work. To this end, we closely follow the presentation in [46, 47].

2.1 Balance Laws and Thermodynamics

Let us assume that a continuum body $\mathcal{R}$ with mass density ρ is surrounded by a vacuum $\mathcal{V}$ (see Fig. 2.1). In the following we will describe the deformation of this body with respect to a reference configuration $\mathcal{R}_0$ at time $t = t_0$. For each material point X in the reference configuration $\mathcal{R}_0$ we associate a vector $\mathbf{X} \in \mathbb{R}^3$. Consequently for the same material point in $\mathcal{R}$ we associate $\mathbf{x} \in \mathbb{R}^3$. Then we define the displacement $\mathbf{u}(\mathbf{X}, t) \in \mathbb{R}^3$, which maps $\mathbf{X}$ to $\mathbf{x}(\mathbf{X}, t) = \mathbf{X} + \mathbf{u}(\mathbf{X}, t)$ for all $t > t_0$. Let us assume in the following that the magnetic field is negligible and that the electrostatic field is quasi-static in comparison to the dynamics of the continuum body. Then, whenever the fields are smooth, we have to locally satisfy the mass-balance

$$\dot{\rho} + \rho \mathrm{div} \dot{\mathbf{u}} = 0 \,, \tag{2.1}$$

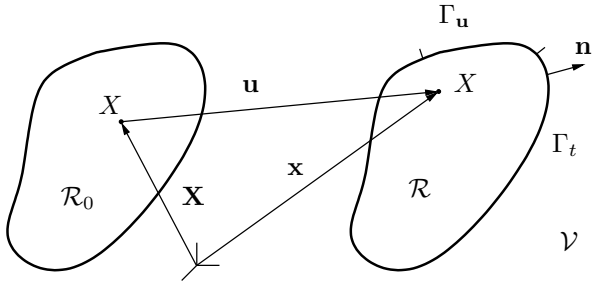

Figure 2.1: Schematic of mechanical boundary value problem.

where $\dot{\mathbf{u}}$ is the material velocity. Euler's first law in the coupled theory is adjusted to

$$\rho\ddot{\mathbf{u}} = \mathrm{div}\mathbf{T} + \rho\bar{\mathbf{b}} \quad \text{in } \mathcal{R}\,, \tag{2.2}$$

$$\mathbf{u} = \bar{\mathbf{u}} \qquad \text{on } \Gamma_{\mathbf{u}}\,, \tag{2.3}$$

where $\bar{\mathbf{b}}$ is the standard body force term and $\mathbf{T}$ is the total Cauchy stress. From the moment-of-momentum balance, one can derive

$$\mathrm{skew}\,[\mathbf{T}] = 0\,. \tag{2.4}$$

Note that a non-symmetric Cauchy stress in the coupled theory might exist if the magnetic and electric field are both non-vanishing, which has been precluded in this study by assumption. In our case, the total Cauchy stress is given by

$$\mathbf{T} = \boldsymbol{\sigma} + \mathbf{e}\otimes\mathbf{p} + \mathbf{T}_M\,, \tag{2.5}$$

where $\mathbf{T}_M$ is the Maxwell stress given by

$$\mathbf{T}_M = \epsilon_0\left(\mathbf{e}\otimes\mathbf{e} - \frac{1}{2}\left(\mathbf{e}\cdot\mathbf{e}\right)\mathbf{I}\right)\,, \tag{2.6}$$

ϵ_0 is the permittivity of free space, $\mathbf{e}$, $\mathbf{p}$ are the electrical field and the material polarization, and $\boldsymbol{\sigma}$ a constitutively determined part of the Cauchy stress. Note that the Maxwell stress penetrates all matter and is independent of any material law. Note especially that the Maxwell stress is non-vanishing outside a material body, which one needs to take into account when deriving boundary conditions in the weak form. The stress boundary condition will be derived in Section 4.1 by the requirement

$$[\![\mathbf{T}]\!]\mathbf{n} = 0\,, \tag{2.7}$$

where $[\![\mathbf{T}]\!]$ denotes the jump in the total Cauchy stress across the boundary of interest. The first two terms in (2.5) are the constitutively determined part of the Cauchy stress. The functional dependency of $\boldsymbol{\sigma}$, $\mathbf{e}$ and $\mathbf{p}$ comes from a thermodynamical argument as illustrated in the next section.

The Maxwell equations simplify for the electro-static case and smooth fields to

$$\mathrm{div}\mathbf{d} = \rho_f\,, \quad \mathrm{curl}\mathbf{e} = 0\,, \tag{2.8}$$

where $\mathbf{d} = \epsilon_0\mathbf{e} + \mathbf{p}$ is the vector potential (electric displacement) for the free charges with density ρ_f. The jump conditions read

$$[\![\mathbf{d}]\!]\cdot\mathbf{n} = \sigma_f\,, \quad \mathbf{n}\times[\![\mathbf{e}]\!] = \mathbf{0}\,, \tag{2.9}$$

where σ_f is the surface charge density. Note that $(2.8)_2$ can be solved via potential Φ such that $\mathbf{e} = -\nabla\Phi$, and we need to solve

$$-\epsilon_0\mathrm{div}\nabla\Phi + \mathrm{div}\mathbf{p} = \rho_f\,, \tag{2.10}$$

with appropriate boundary conditions. Note that *if and only if* $\mathbf{p}$ is linearly related to $\mathbf{e}$, that is one assumes a linear dielectric material $\mathbf{d} = \boldsymbol{\epsilon}\mathbf{e}$ with permittivity tensor $\boldsymbol{\epsilon}$, one can derive

$$\mathrm{div}\boldsymbol{\epsilon}\nabla\Phi = -\rho_f\,, \tag{2.11}$$

which reduces to

$$\nabla^2\Phi = -\rho_f/\epsilon \tag{2.12}$$

for an isotropic, homogeneous material $\boldsymbol{\epsilon}(\mathbf{x}) = \epsilon\mathbf{I}$, $\forall\mathbf{x} \in \mathcal{R}$. Any non-linear material law for the polarization requires a full solution of (2.10), and the simplified equations (2.11), (2.12) will not be sufficient to model the problem.

As the first law of thermodynamics we assume

$$\rho\dot{\varepsilon} = \mathrm{div}\mathbf{T}^T\dot{\mathbf{x}} + \rho\dot{\mathbf{x}}\cdot\bar{\mathbf{b}} + \rho h - \mathrm{div}\mathbf{q}\,, \tag{2.13}$$

where ε is the internal energy of the material, h some external heat source, and $\mathbf{q}$ the heat flux.

The second law can be cast in the form

$$-\rho\dot{\psi} - \rho\eta\dot{\Theta} - \mathbf{p}\cdot\dot{\mathbf{e}} + \boldsymbol{\sigma}\cdot\nabla\dot{\mathbf{x}} - \Theta^{-1}\mathbf{q}\cdot\nabla\Theta \geq 0\,, \tag{2.14}$$

where ψ is some potential function involving the internal energy, Θ the absolute temperature, and η the entropy.

All equations thus far deliver the local forms of the underlying physical laws together with the corresponding jump conditions. They can be solved (in principle) when we specify constitutive relations for the quantities $\boldsymbol{\sigma}$, ψ, $\mathbf{q}$, η and $\mathbf{p}$. In the following section we will derive restrictions on the constitutive laws by using the entropy inequality (2.14) and moment-of-momentum balance (2.4); i.e. we will find restrictions on the constitutive dependency such that these two laws are automatically satisfied.

2.2 Constitutive Modeling

Let us assume that the stress, energy, entropy and material polarization are constitutively dependent on $\{\mathbf{F}, \Theta, \mathbf{e}\}$, where $\mathbf{F}$ is the deformation gradient. Thus, we assume that the potential function ψ takes the form

$$\psi = \psi(\mathbf{F}, \Theta, \mathbf{e})\,. \tag{2.15}$$

Note that this assumption limits us to elastic materials. Any dissipative effects as seen in visco-elastic, plastic, or ferro-electric materials are not considered here (see e.g. [48, 49] for further discussions). From (2.14) we get by a standard argument

$$\boldsymbol{\sigma} = \rho\psi_{\mathbf{F}}\mathbf{F}^T \tag{2.16}$$

$$\mathbf{p} = -\rho\psi_{\mathbf{e}} \tag{2.17}$$

$$\eta = -\psi_{\Theta} \tag{2.18}$$

$$-(\mathbf{q}\cdot\nabla\Theta)/\Theta \geq 0\,. \tag{2.19}$$

If we use (2.16), (2.17), one can show that (2.4) is equivalent to the requirement

$$\psi = \psi(\mathbf{C}, \Theta, \mathbf{E}) \,, \tag{2.20}$$

where $\mathbf{C} = \mathbf{F}^T\mathbf{F}$ and $\mathbf{E} = \mathbf{F}^T\mathbf{e}$. In order to derive (2.20), one essentially follows a similar argument as in [50, p.44]. Note that this requirement also assures the Invariance under superimposed rigid body motions. We then deduce from (2.5), (2.16), and (2.17) that the total Cauchy stress and polarization read

$$\mathbf{T} = 2\rho\mathbf{F}\left(\mathrm{sym}\frac{\partial\psi}{\partial\mathbf{C}}\right)\mathbf{F}^T + \mathbf{T}_M \,, \tag{2.21}$$

$$\mathbf{p} = -\rho\mathbf{F}\frac{\partial\psi}{\partial\mathbf{E}} \,, \tag{2.22}$$

where we have used $\psi_{\mathbf{F}} = 2\mathbf{F}\left(\mathrm{sym}\frac{\partial\psi}{\partial\mathbf{C}}\right) + \mathbf{e}\otimes\frac{\partial\psi}{\partial\mathbf{E}}$, and $\psi_{\mathbf{e}} = \mathbf{F}\frac{\partial\psi}{\partial\mathbf{E}}$. Note in particular $\boldsymbol{\sigma} = \rho\psi_{\mathbf{F}}\mathbf{F}^T = 2\rho\mathbf{F}\left(\mathrm{sym}\frac{\partial\psi}{\partial\mathbf{C}}\right)\mathbf{F}^T - \mathbf{e}\otimes\mathbf{p}$. In the following we will assume the isothermal case; i.e.

$$\psi = \psi(\mathbf{C}, \mathbf{E}) \,. \tag{2.23}$$

Another constraint is the symmetry group of the material. If λ is a symmetry transformation, we require

$$\psi(\mathbf{C}, \mathbf{E}) = \psi(\mathbf{R}^T\mathbf{C}\mathbf{R}, \mathbf{R}^T\mathbf{E}) \,, \tag{2.24}$$

where $\mathbf{R} = \nabla\lambda$. In this context we focus on isotropic materials; i.e. $\mathbf{R} \in \mathcal{O}$, where $\mathcal{O}$ is the group of orthogonal tensors. For anisotropic materials as needed in piezo-electric materials we refer to [49, 51]. For the isotropic case one can derive that the energy is a function of the six invariants

$$\psi = \psi(I_1, I_2, I_3, I_4, I_5, I_6) \,, \tag{2.25}$$

where

$$I_1 = \mathrm{tr}\mathbf{C},\ I_2 = \mathrm{tr}\mathbf{C}^*,\ I_3 = \mathrm{det}\mathbf{C}, \tag{2.26}$$

$$I_4 = \mathrm{tr}\left(\mathbf{C}\mathbf{E}\otimes\mathbf{E}\right),\ I_5 = \mathrm{tr}\left(\mathbf{C}^2\mathbf{E}\otimes\mathbf{E}\right),\ I_6 = \mathrm{tr}\left(\mathbf{E}\otimes\mathbf{E}\right), \tag{2.27}$$

with $\mathbf{C}^* = (\mathrm{det}\mathbf{C})\,\mathbf{C}^{-1}$. This reduces the number of independent parameters from 9 to 6 [cf. (2.23)]. If we define $\psi_i \equiv \frac{\partial\psi}{\partial I_i}$, we derive

$$\mathrm{sym}\frac{\partial\psi}{\partial\mathbf{C}} = (\psi_1 + \psi_2 I_1)\,\mathbf{I} - \psi_2\mathbf{C} + \psi_3 I_3\mathbf{C}^{-1} + \psi_4\mathbf{E}\otimes\mathbf{E} + \psi_5\left[\mathbf{C}\left(\mathbf{E}\otimes\mathbf{E}\right) + \left(\mathbf{E}\otimes\mathbf{E}\right)\mathbf{C}\right] \,, \tag{2.28}$$

$$\frac{\partial\psi}{\partial\mathbf{E}} = 2\left(\psi_4\mathbf{C} + \psi_5\mathbf{C}^2 + \psi_6\mathbf{I}\right)\mathbf{E} \,. \tag{2.29}$$

We will now split the Cauchy stress (2.21) into

$$\mathbf{T} = \mathbf{T}_m + \mathbf{T}_e \,, \tag{2.30}$$

with a purely mechanical part $\mathbf{T}_m$, and an electrical part $\mathbf{T}_e$. Using (2.21), (2.22), (2.28), and (2.29), one gets

$$\mathbf{T}_m = 2\rho \left[(\psi_1 + \psi_2 I_1)\, \mathbf{B} - \psi_2 \mathbf{B}^2 + \psi_3 I_3 \mathbf{I} \right] , \tag{2.31}$$

$$\mathbf{T}_e = 2\rho \left\{ \psi_4 \mathbf{Be} \otimes \mathbf{Be} + \psi_5 \left[\mathbf{B} \left(\mathbf{Be} \otimes \mathbf{Be} \right) + \left(\mathbf{Be} \otimes \mathbf{Be} \right) \mathbf{B} \right] \right\} + \mathbf{T}_M , \tag{2.32}$$

$$\mathbf{p} = -2\rho \left(\psi_4 \mathbf{B}^2 + \psi_5 \mathbf{B}^3 + \psi_6 \mathbf{B} \right) \mathbf{e} , \tag{2.33}$$

where $\mathbf{B} = \mathbf{F}\mathbf{F}^T$ denotes the left Cauchy-Green tensor. In lieu of (2.5), we note that $\boldsymbol{\sigma} = \mathbf{T}_m + \mathbf{T}_e - \mathbf{e} \otimes \mathbf{p} - \mathbf{T}_M$. Various propositions exist for the form of the energy ψ. Next, we will discuss some examples that are typically found in the literature.

2.3 Examples

In [34], the authors propose the form

$$\psi = \frac{\mu}{2} \left(I_1 - 3 \right) - \mu \ln J + \frac{\Lambda}{2} \left(\ln J \right)^2 + \alpha I_4 + \beta I_5 + \gamma I_6 , \tag{2.34}$$

where $\{\mu, \Lambda, \alpha, \beta, \gamma\}$ are five independent material parameters, and $J = \det\mathbf{F} = \sqrt{I_3}$. In this form, following (2.29), the polarization will not be consistent (in general) with a linear dielectric. Thus a solution via (2.11) and (2.12) is not accessible, and one rather has to solve the non-linear equation (2.10).

In order to obtain a formulation that accounts for a linear polarization, [52] propose an incompressible material ($J = \det\mathbf{F} = 1$) with

$$\psi = c_1 \left(I_1 - 3 \right) + c_2 \left(I_2 - 3 \right) + c \left(I_5 - I_1 I_4 + I_2 I_6 \right) , \tag{2.35}$$

and three material parameters $\{c_1, c_2, c\}$. Here one can write $c_1 = G\delta/2$, $c_2 = G(1-\delta)/2$ and $c = -(\epsilon - \epsilon_0)/(2\rho_0)$, where G is the small deformation shear modulus and $\delta \in (0, 1)$ a material parameter. The referential mass density is $\rho_0 = J\rho = \rho$ for an incompressible material. Note that this form is an enhancement of the Mooney-Rivlin material with an additional term to account for the electric field. From (2.31), we obtain the standard Mooney-Rivlin response by assuming the absence of an electrical field:

$$\mathbf{T}_m = -p\mathbf{I} + 2\rho \left[(c_1 + c_2 I_1)\, \mathbf{B} - c_2 \mathbf{B}^2 \right] , \tag{2.36}$$

and from (2.32) the stress due to the electrical field:

$$\begin{aligned} \mathbf{T}_e = & 2\rho c \left[(I_1 I_6 - I_4)\, \mathbf{B} - I_6 \mathbf{B}^2 - I_1 \mathbf{Be} \otimes \mathbf{Be} \right. \\ & \left. + \mathbf{B} \left(\mathbf{Be} \otimes \mathbf{Be} \right) + \left(\mathbf{Be} \otimes \mathbf{Be} \right) \mathbf{B} \right] + \mathbf{T}_M . \end{aligned} \tag{2.37}$$

Here the added constraint pressure p-term accounts for incompressibility. For the polarization, from (2.33), we get

$$\mathbf{p} = (\epsilon - \epsilon_0)\, \mathbf{e} , \tag{2.38}$$

with the linear dependency on $\mathbf{e}$ as desired.

Note that many authors use

$$\mathbf{T} = \tilde{\mathbf{T}} + \mathbf{e} \otimes \mathbf{d} - \frac{1}{2} (\mathbf{e} \cdot \mathbf{d}) \mathbf{I} , \tag{2.39}$$

where $\tilde{\mathbf{T}}$ is the constitutively determined stress due to any deformation in the absence of an electric field. One can derive this form in the case of a linear dielectric *fluid* via a similar thermodynamical argument (see e.g. [46, p.245]). However, we cannot find a corresponding potential in the case of a dielectric *solid* that is consistent with the thermodynamical considerations presented here. This issue has been discussed by [52], and we adopt their findings in this work– that is we regard (2.39) as obsolete in the discussion of dielectric *solids*.

In the examples as discussed in Chapter 4 and 5 we propose the use of a non-linear compressible Neo-Hookean material, with added terms to account for the electric field effects and a linear polarization in accordance with the model proposed by [52]. To this end we assume

$$\psi = \frac{\mu}{2} (I_1 - 3) - \mu \ln J + \frac{\Lambda}{2} (\ln J)^2 + c\, J^{-1} (I_5 - I_1 I_4 + I_2 I_6) , \tag{2.40}$$

given in terms of the small strain Lamé parameters $\Lambda = E\nu/[(1+\nu)(1-2\nu)]$, $\mu = E/[2(1+\nu)]$, the Young's modulus E, Poisson ratio ν, and $c = -(\epsilon - \epsilon_0)/(2\rho_0)$. From (2.31) we derive the purely mechanical part of the Cauchy stress

$$\mathbf{T}_m = \rho_0 J^{-1} (\Lambda \ln J - \mu) \mathbf{I} + \rho_0 \mu J^{-1} \mathbf{B} , \tag{2.41}$$

and from (2.32) the electrical part

$$\begin{aligned} \mathbf{T}_e =& 2\rho_0 c\, J^{-2} \left[1/2 (I_1 I_4 - I_2 I_6 - I_5) \mathbf{I} + (I_1 I_6 - I_4) \mathbf{B} - I_6 \mathbf{B}^2 \right. \\ & \left. - I_1 \mathbf{Be} \otimes \mathbf{Be} + \mathbf{B}(\mathbf{Be} \otimes \mathbf{Be}) + (\mathbf{Be} \otimes \mathbf{Be}) \mathbf{B} \right] + \mathbf{T}_M . \end{aligned} \tag{2.42}$$

The polarization according to (2.33) is found to be linear in $\mathbf{e}$,

$$\mathbf{p} = (\epsilon - \epsilon_0) \mathbf{e} , \tag{2.43}$$

as we desired.

Chapter 3

Immersed Boundary Method

For a linear material polarization, the electro-static boundary value problem reduces to solving Poisson's equation (2.12) for the electrical potential Φ. In this chapter, we adopt a numerical method to solve Poisson's equation on a fixed grid with embedded boundary conditions (see [45]). Special focus is put on the accurate representation of the normal gradient on the boundary. The lack of accuracy in the gradient evaluation on the boundary is a common issue with low-order embedded boundary methods. While a direct evaluation of the gradient is preferable, one typically uses post-processing techniques to improve the quality of the gradient. Here, we adopt a new method based on the discontinuous-Galerkin (DG) finite element method, inspired by the recent work of [53]. The basic idea of the method is pictured in Fig. 3.1. We observe the boundary Γ of the mechanical body $\mathcal{R}$, and the surrounding space $\mathcal{V}$. We have to solve for the electrical potential Φ in all space $\mathcal{R} \cup \mathcal{V}$. Note that later we will truncate the computational domain along Γ_{BE}, where we apply a far-field boundary condition. One uses standard finite elements in the white domain, and for elements intersected by the boundary Γ, one uses special elements that follow the boundary shape locally. In general, these elements are non-conforming, and they are put together in the DG framework. The original method by [53] has been enhanced in two aspects: Firstly, we approximate the boundary shape locally by higher-order geometric primitives. Secondly, we employ higher-order shape functions in intersected elements that we derive for the various geometric features of the boundary based on analytical solutions of the underlying partial differential equation. The development includes three basic geometric features in two dimensions for the solution of Poisson's equation: A straight boundary, a circular boundary, and a boundary with a discontinuity. We demonstrate the performance of the method via analytical benchmark examples with a smooth circular boundary as well as in the presence of a singularity due to a reentrant corner. Results are compared to a low-order extended finite element method as well as the DG method of [53]. We report improved accuracy of the gradient on the boundary by one order of magnitude, as well as improved convergence rates in the presence of a singular source. In principle, the method can be extended to three dimensions, more complicated boundary shapes, and other partial differential equations.

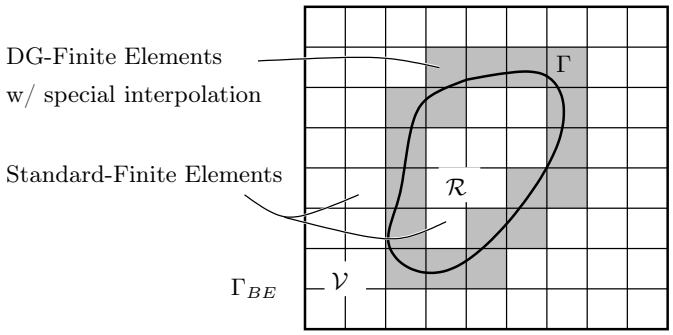

Figure 3.1: Schematic of the high-order immersed boundary DG method: Γ-boundary, intersected DG-finite elements, standard finite elements, and Γ_{BE}.

3.1 Introduction

Immersed boundary methods are popular in various fields of computational mechanics. As prominent examples one can name Peskin's immersed boundary method [54, 55], boundary fitting methods [56], fictitious domain methods [57, 58], and the eXtended finite element method (X-FEM) [59, 60]. These methods have been successfully applied to the simulation of fluid-structure interaction, crack propagation, and phase transitions among others. Our primary interest is in the solution of coupled electro-mechanical problems, where we wish to study moving mechanical bodies in electric fields; the bodies may be conductors or dielectrics. Recently, fixed-grid methods [43, 44] have become popular for this task. In comparison to classical Lagrangian methods that adapt their mesh according to the bodies' motion, immersed boundary methods have the clear advantage that no elements can be distorted, and no re-meshing is required for possibly large motions of the bodies. The obvious advantage, however, comes with some difficulties, for example: When Dirichlet type boundary conditions are given, they have to be enforced on non-conforming meshes. Bad element intersections may occur and require special treatment. And lastly, the accurate evaluation of gradients on the boundary often lacks precision. The last point becomes especially problematic in the solution of coupled problems such as in electro-mechanics, where the normal gradient on any interface boundary determines the traction on the body surface. Thus the accuracy of the gradients is crucial in obtaining physically meaningful results.

In this work we focus on a numerical method that is designed to provide high quality gradients at the interface. In this context we first review a low-order eXtended finite element method, where inaccuracies of the gradient at the interface is a common issue. In the literature there exist several post-processing techniques, which smooth the often largely oscillating gradient fields (e.g. [61]). Here we develop a method that allows one to evaluate the gradient accurately by direct differentiation of the bulk field. Among others, this has the clear advantage that the computational cost will be reduced and one can avoid difficulties of the smoothing operation that may break down when bodies come close, contact, or singu-

larities are involved. Our method follows in spirit the work of [53]. All elements intersected by a boundary will feature a special set of shape-functions that allow a strong imposition of Dirichlet boundary conditions along the immersed boundary. Those non-conforming elements are then put together in the context of a discontinuous-Galerkin (DG) method, where inter-element continuity is enforced in a weak sense in the region near the immersed boundary; regular finite elements are used everywhere else. This method has been adapted for example in [62] to problems in elasticity, where it showed very robust behavior in the enforcement of Dirichlet boundary conditions. In our method, we enhance this approach in two aspects: First, we use a higher-order representation of the boundary by approximating the boundary in each element locally via basic geometric primitives such as straight lines, circular curves, or wedges in two dimensions. Second, we use a special higher-order interpolation motivated by the analytical eigensolution of the underlying PDE in the neighborhood of the corresponding special boundary shape. Specifically we concentrate on Poisson's equation in two-dimensions; however, the method's basic idea can be adopted to more complicated boundary shapes and other types of PDEs in two as well as three dimensions. In comparison to the eXtended finite element method as well as the original DG-based immersed boundary method, we achieve much better accuracy of the gradient. Moreover, we demonstrate the capability to incorporate singularities as seen in the presence of corners in a natural way.

The outline of this chapter is as follows: In Section 3.2 and 3.3, we will state the problem and review a state-of-the-art X-FEM technique. In Section 3.4, we will layout the principles of the proposed high-order immersed boundary DG method (IB-DG), and our choice of boundary approximation and enrichment functions. Lastly, in Section 3.5, we discuss the performance of the high-order IB-DG method versus X-FEM and low-order IB-DG via numerical examples. Throughout we focus on electrostatics and ignore deformation so as to concentrate on the performance of the immersed boundary.

3.2 Governing Equations

We assume that we want to solve Poisson's equation in all space, which is divided into domains $\mathcal{R}$, $\mathcal{V}$ and $\mathcal{W}$ as pictured in Fig. 3.2. $\mathcal{R}$ should be thought of as a body and $\mathcal{V}, \mathcal{W}$ as air. Specifically we are interested in the solution of the electro-static BVP, with boundary conditions given along $\Gamma = \partial\mathcal{R}$. Assuming linear isotropic dielectric properties with permittivity

$$\epsilon(\mathbf{x}) = \begin{cases} \epsilon_{\mathcal{R}}\,, & \mathbf{x} \in \mathcal{R}\,, \\ \epsilon_{\mathcal{V}}\,, & \mathbf{x} \in \mathcal{V}\,, \\ \epsilon_{\mathcal{W}}\,, & \mathbf{x} \in \mathcal{W}\,, \end{cases} \tag{3.1}$$

we look at three typical cases.

Case 1. The body $\mathcal{R}$ is a conductor and the boundary Γ is a conducting surface where we know the potential $\Phi = \bar{\Phi}$. In the absence of any volume charge, the problem reads: Find

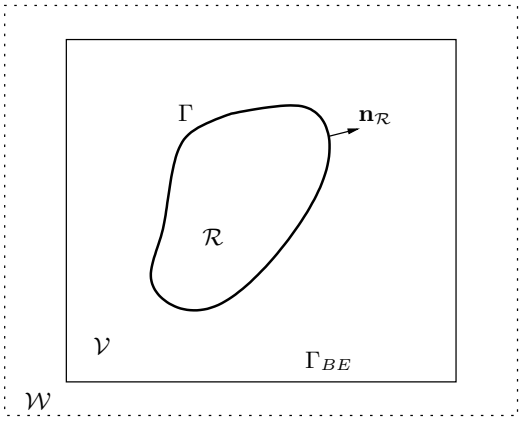

Figure 3.2: Problem definition and notation.

Φ, such that

$$\nabla^2\Phi = 0 \quad \text{all space}\,, \tag{3.2}$$

$$\Phi = \bar{\Phi} \quad \text{on } \Gamma\,, \tag{3.3}$$

where $\bar{\Phi}$ is any given Dirichlet boundary data along Γ.

Case 2. The body $\mathcal{R}$ is a conductor and the boundary Γ is a conducting surface where we know the total charge

$$Q = \int_\Gamma \sigma_f \,\mathrm{da} \tag{3.4}$$

on the surface. The free surface charge density $\sigma_f = [\![q]\!]$ is related to the jump of the flux $q = -\epsilon\nabla\Phi\cdot\mathbf{n}$ along the surface Γ with normal $\mathbf{n}$. In this case, we impose $\Phi = \bar{\Phi} = \text{constant}$ as a constraint and treat $\bar{\Phi}$ as an additional (scalar) unknown. The problem reads: Find $[\Phi, \bar{\Phi}]$, such that

$$\nabla^2\Phi = 0 \quad \text{all space}\,, \tag{3.5}$$

$$\Phi - \bar{\Phi} = 0 \quad \text{on } \Gamma\,, \tag{3.6}$$

$$\int_\Gamma [\![q]\!] \,\mathrm{da} = Q\,. \tag{3.7}$$

Case 3. The body $\mathcal{R}$ is a dielectric and the boundary Γ is a dielectric-dielectric interface. In this case the problem reads: Find Φ, such that

$$\nabla^2\Phi = 0 \quad \text{all space}\,, \tag{3.8}$$

$$[\![q]\!] = 0 \quad \text{on } \Gamma\,. \tag{3.9}$$

Again, $[\![q]\!]$ denotes the jump in the normal flux and (3.9) accounts for the fact that no free surface charge is present at a dielectric-dielectric interface by assumption. The Dirichlet boundary conditions on Φ in this case are assumed to be given away from Γ, see e.g. Section 3.5.

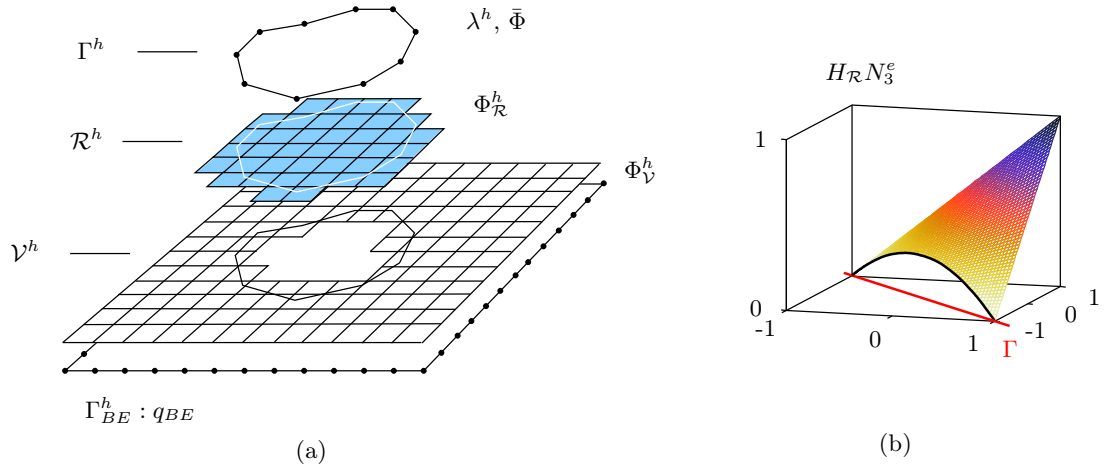

Figure 3.3: Schematic of the eXtended finite element method: (a) domain discretization and (b) discontinuous shape function.

3.3 Extended Finite Element Method (X-FEM)

For *Cases 1-3* we derive the variational form: Find $\Phi \in \mathcal{P}_s$, such that

$$\int_{\mathcal{R}} \epsilon_{\mathcal{R}} \nabla \delta\Phi \cdot \nabla \Phi \mathrm{dv} + \int_{\mathcal{V}} \epsilon_{\mathcal{V}} \nabla \delta\Phi \cdot \nabla \Phi \mathrm{dv} = -\int_{\Gamma_{BE}} \delta\Phi q_{\mathcal{V}} \,\mathrm{da} \tag{3.10}$$

for all $\delta\Phi \in \mathcal{P}_v$ along with the requirement $\Phi = \bar{\Phi}(s)$ on Γ for *Case 1* and *2*. Here s is a parameter along Γ, and the spaces $\mathcal{P}_s$ and $\mathcal{P}_v$ are suitable subspaces of H^1.

In order to solve (3.10) using X-FEM, one typically discretizes each domain as pictured in Fig. 3.3(a). In this depiction we assume the boundary Γ is discretized by linear elements, and $\mathcal{R}$, $\mathcal{V}$ are discretized by quadrilateral elements covering each domain of interest. The effect of $\mathcal{W}$ is modelled as a far field boundary condition along Γ_{BE} via the boundary element method (see App. A). All elements that are intersected by Γ will overlap and feature the interpolation

$$\Phi^h = \Phi^h_{\mathcal{R}} + \Phi^h_{\mathcal{V}} = \sum_i H_{\mathcal{R}} N_i \Phi_{\mathcal{R}i} + \sum_i H_{\mathcal{V}} N_i \Phi_{\mathcal{V}i} \,, \tag{3.11}$$

where N_i are the classical, finite element shape functions. The characteristic functions $H_{\mathcal{R}}$, $H_{\mathcal{V}}$ equal one in the corresponding domain, and zero elsewhere. A standard bi-linear interpolation has four degrees of freedom for each element; with one intersection, we get eight degrees of freedom defining the eXtended or enhanced element. Note the discontinuous shape functions will allow us to capture kinks in the potential field as pictured in Fig. 3.3(b). Using this interpolation, requires an additional constraint equation to enforce continuity along Γ.

The approximate problem then reads: Find $\Phi^h_{\mathcal{R}}, \Phi^h_{\mathcal{V}} \in \mathcal{P}^h_s$, such that

$$\int_{\mathcal{R}} \epsilon_{\mathcal{R}} \nabla \delta\Phi^h_{\mathcal{R}} \cdot \nabla \Phi^h_{\mathcal{R}} \mathrm{dv} + \int_{\mathcal{V}} \epsilon_{\mathcal{V}} \nabla \delta\Phi^h_{\mathcal{V}} \cdot \nabla \Phi^h_{\mathcal{V}} \mathrm{dv} = -\int_{\Gamma_{BE}} q_{\mathcal{V}} \delta\Phi^h_{\mathcal{V}} \mathrm{da} \tag{3.12}$$

for all $\delta\Phi^h_{\mathcal{R}}, \delta\Phi^h_{\mathcal{V}} \in \mathcal{P}^h_v$ along with the requirement $\Phi^h_{\mathcal{V}} = \Phi^h_{\mathcal{R}} = \bar{\Phi}(s)$ on Γ^h (for *Case 1* and *2*), and $\Phi^h_{\mathcal{V}} = \Phi^h_{\mathcal{R}}$ on Γ^h (for *Case 3*). Note that the last three requirements can only be enforced in a weak sense. For simplicity we only discuss the constraint $\Phi^h_{\mathcal{V}} = \bar{\Phi}(s)$ on Γ^h, the others follow in a similar fashion.

In order to enforce $\Phi_{\mathcal{V}} = \bar{\Phi}(s)$ on Γ in a weak sense, the Lagrange multiplier method is used. Let us introduce $\lambda \in \mathcal{L}$, where $\mathcal{L} = H^{-1/2}$. One then requires stationarity of the functional

$$\Pi_{LM}(\Phi_{\mathcal{V}}, \lambda) = \int_\Gamma \lambda \left(\Phi_{\mathcal{V}} - \bar{\Phi}\right) \mathrm{da}\,. \tag{3.13}$$

Upon variation, we obtain: Find $(\Phi_{\mathcal{V}}, \lambda) \in \mathcal{P}_s \times \mathcal{L}$, such that (3.10) holds, and such that

$$\int_\Gamma \delta\lambda\, \Phi_{\mathcal{V}} \mathrm{da} + \int_\Gamma \delta\Phi_{\mathcal{V}}\, \lambda \mathrm{da} = \int_\Gamma \delta\lambda\, \bar{\Phi} \mathrm{da} \tag{3.14}$$

for all $(\delta\Phi_{\mathcal{V}}, \delta\lambda) \in \mathcal{P}_v \times \mathcal{L}$. By choosing a discretization $\lambda^h \in \mathcal{L}^h$, we arrive at the discrete form: Find $(\Phi^h_{\mathcal{V}}, \lambda^h) \in \mathcal{P}^h_s \times \mathcal{L}^h$, such that (3.12) holds, and such that

$$\int_\Gamma \delta\lambda^h\, \Phi^h_{\mathcal{V}} \mathrm{da} + \int_\Gamma \delta\Phi^h_{\mathcal{V}}\, \lambda^h \mathrm{da} = \int_\Gamma \delta\lambda^h\, \bar{\Phi} \mathrm{da} \tag{3.15}$$

for all $(\delta\Phi^h_{\mathcal{V}}, \delta\lambda^h) \in \mathcal{P}^h_v \times \mathcal{L}^h$. One can proceed in an analogous manner for constraints $\Phi^h_{\mathcal{R}} = \bar{\Phi}$ and $\Phi^h_{\mathcal{V}} = \Phi^h_{\mathcal{R}}$ on Γ^h.

We remark that by a standard localization argument, from (3.12) and (3.15) one can show that the Lagrange multiplier equals the normal flux on the boundary:

$$\lambda^h = -\epsilon_{\mathcal{V}} \nabla\Phi^h_{\mathcal{V}} \cdot \mathbf{n}_{\mathcal{V}}\,. \tag{3.16}$$

As will be assessed in Section 3.5, this presents an interesting alternative to the direct evaluation of the normal gradient on the boundary.

Note that $\bar{\Phi}(s)$ is any given potential, and in the case of a *conducting* body $\bar{\Phi}$ will be constant on the body. For a typical electro-static problem, however, it might occur that the voltage (=potential) is not controlled, but rather the total electrical charge Q on a conductor is specified, and one must calculate the corresponding potential as a (scalar) unknown– the so-called floating potential problem. In this case we modify (3.15) to: Find $(\Phi^h_{\mathcal{V}}, \lambda^h, \bar{\Phi}) \in \mathcal{P}^h_s \times \mathcal{L}^h \times \mathbb{R}$, such that (3.12) holds, and such that

$$\bar{\Pi}_{LM}(\Phi^h_{\mathcal{V}}, \lambda^h, \bar{\Phi}) = \int_\Gamma \lambda^h \left(\Phi^h_{\mathcal{V}} - \bar{\Phi}\right) \mathrm{da} + Q\bar{\Phi} \tag{3.17}$$

is rendered stationary. The Lagrange multiplier λ^h can still be interpreted as the normal flux on the boundary, which is essentially the surface charge distribution (Section 3.2). Upon variation of (3.17) with respect to $\bar{\Phi}$, and requiring $\delta_{\bar{\Phi}}\bar{\Pi}_{LM} = 0$, we see that

$$Q = \int_\Gamma \lambda^h \mathrm{da}\,, \tag{3.18}$$

which is consistent with the constraint equation (3.7) for the given charge load.

Note that the Lagrange multiplier space $\mathcal{L}^h$ is not arbitrary but has to satisfy the *inf-sup* condition to ensure stability [63]. Moreover, the use of Lagrange multipliers delivers a non-positive system and additional degrees of freedom are introduced. There are many studies that deal with these issues and propose solutions on how to choose $\mathcal{L}^h$ [64, 65, 66]; further alternative formulations such as Nitsche's method or stabilized Lagrange multipliers respectively have also been advocated in [67, 68, 69, 70, 71, 72, 73, 74, 75]. For our purpose of benchmark testing, the classic Lagrange multiplier approach works nicely as we can control $\mathcal{L}^h$ *a-priori*.

We want to draw special attention to three short comings of the presented X-FEM method and related technologies, when utilizing a low-order interpolation such as the bi-linear interpolation. As will be demonstrated in Section 3.5, in the presence of a corner or any other complicated geometry one will not be able to interpolate the field exactly along the immersed boundary. Second, the bi-linear interpolation obviously does not account for any possible singularity in the gradient, as is seen for example at a corner. And third, the evaluation of the gradient on the boundary will in general be very inaccurate and highly oscillatory even for smooth boundaries, depending on where the background mesh is cut. These issues can be addressed by mesh-refinement, but it is certainly not in the spirit of embedded boundary methods that were developed to precisely avoid this. A higher-order X-FEM technique (e.g. [76]) may show some improvement related to these concerns, but we found the approach based on the discontinuous-Galerkin FEM as presented by [53] more natural to extend for our specific demands.

3.4 High-order Immersed Boundary discontinuous-Galerkin Method (IB-DG)

In this section we propose a new immersed boundary method based on the discontinuous-Galerkin FEM. The DG approach has been used by [53] and [77] recently in a similar context. However, to our knowledge, no studies have demonstrated yet the use of higher-order approximations to the boundary shape or interpolation space.

The basic idea is pictured in Fig. 3.1: All elements that are *not* intersected by the Γ-boundary utilize standard conforming finite elements. In our examples we will use a bi-linear interpolation. All elements that are intersected by the Γ-boundary utilize a special interpolation that is element-wise dependent on the shape and location of Γ. All intersected elements are by default non-conforming, and continuity across element boundaries and to the standard FE domain is enforced in the DG context. At this point we want to review various Γ-approximations as pictured in Fig. 3.4. Note that the approximation of the boundary is in general independent of the field interpolation. Due to the convenience in the integration, one typically uses piecewise linear patches in standard (low-order) eXtended finite element methods or low-order IB-DG methods. As can be readily observed, this approach will lead to

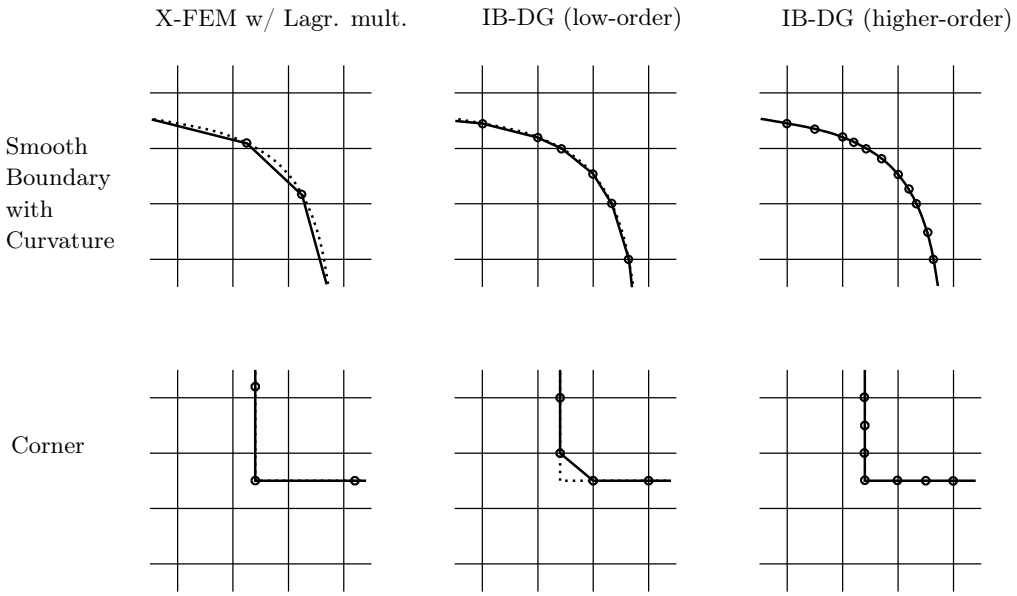

Figure 3.4: Schematic of various Γ-approximations: (left) X-FEM with Lagrange multiplier; (middle) low-order IB-DG; (right) higher-order IB-DG.

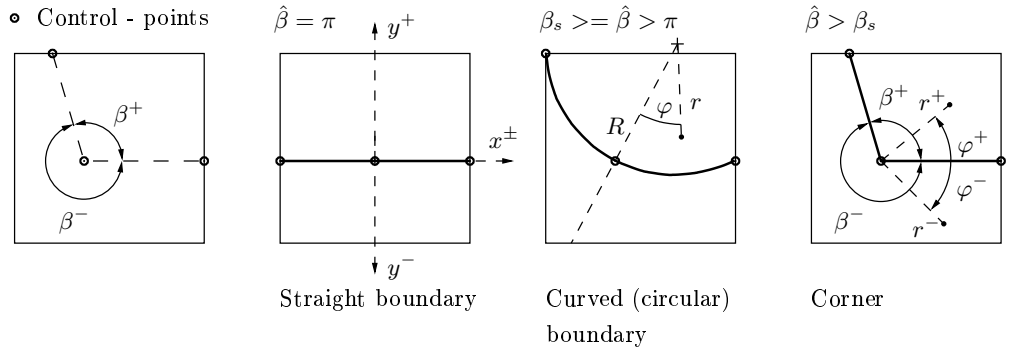

Figure 3.5: Schematic of basic geometric primitives used for higher-order Γ-approximation.

inaccuracies in the Γ-approximation which guide us to a higher-order approximation, built of nonlinear geometric primitives. We locally approach the Γ-boundary as sketched in Fig. 3.5: For each intersected element we calculate three *control-points* (see Fig. 3.5), each lying on Γ. Depending on the angle $\hat{\beta} = \max\{\beta^+, \beta^-\}$, we propose an automatic heuristic switch based on a user-defined parameter β_s.

- If $\hat{\beta} = \pi$, approximate Γ by a *straight line* through all three control-points.
- If $\beta_s \geq \hat{\beta} > \pi$, approximate Γ by a *circular curve* through all three control-points.
- If $\hat{\beta} > \beta_s$, approximate Γ by a *wedge* with vertex at the mid-control-point.

In our later examples, we set $\beta_s = 1.3\,\pi$ but this can be adjusted as needed by the user. Instead of an automatic switch, this can also be done by a user decision– e.g. by flagging certain nodes along the boundary as singular corners, and moreover one may utilize more complicated shapes from a user defined library to approximate the boundary at the required accuracy.

As mentioned before, by default, we use a low-order interpolation for all elements that are *not* intersected by Γ. For all elements intersected by Γ, we switch to a higher-order approximation that follows the boundary shape locally. For the three basic shapes we developed so far, we propose the following interpolations.

Straight Boundary

In the case of a straight boundary, for each side of the element one can use a local Cartesian coordinate system $\{x, y\}$ (see Fig. 3.5), and approximate the solution by polynomial spaces. In accordance with [53], this can be done by a linear (low-order) space

$$\Phi^h \in \text{span}\{1, x, y^{\pm}\}\,, \tag{3.19}$$

featuring 4 degrees of freedom per element. Note that this approximation will be used in the low-order IB-DG implementation for comparison in the next section. In our higher-order formulation we will use a quadratic space

$$\Phi^h \in \text{span}\{1, x, x^2, y^{\pm}, (y^2)^{\pm}, xy^{\pm}\}\,, \tag{3.20}$$

resulting in 9 degrees of freedom per element. This enables a more accurate gradient interpolation, and moreover avoids locking of the solution when non-constant gradients occur in an element.

In this notation we note that all modes labeled $\{(.)^{\pm}\} = \{(.)^+, (.)^-\}$ have to be counted twice as they are independently used to interpolate the field in each domain. Note that the interpolation space is designed to follow the boundary shape, which enables one to specify Dirichlet type boundary conditions in a strong sense. This is one major difference to the X-FEM method, where Dirichlet boundary conditions can only be enforced in a weak sense.

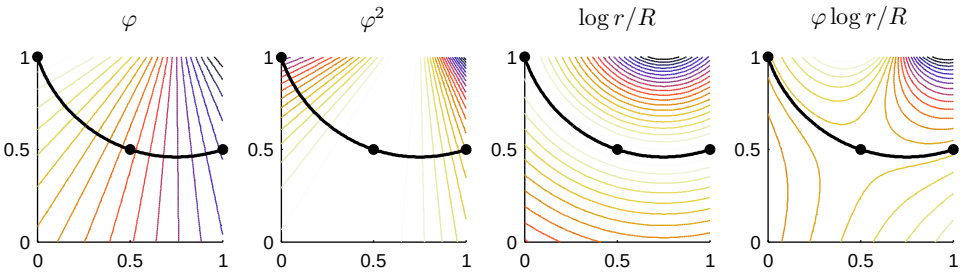

Figure 3.6: Shape functions for circular boundary.

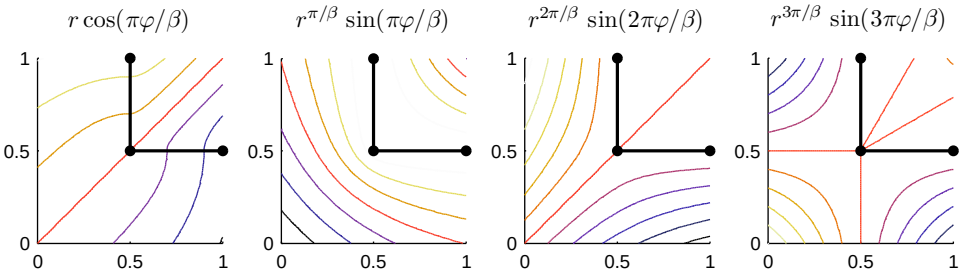

Figure 3.7: Shape functions for corner element.

Circular Boundary

In the case of a circular boundary approximation, we introduce the polar coordinate system $\{r, \varphi\}$ as shown in Fig. 3.5 and propose the shape functions

$$\Phi^h \in \text{span}\{1, \varphi, \varphi^2, \log(r/R)^{\pm}, \varphi \log(r/R)^{\pm}\}, \tag{3.21}$$

as pictured in Fig. 3.6 (viz.7 degrees of freedom). These functions are motivated by the analytical eigensolution of Poisson's equation near a circular boundary in two dimensions (see e.g. [78, §9.4]).

Corner Element

Lastly, we propose a corner interpolation using a polar coordinate system $\{r, \varphi\}$ as pictured in Fig. 3.5. In contrast to the circular boundary case, the coordinate center is now at the singular corner location. We assume

$$\Phi^h \in \text{span}\{1, r\cos(\pi\varphi/\beta), r^2\cos^2(\pi\varphi/\beta), r^{m\pi/\beta}\sin(m\pi\varphi/\beta)^{\pm}\}_{m=1}^{N}, \tag{3.22}$$

which again is motivated by near field solutions to Poisson's equation [78, §9.4]; see Fig. 3.7. Note that $m = 1$ represents the singularity in the gradient due to an entrant corner; modes $m > 1$ represent higher-order series expansions of the exact solution. We found the choice

$N = 3$ (9 degrees of freedom) for our numerical experiments in Section 3.5 sufficiently accurate. Higher choices of N will give more accurate results but potentially also lead to instabilities.

Inter-element Continuity

Since all intersected elements have locally defined solution parameters, one has to enforce continuity along the element boundaries. For simplicity, we employ a discontinuous Galerkin method with internal penalties (IP-DG) [79, 80, 81]. Alternatively one could utilize other DG methods such as Bassi-Rebay [82], the local discontinuous Galerkin [83], or the compact discontinuous Galerkin method [84]. These approaches improve upon IP-DG, but for our purpose of developing a proper boundary representation they are unneeded and we opt for the simplicity afforded by IP-DG.

The overall problem then reads: Find $\Phi^h \in \mathcal{P}_s^h$, such that (3.12) holds and

$$\Pi_{DG}(\Phi^h) = \sum_e \left\{ \int_{\Gamma_e} \langle q^h \rangle [\![\Phi^h]\!] \mathrm{da} - \frac{\alpha}{h_e} \int_{\Gamma_e} [\![\Phi^h]\!]^2 \mathrm{da} \right\} \rightarrow \text{stat.} \tag{3.23}$$

Here

$$[\![\Phi^h]\!] = \Phi^{h+} - \Phi^{h-}\,, \tag{3.24}$$

$$\langle q^h \rangle = \frac{1}{2}\left(q^{h+} + q^{h-}\right) \tag{3.25}$$

denote the jump and average of field or flux respectively across each element boundary Γ_e. The sum goes over all boundaries of intersected elements. The stability parameter α in this form is scaled by the local area-measure h_e of the element boundary. After the typical variation, together with (3.12) we arrive at a linear system, where with ease we can enforce Dirichlet type boundary conditions along Γ in a strong sense. Note that α in this work is a user-defined parameter that must be chosen high enough in order to satisfy coercivity of the weak form, and low enough to retain accuracy. Recent work by [85], [86], or [87] establish methods to estimate α based on the solution of a local eigen-value problem. For our purposes of benchmark testing we manually optimize α for the given examples.

Charge Loading

For the charge loading case, let us denote $\Phi^h = \sum_{j=1}^{nel} P_j \Phi_j$ with $P_j \in \mathcal{P}_s^h$ and the expansion coefficients Φ_j. Using a Galerkin discretization, one can write (3.12) and (3.23) in the algebraic form: Find $[\Phi_j]$ such that

$$\sum_j K_{ij}\Phi_j = q_i\,, \quad \forall i = 1, \ldots, nel\,, \tag{3.26}$$

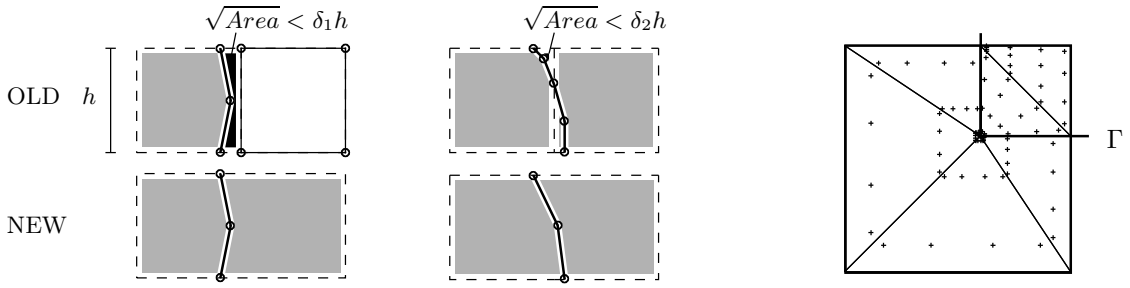

Figure 3.8: IB-DG: (left) element extensions; (right) Gauss integration of singular functions via generalized Duffy-trick [88].

where K_{ij} are the coefficients of the electrical stiffness, and q_i the equivalent fluxes for each degree of freedom. Let us now denote the set

$$\mathcal{J} = \{j \mid P_j(\mathbf{x}) \neq 0, \forall \mathbf{x} \in \Gamma\}\,, \tag{3.27}$$

which are the degrees of freedom in the intersected elements that are used to interpolate $\Phi^h = \bar{\Phi}$ along Γ. We now split $\mathcal{J}$ into $\mathcal{J} = \mathcal{J}_0 \cup \mathcal{J}_n$, with $\mathcal{J}_0 \cap \mathcal{J}_n = \emptyset$, where $\mathcal{J}_0$ is the set of all constant modes and $\mathcal{J}_n$ is the set of all higher modes. For charge loading on a conducting surface we then require

$$\Phi_j = \bar{\Phi}\,, \forall j \in \mathcal{J}_0\,, \quad \Phi_j = 0\,, \forall j \in \mathcal{J}_n\,, \quad \sum_{j \in \mathcal{J}_0} q_j = Q\,, \tag{3.28}$$

which are the equivalent forms to (3.17) and (3.18). From (3.26) we then derive: Find $[\Phi_j, \bar{\Phi}]$, $j \notin \mathcal{J}$, such that

$$\sum_{j \notin \mathcal{J}} K_{ij}\Phi_j + \sum_{j \in \mathcal{J}_0} K_{ij}\bar{\Phi} = q_i\,, \quad \forall i \notin \mathcal{J}\,, \tag{3.29}$$

$$\sum_{i \in \mathcal{J}_0}\sum_{j \notin \mathcal{J}} K_{ij}\Phi_j + \sum_{i \in \mathcal{J}_0}\sum_{j \in \mathcal{J}_0} K_{ij}\bar{\Phi} = Q\,. \tag{3.30}$$

for any given equivalent nodal fluxes q_i and total charge Q.

Integration

Before we proceed to the numerical examples, we point out some further details of the implementation. For elements intersected by a smooth boundary, we employ standard Gauss integration procedures via tessellation [59]. In elements featuring a sharp corner, we have to integrate a singular function of the form

$$\int_{\Delta_I} \epsilon\,(\pi/\beta)^2\, r^{-\gamma} \mathrm{da}\,, \tag{3.31}$$

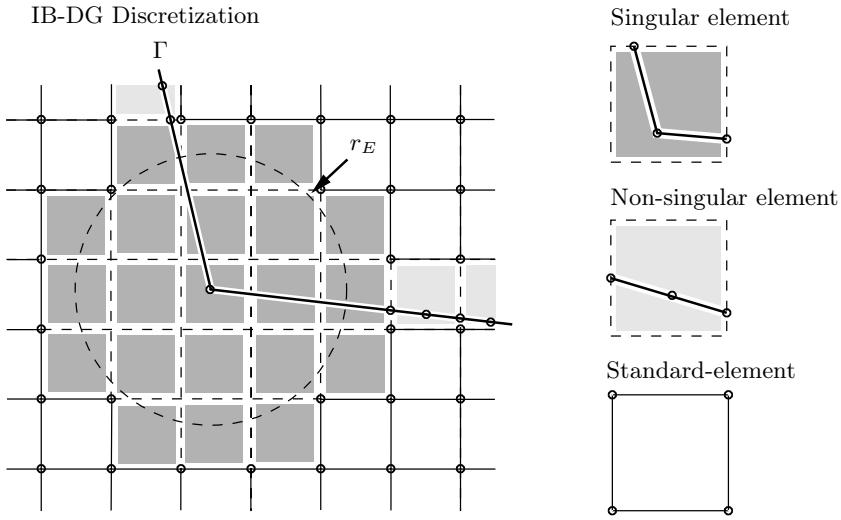

Figure 3.9: Singular element enhancement within enrichment radius r_E.

where $\gamma = 2 - 2\pi/\beta$ is the order of the singularity. As pictured in Fig. 3.8 (right), we divide elements by a Delaunay-triangularization into triangles Δ_I, such that the singularity is at one vertex. Following [88], we then use a generalized Duffy-trick to integrate each triangle with a proper Gauss-rule that respects the order of the singularity depending on the angle $\beta^{\pm}$.

Singular Corner Enrichment Radius

In accordance with [89] and [90] we observe that optimal convergence during mesh-refinement for the singular enrichment can only be achieved by enhancing all elements surrounding the singular point within a certain radius r_E (see Fig. 3.9). For each such element we refer to the same source of singularity, from which we measure the local coordinates $\{r, \varphi\}$ and from which we take the angle $\beta^{\pm}$. In this work, r_E is a user-defined parameter, which has been adjusted in the upcoming examples to sufficiently cover the effective radius of the singularity (see Section 3.5).

Element Extensions

Since one typically cannot control the boundary location, for example if one has moving bodies, bad element intersections may lead to ill-conditioning. To alleviate this problem, we follow a procedure similar to what was proposed in [91]. In two dimensions our strategy depends on how the elements are intersected. When two opposite sides are intersected (Fig. 3.8, left) and $\sqrt{Area} < \delta_1 h$, we extend the element to the next neighbor. When two adjacent sides are intersected (Fig. 3.8, middle) and $\sqrt{Area} < \delta_2 h$, we merge two intersected elements that share a common edge. Here, δ_1 and δ_2 are user-defined parameters that control

the range of element extensions. In rare cases it may occur that such merging will lead to a successive combining of elements into a very large element. For a structured mesh as pictured here, this can be avoided by consistently merging elements in only one coordinate direction. With unstructured meshes, one would have to consider a strategy that avoids such combinations.

Element Identification

In order to identify the various element-types, a level-set function is calculated for each solution iteration. In our examples we compute the signed-distance to the boundary Γ at each nodal location of the computational domain $\Omega^h = \mathcal{R}^h \cup \mathcal{V}^h$. This enables an identification of all intersected elements, for which we identify the element control-points as pictured in Fig. 3.5. Subsequently we check for singular elements and bad element intersections depending on the parameters r_E, δ_1, δ_2. Note again that all identified elements, that track the interface, feature a higher-order locally defined interpolation, whereas the remaining elements utilize a standard bi-linear interpolation as pictured in Fig. 3.9. This is a major advantage of the IB-DG method vs. X-FEM. Once the basic framework is implemented, one can easily define new elements and combine various element-types of different orders to obtain an optimal and efficient interpolation space for the problem at hand.

3.5 Numerical Examples

We now look at several examples where a straight forward analytical solution is accessible. In particular we will validate the accuracy and convergence during $h-$refinement. To this end we introduce the relative L2-error norms

$$||\Phi - \Phi^h||_\Omega / ||\Phi||_\Omega = \sqrt{\int_\Omega \left(\Phi^h - \Phi\right)^2 \mathrm{d}\Omega} \Big/ \sqrt{\int_\Omega \Phi^2 \mathrm{d}\Omega}\,, \tag{3.32}$$

for the bulk field in the computational domain Ω and

$$||\nabla_n\Phi - \nabla_n\Phi^h||_\Gamma / ||\nabla_n\Phi||_\Gamma = \sqrt{\int_\Gamma \left(\nabla_n\Phi^h - \nabla_n\Phi\right)^2 \mathrm{d}\Gamma} \Big/ \sqrt{\int_\Gamma \nabla_n\Phi^2 \mathrm{d}\Gamma}\,, \tag{3.33}$$

for the normal gradient along Γ.

Two Cylinders

In this example we assume two cylinders which are separated by a distance c and one is kept at a fixed potential $\Phi = \Phi_0$ while the other is kept at $\Phi = -\Phi_0$ (see Fig. 3.10). The analytical solution is given by (e.g. [92, p.15])

$$\Phi(\mathbf{x}) = \Phi_0 \log \frac{r_2(\mathbf{x})}{r_1(\mathbf{x})} \Big/ \log \frac{a}{d}\,, \tag{3.34}$$

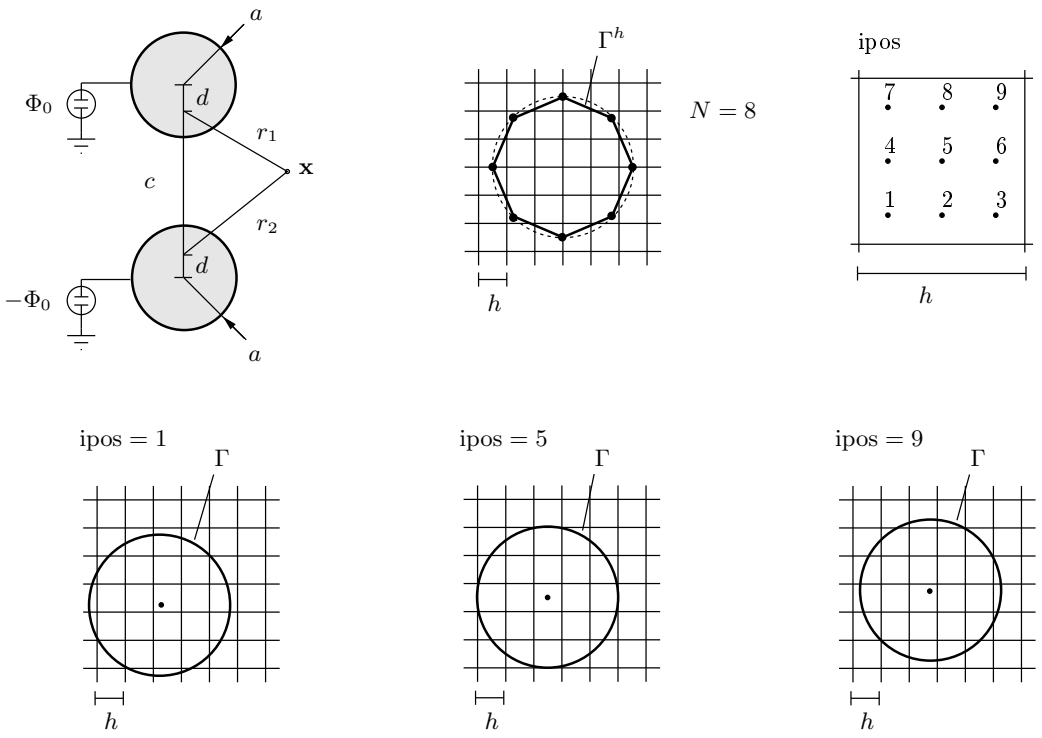

Figure 3.10: Two-cylinders example: schematic, discretization and various cylinder center positions (ipos).

where the cylinder radius a, r_1, r_2 are pictured in Fig. 3.10 and $d = c/2 - \sqrt{0.25c^2 - a^2}$.

For the numerical example we consider $\epsilon_{\mathcal{R}} = \epsilon_{\mathcal{V}} = \epsilon_{\mathcal{W}} = 1$, $\Phi_0 = 300$, $a = 0.1$ and $c = 0.5$. Note that in this example the potential along Γ is constant, so one can actually prescribe the solution $\Phi^h_{\mathcal{R}}$ inside the cylinders to be equal to the given boundary data Φ_0 and $-\Phi_0$ respectively. Thus, the definition of $\epsilon_{\mathcal{R}}$ is arbitrary. The background mesh covers the domain $\Omega = [0, 1]^2$, and has been refined from 25×25 to 200×200 elements; i.e. the element size $h = 1/25, \ldots, 1/200$. For ease of implementation, we discretize the cylinder surface (Γ^h) by N piecewise linear surface patches. Since we adopt the Lagrange multiplier space according to the surface discretization for X-FEM via Lagrange multipliers, N cannot be chosen arbitrarily in this case since the inf-sup condition must be satisfied. We found the best possible results by using 10 to 80 linear elements for each cylinder (Fig. 3.10), which corresponds to a ratio $l/h \approx 1.6$. In the case of the IB-DG method, there is no constraint on the surface discretization, and we used $N = 500$ to obtain an accurate representation of Γ. Following a sensitivity study as discussed later, we choose $\alpha = 100$ for the low-order IB-DG. For the higher-order IB-DG we choose $\alpha = 150$ and in addition use element extensions with $\delta_1 = 0.6$, $\delta_2 = 1$. No radius r_E needs to be specified in this example since no singularities are present.

Looking at typical results in Fig. 3.11(a-c), we readily observe two advantages of the

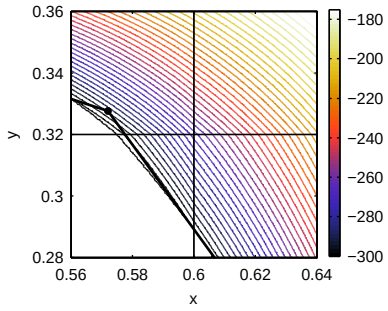

(a) Potential contour: XFEM (h=1/25).

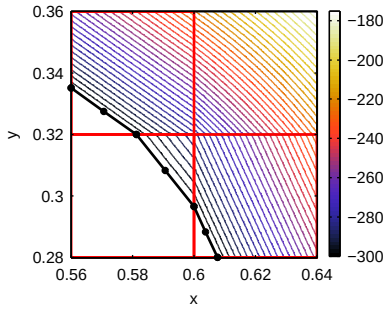

(b) Potential contour: IB-DG (low-order, h=1/25).

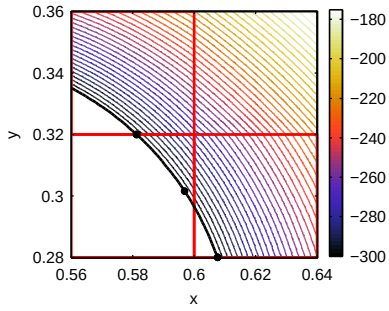

(c) Potential contour: IB-DG (higher-order, h=1/25).

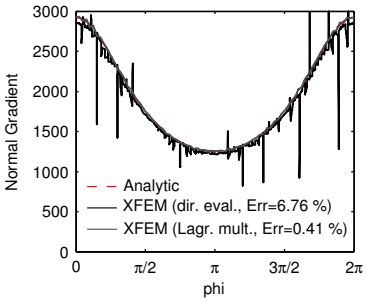

(d) Normal gradient: XFEM (h=1/200).

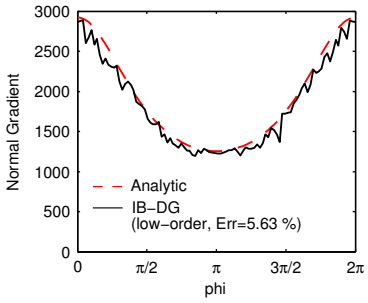

(e) Normal gradient: IB-DG (low-order, h=1/200).

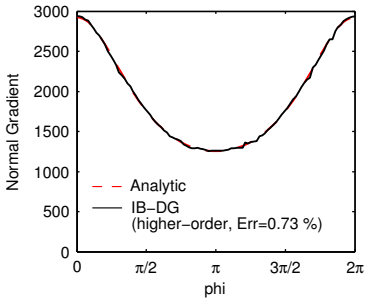

(f) Normal gradient: IB-DG (higher-order, h=1/200).

Figure 3.11: Two-cylinders example: (top) detailed potential contour, Γ-boundary and background mesh with control-points; (bottom) normal gradient along cylinder surface.

higher-order IB-DG method: First, the potential field follows the surface discretization much more accurately than in the case of a low-order IB-DG method or X-FEM. Second, the constraint $\Phi = \bar{\Phi}$ is enforced exactly on the boundary, which cannot be guaranteed by X-FEM. Looking at Fig. 3.11(d-f), the advantage of the higher-order enhancement becomes even more obvious. Whereas X-FEM and low-order IB-DG give very poor quality of the gradient along Γ, the error for higher-order IB-DG is noticeably better. Inaccuracies in the gradient as seen in Fig. 3.11(d) are a well known issue to the X-FEM community [61]. Methods exist to reconstruct more accurate gradients by post-processing steps, but this is not necessary for the proposed higher-order IB-DG method. Note that the Lagrange multiplier in this example does give a very accurate representation of the normal flux on the boundary, and only small oscillations occur. However, this is a best case scenario as we optimized $\mathcal{L}^h$, and any other choice will easily give much worse results with possibly

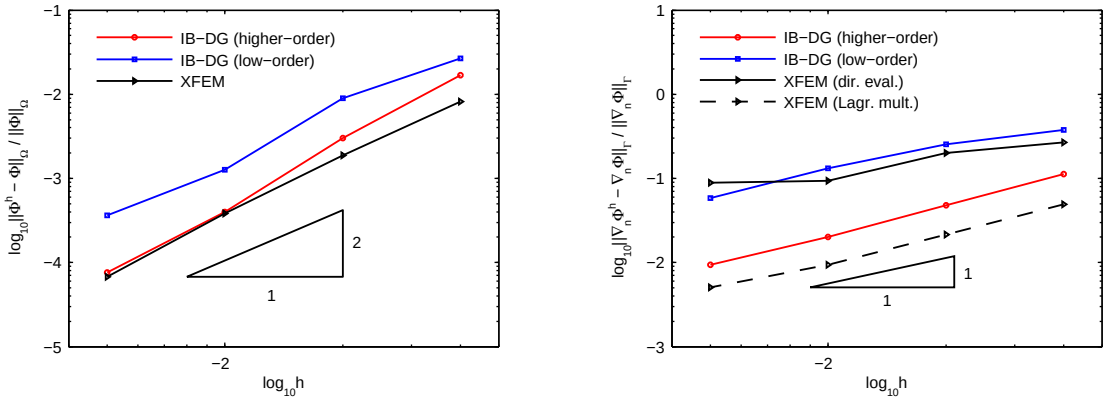

Figure 3.12: Two-cylinders example, maximum L2-error convergence: (left) bulk field; (right) normal gradient.

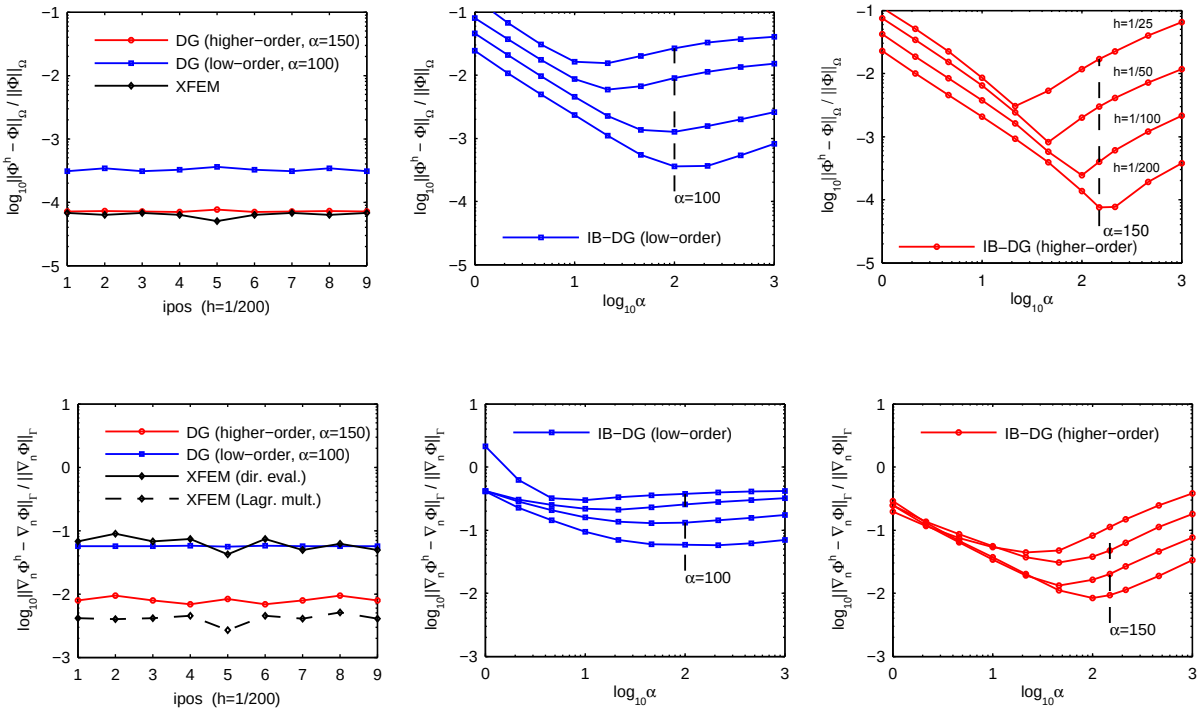

Figure 3.13: Two-cylinders example: sensitivity of bulk- and gradient-error (left) with respect to interface location (ipos); (center and right) with respect to stability parameter (α) for various h-values as indicated in upper right figure.

large oscillations. Moreover, as will be observed in the next example, the standard Lagrange multiplier approach will fail whenever singularities in the gradient field are involved. The convergence during h-refinement of the field Φ and the normal gradient field is shown in Fig. 3.12. All methods show second and first order convergence of the field and the normal gradient error respectively. The gradient approximation of the higher-order IB-DG method and the Lagrange-multiplier are about one order of magnitude more accurate than the low-order IB-DG method and X-FEM, but the rates are the same.

Sensitivity (interface location)

In a general application of the method, the elements can be intersected by the boundary in any possible way. Thus we test over a certain range of configurations and report in our convergence plots worst case scenarios as an upper bound on the error. To give a full picture, Fig. 3.13(left) shows the error as we vary the cylinder center as pictured in Fig. 3.10(right and bottom). We observe very little variation of the error, which has also been confirmed in the examples that follow.

Sensitivity (α)

As indicated previously, one needs to select the stabilization parameter α. In order to pick α for the IB-DG methods, we plot the field- and gradient-error in Fig. 3.13(center and right). The optimum α depends on the mesh refinement h. In this and the upcoming examples, we choose a minimum α such that optimum convergence during h-refinement was achieved over the range of h-values examined. For any given discretization h, however, other choices of α may give more accurate results in terms of the error constant. This manual procedure ensures that we observe full rates of convergence. However, in a general setting one should employ an automatic parameter selection scheme. We also note that the sensitivity with respect to α is essentially independent of the degree of intersection as resulting from the varying cylinder positions described in the previous paragraph [see Fig. 3.13(left)].

Rectangular Corner

For the second example we assume a rectangular body within a box, where the potential at the boundary Γ is held at $\Phi_0 = 300$ and at the border of the box is set to zero (see Fig. 3.14). We denote the length of the rectangular boundary as L and consequently the gap between Γ and the outer box as g. When the gap-to-length ratio $g/L << 1$, we set the origin of a Cartesian coordinate system (x, y) at the lower left corner of the outer box, and one can find the analytical solution near this corner as pointed out in [93, p.21] via a conformal mapping $f : \tilde{z} \to z$, with $z, \tilde{z} \in \mathbb{C}$. Here $z = x + iy$ represents the coordinate location in the physical space, whereas $\tilde{z} = \tilde{r}\cos(\tilde{\varphi}) + i\tilde{r}\sin(\tilde{\varphi})$ follows rays of corresponding potentials $\Phi = \Phi_0\tilde{\varphi}/\pi$

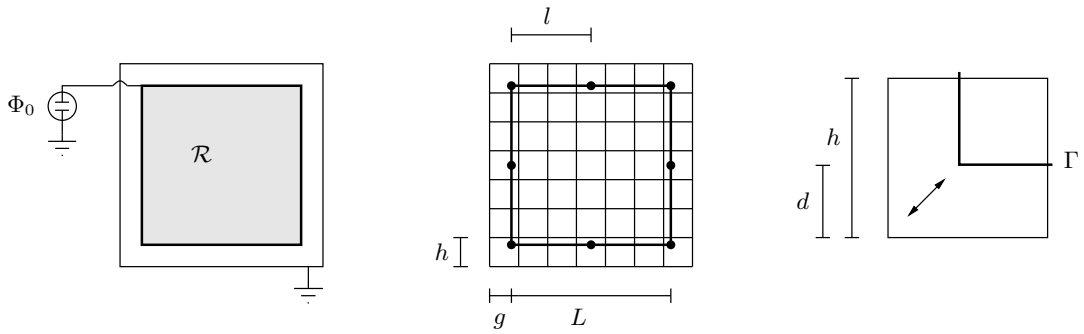

Figure 3.14: Rectangular-corner example: schematic, discretization and varying interface location.

for any fixed angle $\tilde{\varphi} \in [0, \pi]$. The mapping f is given by

$$f(\tilde{z}) = \frac{2g}{\pi} \left[\arctan \sqrt{\frac{\tilde{z}-1}{\tilde{z}+1}} + \frac{1}{2} \ln \frac{1 + \sqrt{\frac{\tilde{z}-1}{\tilde{z}+1}}}{1 - \sqrt{\frac{\tilde{z}-1}{\tilde{z}+1}}} \right], \tag{3.35}$$

and we find the solution at $z = (x, y)$ formally by taking the inverse $\tilde{z} = f^{-1}(z)$. The normal gradient then is

$$\nabla_n \Phi = \frac{\Phi_0}{g} \sqrt{\frac{\tilde{z}-1}{\tilde{z}+1}}. \tag{3.36}$$

For the numerical example we consider $\epsilon_{\mathcal{R}} = \epsilon_{\mathcal{V}} = 1$, $\Phi_0 = 300$, and vary L to change the interface location. The background mesh covers the domain $[0, 1]^2$, and has been refined from 25×25 to 200×200 elements; i.e. the element size $h = 1/25, \ldots, 1/200$. Again, for X-FEM via Lagrange multipliers, the corner surface discretization (Γ^h) is not arbitrary and has been optimized to 8 to 64 linear elements per side ($l/h \approx 2.5$). For the low-order DG we choose $\alpha = 20$, whereas for the higher-order DG we choose $\alpha = 1000$, $\delta_1 = 0.6$, $\delta_2 = 1$. Due to the presence of a singularity, in the higher-order IB-DG we use a geometric enrichment around the singularity with $r_E = 0.04$. We chose r_E to sufficiently cover the effective radius of the singularity as observed in the numerical examples. In lieu of (3.36) we required that $\nabla_n \Phi < 1.15(\Phi_0/g)$ for all points outside the radius r_E on the boundary Γ [see also Fig. 3.15(d-f) as indicated by the dashed line, and Fig. 3.15(bottom)].

Looking at typical results in Fig. 3.15, we make similar observations as in the previous example but even more distinct. The low-order X-FEM and IB-DG clearly fail to interpolate the potential around the corner [Fig. 3.15(a,b)] and approximate the gradient very poorly even for high refinements [Fig. 3.15(g,h)]. On the other hand, the higher-order IB-DG approach shows excellent performance as seen in Fig. 3.15(c,i).

In order to perform a convergence study for h-refinement, at each refinement we vary the ratio $d/h \in [0, \ldots, 1]$ as pictured in Fig. 3.14. Three cases are plotted for the higher-order IB-DG in Fig. 3.15(d-f). As Γ comes closer to the element boundary, our method will

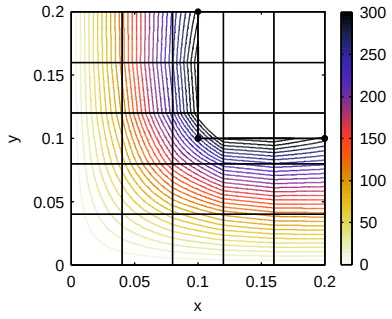

(a) Potential contour: XFEM (h=1/25).

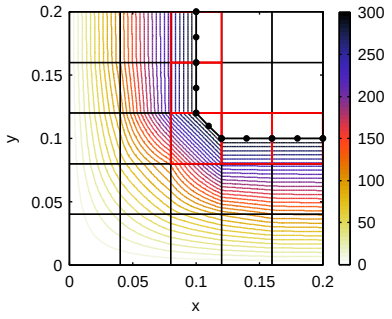

(b) Potential contour: IB-DG (low-order, h=1/25).

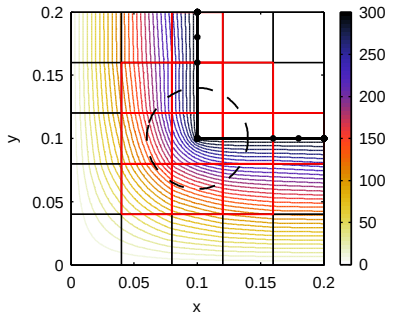

(c) Potential contour: IB-DG (higher-order, h=1/25).

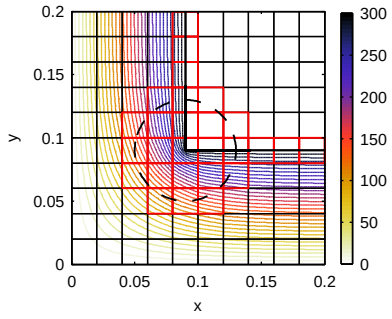

(d) Potential contour: IB-DG (higher-order, h=1/50, d/h=0.5).

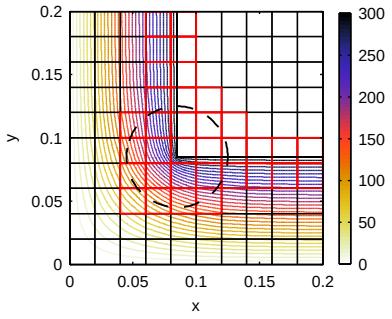

(e) Potential contour: IB-DG (higher-order, h=1/50, d/h=0.25).

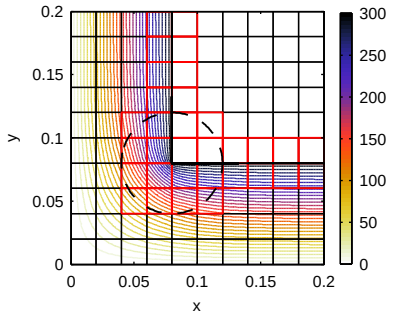

(f) Potential contour: IB-DG (higher-order, h=1/50, d/h=0).

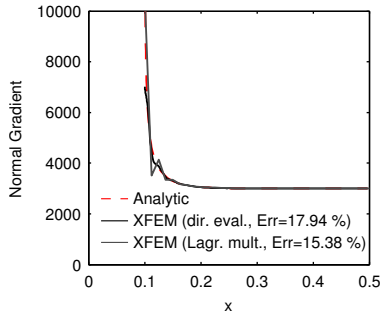

(g) Normal gradient: XFEM (h=1/200).

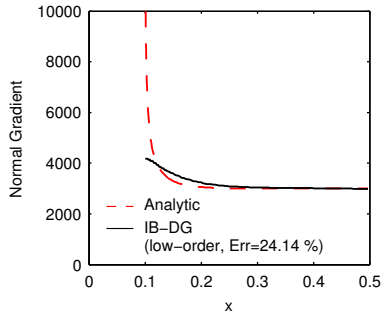

(h) Normal gradient: IB-DG (low-order, h=1/200).

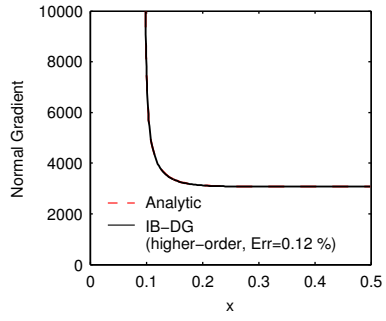

(i) Normal gradient: IB-DG (higher-order, h=1/200).

Figure 3.15: Corner example: (top) resulting potential contour, Γ-boundary and background mesh; (bottom) normal gradient along Γ-boundary.

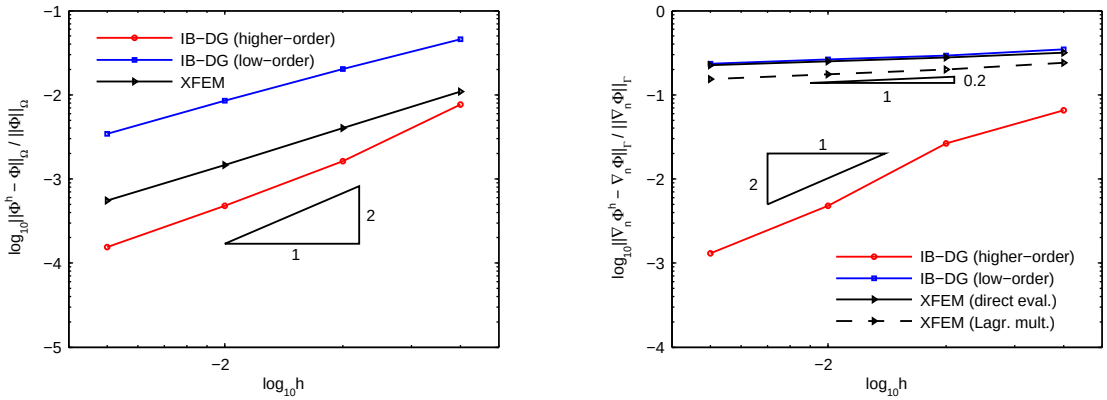

Figure 3.16: Corner example, voltage loading, maximum L2-error convergence: (left) bulk field; (right) normal gradient.

automatically extend the DG element region (red element boundaries) and merge neighboring elements. The upper bounds on the error for the bulk- and gradient-fields are shown in Fig. 3.16. The higher-order IB-DG method clearly outperforms the low-order approaches. We observe second order convergence in the bulk field as well as the gradient field for the higher-order IB-DG, whereas the low-order methods lock with respect to the surface gradient error. Note especially that despite the previous example with a circular boundary, the Lagrange multiplier is unable to deliver accurate results in this case. Moreover, any post-processing will have difficulties to reconstruct the singular gradients around the corner from a low-order bulk field interpolation.

Charge Loading

We next test the case where a total charge Q is imposed on a conductor. We take the geometry from the rectangular boundary given in the previous example. From the analytical approximation, we calculate

$$Q = -\int_\Gamma \epsilon_\mathcal{V}(\nabla\Phi\cdot\mathbf{n})\,\mathrm{da} = -8\epsilon_\mathcal{V}\Phi_0/\pi\int_{\tilde{z}_0}^{-1}\tilde{z}^{-1}\,\mathrm{da}\,, \tag{3.37}$$

where we find $\tilde{z}_0 = f^{-1}(z_0)$, with $z_0 = (0.5, g)$ and the mapping f as in (3.35). We tabulate typical values for Q at $\Phi_0 = 300$ and various g in Table 3.1.

For the numerical test we use the same parameters as from the previous example, except we now employ Q as a given load and solve consequently for $\Phi^h, \bar{\Phi}$ via (3.17) in the X-FEM context, or (3.29) and (3.30) for the IB-DG methods. We plot the convergence of the potential and gradient field in Fig. 3.17, as well as for the relative error of the floating potential $\bar{\Phi}$ in Fig. 3.18. We observe similar results as reported in the previous example.

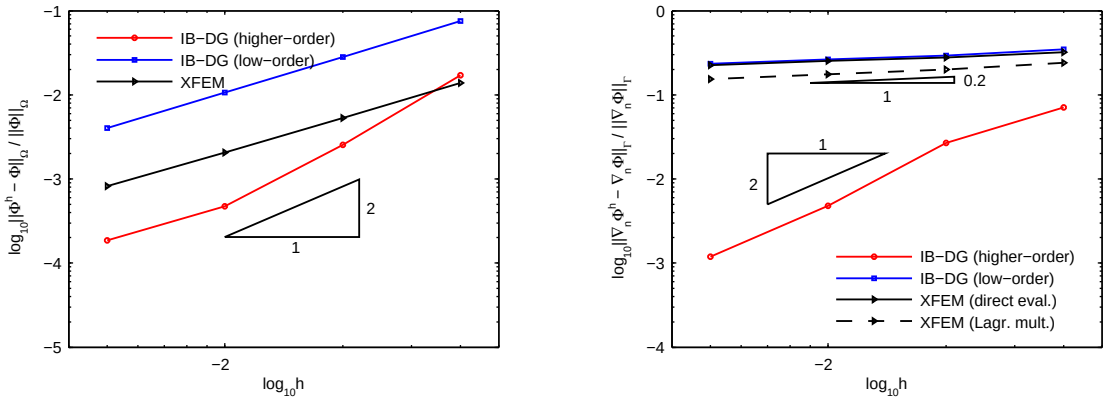

Figure 3.17: Corner example, charge loading, maximum L2-error convergence: (left) bulk field; (right) normal gradient.

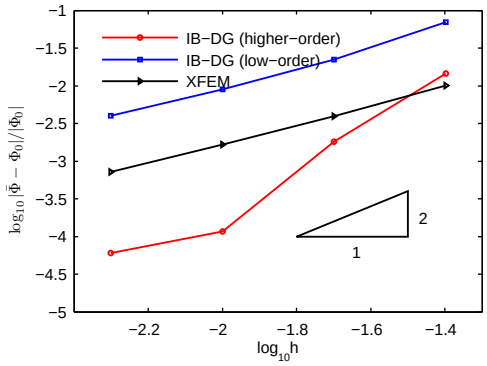

Figure 3.18: Corner example, charge loading: convergence of floating potential $\bar{\Phi}$.

g	0.0900	0.0925	0.095	0.0975	0.1000
$\tilde{z}_0$	$-3.9505 \cdot 10^6$	$-2.4648 \cdot 10^6$	$-1.5766 \cdot 10^6$	$-1.0318 \cdot 10^6$	$-6.8970 \cdot 10^5$
Q	$-1.1604 \cdot 10^4$	$-1.1243 \cdot 10^4$	$-1.0902 \cdot 10^4$	$-1.0578 \cdot 10^4$	$-1.0270 \cdot 10^4$

Table 3.1: Charge loading example: Typical $\tilde{z}_0$ and Q for various gaps g at $\Phi_0 = 300$.

Our high-order IB-DG outperforms the other methods especially with respect to the normal gradient error.

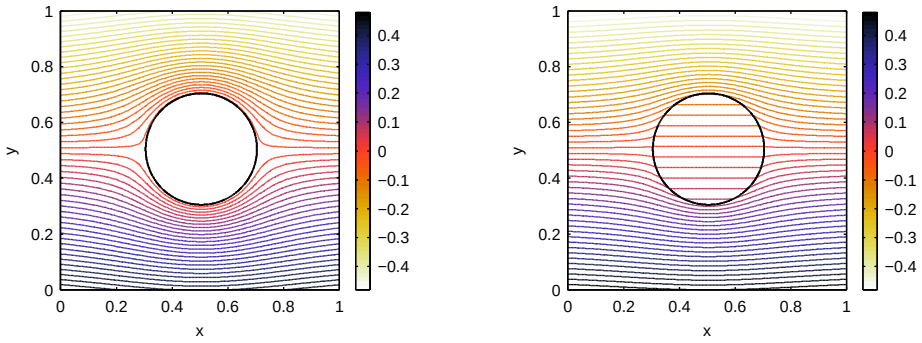

Figure 3.19: Dielectric-interface example: resulting potential contour IB-DG (higher-order, h=1/100) for (left) $\epsilon_{\mathcal{R}} = 10^6$ and (right) $\epsilon_{\mathcal{R}} = 3$.

Dielectric Interface

In our last example we test the capability to calculate penetrating fields as well as a discontinuous material permittivity across dielectric-dielectric interfaces. To this end we assume a cylinder with radius R and permittivity $\epsilon_{\mathcal{R}}$ placed in a uniform e-field of strength E_0 in the surrounding infinite space with permittivity $\epsilon_{\mathcal{V}}$. Using a polar coordinate system $\{r, \varphi\}$ with origin at the cylinder center, the analytical solution is given by

$$\Phi = \begin{cases} -\frac{2\epsilon_{\mathcal{V}}}{\epsilon_{\mathcal{R}}+\epsilon_{\mathcal{V}}} E_0 r \sin\varphi\,, & \text{if } r < R\,, \\ -E_0 r \sin\varphi + \frac{\epsilon_{\mathcal{R}}-\epsilon_{\mathcal{V}}}{\epsilon_{\mathcal{R}}+\epsilon_{\mathcal{V}}} E_0 \frac{R^2}{r} \sin\varphi\,, & \text{if } r \geq R\,, \end{cases} \tag{3.38}$$

which features a constant electrical field in the interior of the cylinder. For the numerical example we consider the radius $R = 0.2$, permittivity $\epsilon_{\mathcal{V}} = 1$, and e-field strength $E_0 = 1$. We test two different scenarios $\epsilon_{\mathcal{R}} = 10^6$ and $\epsilon_{\mathcal{R}} = 3$. The background mesh has been refined from 25×25 to 200×200 elements. For the Lagrange multiplier space we use $N = 15, \ldots, 120$ linear elements which corresponds to a ratio $l/h \approx 2.1$ to maintain stability. For the low-order IB-DG we choose $\alpha = 200$, and $\alpha = 450$ for the higher-order IB-DG. In addition we use element extensions with $\delta_1 = 0.6$, $\delta_2 = 1$. No radius r_E needs to be specified since no singularities are present. In this example we impose fixed Dirichlet boundary conditions along the boundary of the computational domain, as we have calculated from the analytical solution.

A typical contour plot for the two different $\epsilon_{\mathcal{R}}$ is shown in Fig. 3.19, which nicely shows the constant e-field inside the cylinder. As can be expected, $\epsilon_{\mathcal{R}} = 10^6$ enforces a quasi-vanishing electrical field inside the cylinder, whereas $\epsilon_{\mathcal{R}} = 3$ allows a penetrating field. Since for both $\epsilon_{\mathcal{R}}$ we made similar numerical observations, we will focus on $\epsilon_{\mathcal{R}} = 3$ in the following. We draw attention to the detailed point-wise error maps in Fig. 3.20(a-c) around the boundary: For X-FEM we have the large errors occurring near the boundary location, whereas for the IB-DG methods the error concentrates near the element edges. This is expected, since for X-

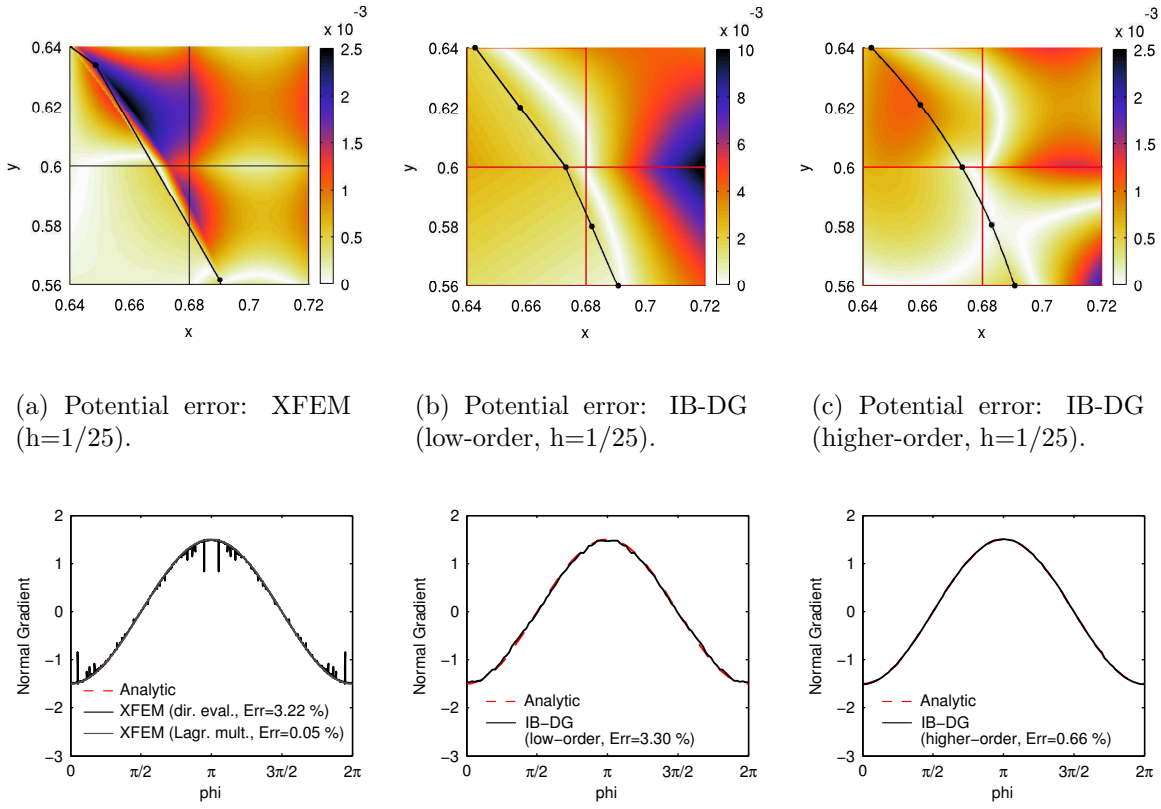

(a) Potential error: XFEM (h=1/25).

(b) Potential error: IB-DG (low-order, h=1/25).

(c) Potential error: IB-DG (higher-order, h=1/25).

(d) Normal gradient: XFEM (h=1/200).

(e) Normal gradient: IB-DG (low-order, h=1/200).

(f) Normal gradient: IB-DG (higher-order, h=1/200).

Figure 3.20: Dielectric-interface example: (top) detailed potential error $|\Phi^h - \Phi|$, Γ-boundary and background mesh with control-points; (bottom) normal gradient along Γ-boundary.

FEM one enforces continuity along Γ in a weak sense, whereas for the IB-DG based methods continuity along Γ is enforced in a strong sense, and continuity along element boundaries of the intersected elements is enforced in a weak sense. When looking at the normal gradients in Fig. 3.20(d-e), we observe a smooth approximation via the Lagrange multiplier and higher-order IB-DG, whereas the direct evaluation via X-FEM and low-order IB-DG show some error spikes and more jittery behavior. This is reflected in the convergence plots in Fig. 3.21, where the error constants for X-FEM with Lagrange multipliers and high-order IB-DG are smaller. Nevertheless all methods show the same order of convergence for this example.

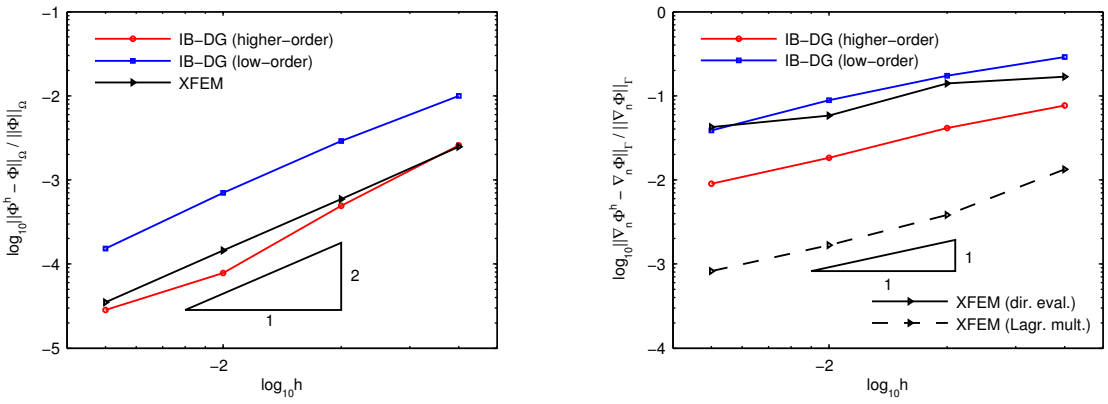

Figure 3.21: Dielectric-interface example, maximum L2-error convergence: (left) bulk field; (right) normal gradient.

Chapter 4

Eulerian-Lagrangian Finite Element Method

In this chapter, we present a new implementation to solve the coupled electro-mechanical problem by a mixed Eulerian-Lagrangian finite element method with embedded boundary conditions. Particular focus is put on the accurate representation of the Maxwell surface traction in the presence of singularities in the electrical field, and changes in topology when two bodies come into contact. We use a Lagrangian finite element method to track the mechanical motion, and a fixed Eulerian method to solve for the electrical field. Any nonlinear boundary features or singularities in the electrical field are captured by the high-order immersed boundary method as developed in the previous chapter. Traditional Lagrangian-Lagrangian or arbitrary Lagrangian-Eulerian (ALE) methods encounter deficiencies, for example, when dealing with mesh distortion due to large deformations, or topology changes due to contacting bodies. The presented Eulerian-Lagrangian approach addresses these issues in a natural way. We develop an implicit scheme based on the mid-point rule, as well as an explicit scheme based on the centered-difference method, with the incorporation of energy conserving, frictionless contact algorithms for an elastic-to-rigid-surface contact. The performance of the proposed method is assessed for several benchmark tests: the electro-static force vector around a singular corner, the quasi-static pull-in of an electro-mechanically actuated switch, the excitation of a carbon nanotube at resonance, and the cyclic impact simulation of a micro-electro-mechanical resonant-switch. We report improved accuracy for the high-order method as compared to low-order methods, and linear convergence in the iterative solution of the staggered scheme.

The outline of the chapter is as follows: In Section 4.1 and 4.2 we state the weak form of the mechanical and electrical problem. In Section 4.3 and 4.4, the Maxwell traction and mechanical contact treatment are discussed, before the algorithmic solution in Section 4.5 and numerical benchmark examples in the following sections are presented.

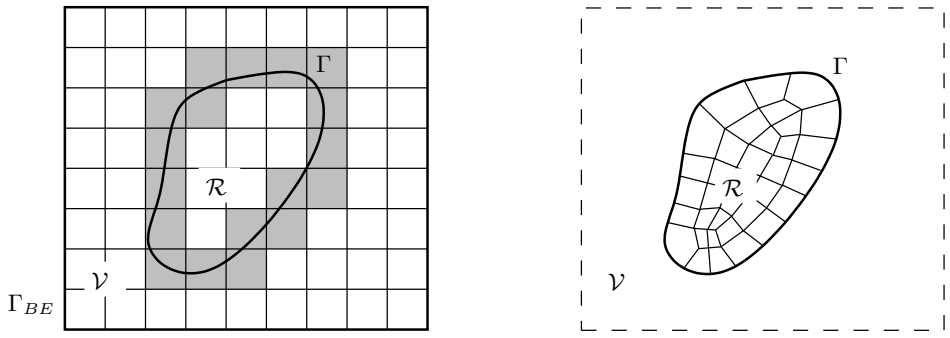

Figure 4.1: Discretization in space: (left) Eulerian finite element mesh with immersed boundary for the electrical field; (right) Lagrangian finite element mesh for the mechanical motion.

4.1 Mechanical Boundary Value Problem

In order to derive the weak form for the mechanical balance law, by (2.7) and (2.9), we note that for the Cauchy stress along the Neumann boundary, Γ_t: $\mathbf{T}^{-}\mathbf{n} = \bar{\mathbf{t}}_a + \mathbf{T}^{+}_{M}\mathbf{n}$, where $\bar{\mathbf{t}}_a = \boldsymbol{\sigma}^{+}\mathbf{n}$ is the applied (mechanical) traction due to external forces, and $\mathbf{T}^{+}_{M}\mathbf{n}$ the boundary traction due to external electrical fields. Here, the superscripts $(.)^{-}$ and $(.)^{+}$ indicate the limit as we approach the boundary Γ from inside $\mathcal{R}$, or from outside $\mathcal{R}$ respectively. From (2.2) we derive the mechanical weak form: Given initial conditions $\mathbf{u}(t_0) = \mathbf{u}_0$, $\dot{\mathbf{u}}(t_0) = \dot{\mathbf{u}}_0$ at $t = t_0$, find $\mathbf{u} \in \mathcal{U}_s$, such that

$$\int_{\mathcal{R}} \delta\mathbf{u} \cdot \rho\ddot{\mathbf{u}} \,\mathrm{dv} + \int_{\mathcal{R}} \nabla\delta\mathbf{u} \cdot \mathbf{T} \,\mathrm{dv} = \int_{\mathcal{R}} \delta\mathbf{u} \cdot \rho\bar{\mathbf{b}} \,\mathrm{dv} + \int_{\Gamma_t} \delta\mathbf{u} \cdot \left(\bar{\mathbf{t}}_a + \mathbf{T}^{+}_{M}\mathbf{n}\right) \mathrm{da}\,, \tag{4.1}$$

for all admissible variations $\delta\mathbf{u} \in \mathcal{U}_v$ at any $t > t_0$, together with given data $\mathbf{u} = \bar{\mathbf{u}}$ on the Dirichlet boundary $\Gamma_{\mathbf{u}}$. Here, the spaces $\mathcal{U}_s$ and $\mathcal{U}_v$ are suitable subspaces of H^1.

Upon a Lagrangian discretization in space [see Fig. 4.1(right)], we get the semi-discrete variational form of the mechanical problem: Find $\mathbf{u}^h \in \mathcal{U}^h_s$, such that

$$\int_{\mathcal{R}} \delta\mathbf{u}^h \cdot \rho\ddot{\mathbf{u}}^h \,\mathrm{dv} + \int_{\mathcal{R}} \nabla\delta\mathbf{u}^h \cdot \mathbf{T}^h \,\mathrm{dv} = \int_{\mathcal{R}} \delta\mathbf{u}^h \cdot \rho\bar{\mathbf{b}} \,\mathrm{dv} + \int_{\Gamma_t} \delta\mathbf{u}^h \cdot \left(\bar{\mathbf{t}}_a + \mathbf{T}^{+}_{M}\mathbf{n}\right) \mathrm{da}\,, \tag{4.2}$$

for all (admissible) variations $\delta\mathbf{u}^h \in \mathcal{U}^h_v$ at any $t > t_0$. Let us denote $\mathbf{u}^h = \sum_i N_i\mathbf{u}_i$, $\dot{\mathbf{u}}^h = \sum_i N_i\dot{\mathbf{u}}_i$, $\ddot{\mathbf{u}}^h = \sum_i N_i\ddot{\mathbf{u}}_i$ with $N_i \in \mathcal{U}^h$ and the expansion coefficients $\mathbf{U} = [\mathbf{u}_i]$, $\dot{\mathbf{U}} = [\dot{\mathbf{u}}_i]$, $\ddot{\mathbf{U}} = [\ddot{\mathbf{u}}_i]$. Using a Galerkin discretization, we can bring (4.2) into the algebraic form: Given $\mathbf{U}_0$, $\dot{\mathbf{U}}_0$, find $\mathbf{U}$ such that

$$\mathbf{M}\ddot{\mathbf{U}} + \mathbf{R}_{div} = \mathbf{F}_{ext}\,, \tag{4.3}$$

for all time instants $t > t_0$, where $\mathbf{M}$ is the mass matrix, $\mathbf{R}_{div}$ the stress-divergence term of the mechanical linear momentum balance, and $\mathbf{F}_{ext}$ the mechanical traction due to external

forces. We encounter two types of electrical forces on the continuum: A body force due to internal fields, and a surface traction due to the external electrical field. As mentioned earlier, the total Cauchy-stress $\mathbf{T}$ can be split into a purely mechanical part $\mathbf{T}_m$ and an electrical part $\mathbf{T}_e$ given by (2.31), and (2.32) respectively. Consequently we apply an additive split to $\mathbf{R}_{div} = \mathbf{R}_{div,m} + \mathbf{R}_{div,e}$, where

$$\mathbf{R}_{div,m} \leftarrow \int_{\mathcal{R}} \nabla\delta\mathbf{u}^h \cdot \mathbf{T}_m \,\mathrm{dv}\,, \tag{4.4}$$

$$\mathbf{R}_{div,e} \leftarrow \int_{\mathcal{R}} \nabla\delta\mathbf{u}^h \cdot \mathbf{T}_e \,\mathrm{dv}\,, \tag{4.5}$$

with $\mathbf{R}_{div,m}$ being the classical, purely mechanical stress-divergence term, and $\mathbf{R}_{div,e}$ the contribution of electrical body forces. In the following we will assume that $\mathbf{F}_{ext}$ is split into

$$\mathbf{F}_{ext} = \mathbf{F}_{contact} + \mathbf{F}_{dis} + \mathbf{F}_M^+\,, \tag{4.6}$$

viz., the surface traction $\mathbf{F}_{contact}$ due to mechanical contact, the dissipative force $\mathbf{F}_{dis}$ for example due to friction or absorbing boundary conditions, and the surface traction $\mathbf{F}_M^+$ due to external electrical fields.

4.2 Review: Electrical Boundary Value Problem

In this section, the electro-static problem as discussed in Chapter 3 is briefly reviewed. For a linear dielectric material, we have to find $\Phi_{\mathcal{R}}^h, \Phi_{\mathcal{V}}^h \in \mathcal{P}^h$, such that

$$\int_{\mathcal{R}} \epsilon_{\mathcal{R}} \nabla\delta\Phi_{\mathcal{R}}^h \cdot \nabla\Phi_{\mathcal{R}}^h \,\mathrm{dv} + \int_{\mathcal{V}} \epsilon_{\mathcal{V}} \nabla\delta\Phi_{\mathcal{V}}^h \cdot \nabla\Phi_{\mathcal{V}}^h \,\mathrm{dv} = -\int_{\Gamma_{BE}} q_{\mathcal{V}} \delta\Phi_{\mathcal{V}}^h \,\mathrm{da}\,, \tag{4.7}$$

for all $\delta\Phi_{\mathcal{R}}^h, \delta\Phi_{\mathcal{V}}^h \in \mathcal{P}^h$ along with the requirement $\Phi_{\mathcal{V}}^h = \Phi_{\mathcal{R}}^h = \bar{\Phi}(s)$ on Γ^h (for *Case 1* and *2*), and $\Phi_{\mathcal{V}}^h = \Phi_{\mathcal{R}}^h$ on Γ^h (for *Case 3*). Note that in the context of X-FEM we enforced the last requirements in a weak sense via Lagrange-multiplier. As demonstrated for $\Phi_{\mathcal{V}}^h = \bar{\Phi}$ on Γ^h, this resulted in: Find $(\Phi_{\mathcal{V}}^h, \lambda^h) \in \mathcal{P}^h \times \mathcal{L}^h$, such that (4.7) holds, and such that

$$\Pi_{LM}(\Phi_{\mathcal{V}}^h, \lambda^h) = \int_{\Gamma} \lambda^h \left(\Phi_{\mathcal{V}}^h - \bar{\Phi}\right) \mathrm{da} \tag{4.8}$$

will be rendered stationary. For the charge loading case for a given charge Q on a conductor, we modify (4.8) to: Find $(\Phi_{\mathcal{V}}^h, \lambda^h, \bar{\Phi}) \in \mathcal{P}^h \times \mathcal{L}^h \times \mathbb{R}$, such that (4.7) holds, and such that

$$\Pi_{LM}(\Phi_{\mathcal{V}}^h, \lambda^h, \bar{\Phi}) = \int_{\Gamma} \lambda^h \left(\Phi_{\mathcal{V}}^h - \bar{\Phi}\right) \mathrm{da} + Q\bar{\Phi} \tag{4.9}$$

becomes stationary.

In the case of the immersed boundary DG method, we required:

$$\Pi_{DG}(\Phi^h) = \sum_e \left\{ \int_{\Gamma_e} \langle q^h \rangle [\![\Phi^h]\!] \mathrm{da} - \frac{\alpha}{h_e} \int_{\Gamma_e} [\![\Phi^h]\!]^2 \mathrm{da} \right\} \rightarrow \text{stat.} \tag{4.10}$$

where we can enforce Dirichlet type boundary conditions $\Phi^h = \bar{\Phi}$ along $\bar{\Gamma}$ strongly. In the charge loading case, recall the problem: Find $[\Phi_j, \bar{\Phi}]$ such that

$$\sum_{j \notin \mathcal{J}} K_{ij} \Phi_j + \sum_{j \in \mathcal{J}_0} K_{ij} \bar{\Phi} = q_i \,, \quad \forall i \notin \mathcal{J} \,, \tag{4.11}$$

$$\sum_{i \in \mathcal{J}_0} \sum_{j \notin \mathcal{J}} K_{ij} \Phi_j + \sum_{i \in \mathcal{J}_0} \sum_{j \in \mathcal{J}_0} K_{ij} \bar{\Phi} = Q \,, \tag{4.12}$$

for any given equivalent nodal fluxes q_i and total charge Q, where K_{ij} are the coefficients of the electrical stiffness.

For future reference, we summarize the electro-static problem into an algebraic form. First we write $\lambda^h = \sum_k L_k \lambda_k$ with $L_k \in \mathcal{L}^h$ and expansion coefficients $[\lambda_k]$. Then the problem can be cast as: Find $\mathbf{\Phi}$, such that

$$\mathbf{K}(\mathbf{U})\mathbf{\Phi} = \mathbf{Q}(\mathbf{U}) \,, \tag{4.13}$$

where $\mathbf{K}$ is the assembly of the electro-static stiffness, $\mathbf{\Phi}$ is the electrical solution vector, and $\mathbf{Q}$ the equivalent flux vector, which depends on the method of choice as well as the loading case: For X-FEM with a prescribed potential $\bar{\Phi}$ we have $\mathbf{\Phi} = [\Phi_j, \lambda_k]$ and $\mathbf{K}$, $\mathbf{Q}$ as derived from (4.7) and (4.8). For X-FEM with a conductor and a prescribed total charge Q we have the solution vector $\mathbf{\Phi} = [\Phi_j, \lambda_k, \bar{\Phi}]$ and $\mathbf{K}$, $\mathbf{Q}$ as derived from (4.7) and (3.17). For the IBDG method and a prescribed potential $\bar{\Phi}$ we have $\mathbf{\Phi} = [\Phi_j]$ and $\mathbf{K}$, $\mathbf{Q}$ as derived from (4.7) and (4.10). When we know the total charge on a conductor, this results in $\mathbf{\Phi} = [\Phi_j, \bar{\Phi}]$ and $\mathbf{K}$, $\mathbf{Q}$ in accordance with (4.11) and (4.12).

4.3 Maxwell Boundary Traction

The mechanical boundary traction $\mathbf{F}_M^+$, which arises due to the external electrical field, is given by

$$\mathbf{F}_M^+ \leftarrow \int_{\Gamma_t} \delta \mathbf{u}^h \cdot \mathbf{T}_M^+ \mathbf{n} \, \mathrm{da} \,, \tag{4.14}$$

where we approximate

$$\mathbf{T}_M^+ \mathbf{n} \approx \epsilon_0 \left[\left(\nabla \Phi^h \cdot \mathbf{n} \right) \nabla \Phi^h - \frac{1}{2} ||\nabla \Phi^h||^2 \mathbf{n} \right] \tag{4.15}$$

along the boundary Γ_t. This function is non-linear in the gradient of Φ^h and moreover it has to be evaluated at the embedded boundary location, which randomly may intersect the

Eulerian grid. In standard low-order X-FEM or IBDG methods, it has been shown that the gradient accuracy on the boundary can be bad and largely oscillating. These inaccuracies will cause issues to the global convergence. One method to overcome this issue is by a post-processing technique, that essentially smoothes the gradients (see e.g. [61]). However, this will add computational cost and difficulties may arise when two interfaces come close, contact, or singularities are involved. In contrast, the high-order IBDG method will enable a much more accurate representation of the gradient for smooth and non-smooth boundaries, where for example a re-entrant corner requires the incorporation of singular gradients. Note that alternatively, whenever the boundary is smooth and no singularities are present, one may use a low-order X-FEM method with Lagrange multipliers and interpret the Lagrange multiplier as normal flux on the boundary

$$\lambda^h = -\epsilon_{\mathcal{V}}(\nabla\Phi^h_{\mathcal{V}} \cdot \mathbf{n}_{\mathcal{V}})\,. \tag{4.16}$$

We split the gradient along the boundary into a normal and tangential part

$$\nabla\Phi^h = (\nabla_n\Phi^h)\mathbf{n} + (\nabla_t\Phi^h)\mathbf{t}\,, \tag{4.17}$$

with normal component $\nabla_n\Phi^h = \nabla\Phi^h \cdot \mathbf{n}$ and tangential component $\nabla_t\Phi^h = \nabla\Phi^h \cdot \mathbf{t}$. Then, when $\epsilon_{\mathcal{V}} = \epsilon_0$, we approximate

$$\mathbf{T}^+_M\mathbf{n} \approx \frac{1}{2\epsilon_0}(\lambda^h)^2\mathbf{n} - \lambda^h(\nabla_t\Phi^h)\mathbf{t} - \frac{1}{2}\epsilon_0(\nabla_t\Phi^h)^2\mathbf{n}\,. \tag{4.18}$$

This approach requires careful consideration, since no singularities must be present, as well as the Lagrange multiplier space must be chosen to satisfy the inf-sup condition as discussed in Chapter 3.

4.4 Mechanical Contact

In this study we only consider frictionless contact, and a node-to-rigid-surface contact driver. The mechanical contact force is due to a (nominal) contact pressure $p \geq 0$,

$$\mathbf{F}_{contact} \leftarrow \int_{\Gamma_c} \delta\mathbf{u}^h \cdot p\mathbf{n}\,\mathrm{d}a\,, \tag{4.19}$$

which is active along the contacting surface Γ_c with outward normal $\mathbf{n}$. The pressure p accounts for the unilateral constraint

$$g(\mathbf{U}) \geq 0\,, \tag{4.20}$$

where $g(\mathbf{U})$ is the gap function between the continuum bodies. This problem can be referenced as

$$p \geq 0, \quad g \geq 0, \quad pg = 0\,, \tag{4.21}$$

in accordance with the Kuhn-Tucker conditions (e.g. [94]). During persistent contact, in addition one typically requires

$$p\dot{g} = 0\,, \tag{4.22}$$

the persistency condition. The algorithmic enforcement of (4.21) and (4.22) simultaneously becomes non-trivial while preserving energy and momentum of the deformable bodies involved. For the various computational treatments of this issue we refer to [95, 96, 97, 98, 99, 100], and the more recent studies in [5, 101, 102] or references therein. Here, we consider two algorithms for an explicit, as well as implicit time integration.

4.5 Algorithmic Solution

Let us define

$$\mathbf{R}(\mathbf{U}, \mathbf{\Phi}) = \mathbf{R}_{div,m}(\mathbf{U}) + \mathbf{R}_{div,e}(\mathbf{U}, \mathbf{\Phi}) - \mathbf{F}^{+}_{M}(\mathbf{U}, \mathbf{\Phi}) - \mathbf{F}_{contact}(\mathbf{U})\,. \tag{4.23}$$

We account for any dissipative effects by a linear model and a damping matrix $\mathbf{D}$, such that we can bring (4.3), (4.13) into the form: Given $\mathbf{U}_0$, $\dot{\mathbf{U}}_0$, find $(\mathbf{U}, \mathbf{\Phi})$ such that

$$\mathbf{M}\ddot{\mathbf{U}} + \mathbf{D}\dot{\mathbf{U}} + \mathbf{R}(\mathbf{U}, \mathbf{\Phi}) = \mathbf{0}\,, \tag{4.24}$$

$$\mathbf{K}(\mathbf{U})\mathbf{\Phi} = \mathbf{Q}(\mathbf{U})\,, \tag{4.25}$$

for all time instants $t > t_0$. This states the coupled non-linear semi-discrete system. We will look at the quasi-static solution, as well as the dynamical case, where we test an implicit method (mid-point rule), as well as an explicit method (centered-difference scheme) in order to integrate equations (4.24) and (4.25) in time.

Quasi-static Case

For the quasi-static case, the problem reduces to: Find $(\mathbf{U}, \mathbf{\Phi})$ such that

$$\mathbf{R}(\mathbf{U}, \mathbf{\Phi}) = \mathbf{0}\,, \tag{4.26}$$

$$\mathbf{K}(\mathbf{U})\mathbf{\Phi} = \mathbf{Q}(\mathbf{U})\,. \tag{4.27}$$

One can either solve each equation separately and advance the solution in a staggered scheme, or one calculates the full tangent and solves the coupled system via a monolithic scheme. Even though the latter may be necessary to obtain improved convergence for strongly coupled problems, in this work we follow the staggered scheme for ease of implementation. Employing a staggered solution via a standard Newton-Raphson scheme, the quasi-static coupled non-linear system can be solved as outlined in Alg. 4.1. Note that in this form, the electrical field is solved in every iteration step (Alg. 4.1.2) with a fixed boundary position, and subsequently the electrical force drives the mechanical motion until convergence is achieved.

Staggered Scheme, Quasi-static

LOOP j

1. Given $\mathbf{U}_j$, assemble $\mathbf{K}(\mathbf{U}_j)$ and $\mathbf{Q}(\mathbf{U}_j)$ as in (4.27).

2. Calculate $\mathbf{\Phi}_j$ via
   $\mathbf{K}(\mathbf{U}_j)\mathbf{\Phi}_j = \mathbf{Q}(\mathbf{U}_j)\,.$

3. Assemble $\mathbf{R}(\mathbf{U}_j, \mathbf{\Phi}_j)$, $[\partial\mathbf{R}/\partial\mathbf{U}]\,(\mathbf{U}_j, \mathbf{\Phi}_j)$ as in (4.26).

4. Calculate $\Delta\mathbf{U}_j$ by solving the linear system
   $[\partial\mathbf{R}/\partial\mathbf{U}]\,(\mathbf{U}_j, \mathbf{\Phi}_j)\Delta\mathbf{U}_j = -\mathbf{R}(\mathbf{U}_j, \mathbf{\Phi}_j)\,.$

5. Update
   $\mathbf{U}_{j+1} = \mathbf{U}_j + \Delta\mathbf{U}_j\,.$

6. Check convergence:
   IF $||\mathbf{R}\cdot\Delta\mathbf{U}_j||_2 < TOL$
   EXIT
   ELSE
   Set $j \leftarrow j+1$ and GO TO 1.
   ENDIF

END LOOP j

Algorithm 4.1: Staggered scheme for the quasi-static electro-mechanical BVP.

Implicit Case

For the dynamical implicit solution we employ the *mid-point rule*. Let $\mathbf{U}_n \equiv \mathbf{U}(t_n)$, $\dot{\mathbf{U}}_n \equiv \dot{\mathbf{U}}(t_n)$, $\ddot{\mathbf{U}}_n \equiv \ddot{\mathbf{U}}(t_n)$, $\mathbf{\Phi}_n \equiv \mathbf{\Phi}(t_n)$ at $t = t_n$. Then for one step $(t_n, t_{n+1}]$ we require: Given $\mathbf{U}_n$, $\dot{\mathbf{U}}_n$, and Δt_n, find $\mathbf{U}_{n+1}$, $\dot{\mathbf{U}}_{n+1}$ such that

$$\mathbf{M}\ddot{\mathbf{U}}_{n+1/2} + \mathbf{D}\dot{\mathbf{U}}_{n+1/2} + \mathbf{R}(\mathbf{U}_{n+1/2}, \mathbf{\Phi}_{n+1/2}) = \mathbf{0}\,, \tag{4.28}$$

$$\mathbf{K}(\mathbf{U}_{n+1/2})\mathbf{\Phi}_{n+1/2} = \mathbf{Q}(\mathbf{U}_{n+1/2})\,, \tag{4.29}$$

where

$$\mathbf{U}_{n+1/2} = (\mathbf{U}_{n+1} + \mathbf{U}_n)/2\,, \tag{4.30}$$
$$\dot{\mathbf{U}}_{n+1/2} = (\dot{\mathbf{U}}_{n+1} + \dot{\mathbf{U}}_n)/2\,, \tag{4.31}$$
$$\dot{\mathbf{U}}_{n+1/2} = (\mathbf{U}_{n+1} - \mathbf{U}_n)/\Delta t_n\,, \tag{4.32}$$
$$\ddot{\mathbf{U}}_{n+1/2} = (\dot{\mathbf{U}}_{n+1} - \dot{\mathbf{U}}_n)/\Delta t_n\,. \tag{4.33}$$

This method is second-order accurate and unconditionally stable for linear systems. In order to ensure (4.21) and (4.22), we use a penalty method, with the penalty potential

$$U(g) = \begin{cases} \frac{1}{2}\kappa_p g^2\,, & \text{if } g \leq 0\,, \\ 0\,, & \text{otherwise}\,, \end{cases} \tag{4.34}$$

featuring the penalty parameter κ_p, such that the contact pressure becomes $p = -U'(g)$ whenever there is some penetration. Following [99], we advocate an energy conserving scheme, where the contact pressure $p_{n+1/2}$ at $t = t_{n+1/2}$ is calculated by

$$p_{n+1/2} = \begin{cases} -\frac{U(g_{n+1})-U(g_n)}{g_{n+1}-g_n}\,, & \text{if } g_{n+1} \neq g_n\,, \\ -U'\left(\frac{1}{2}(g_n + g_{n+1})\right)\,, & \text{otherwise}\,. \end{cases} \tag{4.35}$$

As shown in [99], the form of contact pressure as in (4.35) preserves the energy upon contact release. The method does feature a penalty parameter κ_p, which has to be chosen by the user (see App. B for more details of the dynamical contact treatment). As sketched in Alg. 4.2, at each time-step one has to solve the fully coupled nonlinear problem by an iterative method. To this end, we use a staggered scheme as in Alg. 4.1 for the quasi-static case, and a mass lumping procedure following [103, p.704]. In this setting, for each time-step and each iteration of the Newton-Raphson method, one first calculates the electrical field for a fixed mechanical configuration as in Alg. 4.2.3. Subsequently the resulting electrical forces are updated in this configuration (Alg. 4.2.4), that drive the mechanical displacement.

Explicit Case

For the dynamical (explicit) solution we investigate the *centered-difference scheme* (e.g. [104, p.490]): Given $\mathbf{U}_n$, $\dot{\mathbf{U}}_n$, $\ddot{\mathbf{U}}_n$ and Δt_n, for one step $(t_n, t_{n+1}]$ we require:

$$\mathbf{M}\ddot{\mathbf{U}}_{n+1} + \mathbf{D}\dot{\mathbf{U}}_{n+1} + \mathbf{R}(\mathbf{U}_{n+1}, \mathbf{\Phi}_{n+1}) = \mathbf{0}\,, \tag{4.36}$$
$$\mathbf{K}(\mathbf{U}_{n+1})\mathbf{\Phi}_{n+1} = \mathbf{Q}(\mathbf{U}_{n+1})\,, \tag{4.37}$$

and

$$\mathbf{U}_{n+1} = \mathbf{U}_n + \Delta t_n \dot{\mathbf{U}}_n + (\Delta t_n^2/2)\left[(1-2\beta)\ddot{\mathbf{U}}_n + 2\beta\ddot{\mathbf{U}}_{n+1}\right]\,, \tag{4.38}$$
$$\dot{\mathbf{U}}_{n+1} = \dot{\mathbf{U}}_n + \Delta t_n \left[(1-\gamma)\ddot{\mathbf{U}}_n + \gamma\ddot{\mathbf{U}}_{n+1}\right]\,, \tag{4.39}$$

Transient Solution (implicit)

LOOP n

1. Given $\mathbf{U}_n$, $\dot{\mathbf{U}}_n$, Δt_n. Set $\mathbf{U}^0_{n+1} = \mathbf{U}_n$.

LOOP i

2. Calculate $\mathbf{U}_{n+1/2} = (\mathbf{U}_n + \mathbf{U}^i_{n+1})/2$.

3. Assemble $\mathbf{K}(\mathbf{U}_{n+1/2})$ and $\mathbf{Q}(\mathbf{U}_{n+1/2})$ as in (4.25), and calculate $\mathbf{\Phi}_{n+1/2}$ via
$\mathbf{K}(\mathbf{U}_{n+1/2})\mathbf{\Phi}_{n+1/2} = \mathbf{Q}(\mathbf{U}_{n+1/2})$.

4. Assemble $\mathbf{M}$, $\mathbf{D}$, $\mathbf{R}(\mathbf{U}_{n+1/2}, \mathbf{\Phi}_{n+1/2})$ as in (4.24), and calculate
$\tilde{\mathbf{R}} = [(2/\Delta t_n^2)\mathbf{M} + (1/\Delta t_n)\mathbf{D}] \left(\mathbf{U}^i_{n+1} - \mathbf{U}_n\right) - \ldots$
$(2/\Delta t_n)\mathbf{M}\dot{\mathbf{U}}_n + \mathbf{R}(\mathbf{U}_{n+1/2}, \mathbf{\Phi}_{n+1/2})$.

5. Calculate $\Delta\mathbf{U}^i_{n+1}$ by solving
$\left[\partial\tilde{\mathbf{R}}/\partial\mathbf{U}^i_{n+1}\right] \Delta\mathbf{U}^i_{n+1} = -\tilde{\mathbf{R}}$.

6. Update displacement
$\mathbf{U}^{i+1}_{n+1} = \mathbf{U}^i_{n+1} + \Delta\mathbf{U}^i_{n+1}$.

7. Check convergence:
IF $||\tilde{\mathbf{R}} \cdot \Delta\mathbf{U}^i_{n+1}||_2 < TOL$
Set $\mathbf{U}_{n+1} = \mathbf{U}^{i+1}_{n+1}$ and GO TO 8.
ELSE
Set $i \leftarrow i + 1$ and GO TO 2.
ENDIF

END LOOP i

8. Update velocity
$\dot{\mathbf{U}}_{n+1} = (2/\Delta t_n)\left[\mathbf{U}_{n+1} - \mathbf{U}_n\right] - \dot{\mathbf{U}}_n$.

9. Set $n \leftarrow n + 1$ and GO TO 1.

END LOOP n

Algorithm 4.2: Staggered scheme for the dynamic (implicit) electro-mechanical impact simulation.

Transient Solution (explicit)

LOOP n

1. Given $\mathbf{U}_n$, $\dot{\mathbf{U}}_n$, $\ddot{\mathbf{U}}_n$, Δt_n. Calculate predictor
   $\mathbf{U}_{n+1}^{-} = \mathbf{U}_n + \Delta t_n \dot{\mathbf{U}}_n + (\Delta t_n^2/2)\, \ddot{\mathbf{U}}_n$.

2. Check for penetration and update $\mathbf{U}_{n+1}^{-} \to \mathbf{U}_{n+1}$ by closest-point projection, such that the gap $g_A = 0$ for all contacting nodes (B.1).

3. Assemble $\mathbf{K}(\mathbf{U}_{n+1})$ and $\mathbf{Q}(\mathbf{U}_{n+1})$ as in (4.25).

4. Calculate $\mathbf{\Phi}_{n+1}$ via
   $\mathbf{K}(\mathbf{U}_{n+1})\mathbf{\Phi}_{n+1} = \mathbf{Q}(\mathbf{U}_{n+1})$.

5. Assemble $\mathbf{M}$, $\mathbf{D}$, $\mathbf{R}(\mathbf{U}_{n+1}, \mathbf{\Phi}_{n+1})$ as in (4.24).

6. Calculate $\ddot{\mathbf{U}}_{n+1}$ by solving
   $$[\mathbf{M} + \gamma \Delta t_n \mathbf{D}]\, \ddot{\mathbf{U}}_{n+1} = -\mathbf{R}(\mathbf{U}_{n+1}, \mathbf{\Phi}_{n+1}) - \mathbf{D}\left[\dot{\mathbf{U}}_n + (1-\gamma)\Delta t_n \ddot{\mathbf{U}}_n\right] .$$

7. Calculate predictor
   $$\dot{\mathbf{U}}_{n+1}^{-} = \dot{\mathbf{U}}_n + \Delta t_n \left[(1-\gamma)\ddot{\mathbf{U}}_n + \gamma \ddot{\mathbf{U}}_{n+1}\right] .$$

8. Update $\dot{\mathbf{U}}_{n+1}^{-} \to \dot{\mathbf{U}}_{n+1}$, such that the gap rate $\dot{g}_A = 0$ for all contacting nodes (B.3).

9. Set $n \leftarrow n+1$ and GO TO 1.

END LOOP n

Algorithm 4.3: Predictor-corrector scheme for the dynamic (explicit) electro-mechanical impact simulation.

where $\beta = 0$, $\gamma = 0.5$. This scheme is second-order accurate and conditionally stable. One requires a sufficient small time-step, such that the Courant condition is satisfied. Following [105], one typically chooses

$$\Delta t_n = \delta \frac{h}{v_p}\,, \tag{4.40}$$

with the element size h of the smallest element, and the p-wave speed v_p can be estimated for a linear elastic material by $v_p = \sqrt{2\mu/\rho + \lambda/\rho}$, where λ and μ are the first and second Lamé-parameters. The empirical factor δ typically ranges $0.2 < \delta < 0.9$. In order to ensure (4.21) and (4.22) in the explicit setting, we employ a similar approach to a recent method by [5], where the equations of motion are integrated in time with a predictor-corrector-type algorithm (see Alg. 4.3 and App. B). Since the scheme is explicit, we can solve the electrical and mechanical problem independently and only encounter linear equations. Thus the explicit method is computationally more efficient in comparison to the implicit method when the time-steps are comparable. Note however, that the stability requirement (4.40) must be satisfied, which imposes a restriction on the method and may require much smaller time-steps as compared to the implicit method.

We will now assess the performance of the described method by four benchmark examples: The Maxwell-traction in the presence of a corner, the quasi-static pull-in of an electro-mechanically actuated switch, the vibration of a carbon nanotube, and the cyclic impact simulation of an electro-mechanically actuated resonant-switch.

4.6 Electro-static Force Vector in the Presence of a Singularity

In order to evaluate the accuracy of the electro-static force vector, we employ the reentrant corner example from Section 3.5, where a singularity in the gradient of the electrical potential occurs. Here, we monitor the equivalent boundary force vector. The equivalent force vector of interest $\mathbf{F}_M^+ = [\mathbf{f}_{M,i}]$ as stated in (4.14) is assembled from

$$\mathbf{f}_{M,i} = \int_{\Gamma_t} \delta\mathbf{u}_i^h \cdot \mathbf{T}_M^+ \mathbf{n}\,\mathrm{da}\,, \tag{4.41}$$

at each node labeled *'i'*. We refer to $\mathbf{f}_{M,i}$ as the nodal force resulting from the analytical solution $\mathbf{T}_M^+$, whereas $\mathbf{f}_{M,i}^h$ refers to the numerical approximation of the Maxwell traction as assembled from (4.15) or (4.18). We introduce the L2-error norm

$$\varepsilon(\mathbf{F}_M^+) = \sqrt{\sum_i ||\mathbf{f}_{M,i}^h - \mathbf{f}_{M,i}||^2} \Big/ \sqrt{\sum_i ||\mathbf{f}_{M,i}||^2} \tag{4.42}$$

to measure the relative nodal force error. As described in Section 3.5, the potential at the boundary Γ is held at $\Phi_0 = 300$ and is set to zero at the border of the box. We denote the

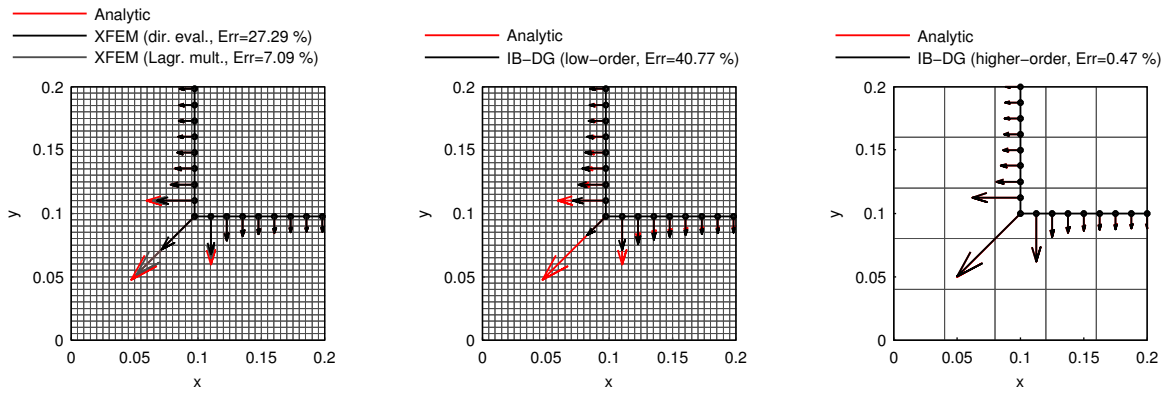

(a) XFEM (h=1/200).

(b) IB-DG (low-order, h=1/200).

(c) IB-DG (high-order, N=5, h=1/25).

Figure 4.2: Corner example: resulting finite element force vector, Γ-boundary, and background mesh.

gap between Γ and the outer box as g. With the origin of a Cartesian coordinate system (x, y) at the lower left corner of the outer box, one can find the analytical solution near this corner by a conformal mapping $f : \tilde{z} \to z$, with $z, \tilde{z} \in \mathbb{C}$. Here $z = x + iy$ represents the coordinate location in the physical space, whereas $\tilde{z} = \tilde{r}\cos(\tilde{\varphi}) + i\tilde{r}\sin(\tilde{\varphi})$ follows rays of corresponding potentials $\Phi = \Phi_0\tilde{\varphi}/\pi$ for any fixed angle $\tilde{\varphi} \in [0, \pi]$. The mapping f is given by

$$f(\tilde{z}) = \frac{2g}{\pi}\left[\arctan\sqrt{\frac{\tilde{z}-1}{\tilde{z}+1}} + \frac{1}{2}\ln\frac{1+\sqrt{\frac{\tilde{z}-1}{\tilde{z}+1}}}{1-\sqrt{\frac{\tilde{z}-1}{\tilde{z}+1}}}\right], \tag{4.43}$$

and we find the solution at $z = (x, y)$ formally by taking the inverse $\tilde{z} = f^{-1}(z)$. The normal gradient then is

$$\nabla_n\Phi = \frac{\Phi_0}{g}\sqrt{\frac{\tilde{z}-1}{\tilde{z}+1}}, \tag{4.44}$$

from which we evaluate the Maxwell traction $\mathbf{T}_M^+\mathbf{n}$ along the boundary Γ.

Note that in order to evaluate expression (4.41), one has to integrate a singular function around the corner due to the singularity in the normal gradient at the corner [see Eq. (3.22)]. For simplicity of notation, let us assume such a function of the form

$$\int_0^{r_0} r^{\pi/\beta-1} g(r)\, \mathrm{d}r\,, \tag{4.45}$$

where the singularity for $\beta > \pi$ is at $r = 0$, and $g(r)$ is a smooth function. In order to obtain accurate results during the Gauss-Legendre integration, we are using a change in variables

$\tilde{r} = r^{\pi/\beta}$, such that (4.45) becomes

$$\int_0^{r_0} r^{\pi/\beta-1} g(r)\, \mathrm{d}r = \frac{\beta}{\pi} \int_0^{r_0^{\pi/\beta}} g(r(\tilde{r}))\, \mathrm{d}\tilde{r}\,, \tag{4.46}$$

which we can now evaluate by a standard Gauss-Legendre quadrature rule.

For the numerical example we consider $\epsilon_{\mathcal{R}} = \epsilon_{\mathcal{V}} = 1$, $\Phi_0 = 300$, and vary g to test several interface locations. The background mesh covers the domain $[0,1]^2$, and has been refined from 25×25 to 200×200 elements; i.e. the element size $h = 1/25, \ldots, 1/200$. For X-FEM via Lagrange multipliers, the corner surface discretization (Γ^h) is not arbitrary and has been optimized to 8 to 64 linear elements per side ($l/h \approx 2.5$). For the low-order DG we choose $\alpha = 20$, whereas for the higher-order DG we choose $\alpha = 1000$. In Fig. 4.2(a,b) we plot a typical result for the low-order methods. Even at the lowest refinement ($h = 1/200$), the use of X-FEM with a direct gradient evaluation according to (4.15) results in $\varepsilon(\mathbf{F}_M^+) > 20\%$, and for the low-order IB-DG we obtain $\varepsilon(\mathbf{F}_M^+) > 40\%$. Using the alternative form (4.18) for X-FEM and piece-wise linear Lagrange multipliers, the error is improved to $\varepsilon(\mathbf{F}_M^+) < 10\%$. This result though is a best case scenario, as we optimized the space $\mathcal{L}^h$. A coarse background mesh, or changing interface locations result in a force-vector variation that can lead to incomplete convergence during the non-linear coupled electro-mechanical solution as observed in the following example. By employing the high-order IB-DG, a much higher accuracy in the nodal force along the Γ-boundary in Fig. 4.2(c) is observed, where the force error even at the coarse refinement ($h = 1/25$) is $\varepsilon(\mathbf{F}_M^+) < 1\%$. Note the additional benefit that with IB-DG there is no restriction on the Γ^h-discretization. In particular, a $\mathcal{L}^h$ discretization as pictured in Fig. 4.2(c) using piece-wise linear Lagrange multipliers and a bi-linear potential interpolation would fail, since the inf-sup condition would be violated.

4.7 Electro-static Pull-in

Next we address the coupled solution of an electro-mechanical pull-in example as sketched in Fig. 4.3. We assume a non-linear Neo-Hookean material, which is surrounded by an ideal, infinitely thin conductor with the same material properties. Since no field can penetrate the material, the stored energy for the material as given by (2.40) reduces to

$$\psi(\mathbf{C}) = \frac{\mu}{2}\,(I_1 - 3) - \mu \ln J + \frac{\Lambda}{2}\,(\ln J)^2\,, \tag{4.47}$$

where $I_1 = \operatorname{tr}\mathbf{C}$, $J = \det\mathbf{F}$, and the Lamé parameters $\Lambda = E\nu/[(1+\nu)(1-2\nu)]$, $\mu = E/[2(1+\nu)]$ in terms of the Young's modulus E and Poisson ratio ν. The Cauchy stress then reads

$$\mathbf{T} = \rho_0 J^{-1}(\Lambda \ln J - \mu)\mathbf{I} + \rho_0 \mu J^{-1}\mathbf{B}\,, \tag{4.48}$$

with mass density ρ_0 and $\mathbf{B} = \mathbf{F}\mathbf{F}^T$ as derived in Section 2.3. The material is clamped on top, and an increasing voltage on the conductor will pull the material down towards the grounded electrode which is surrounded by a rigid dielectric.

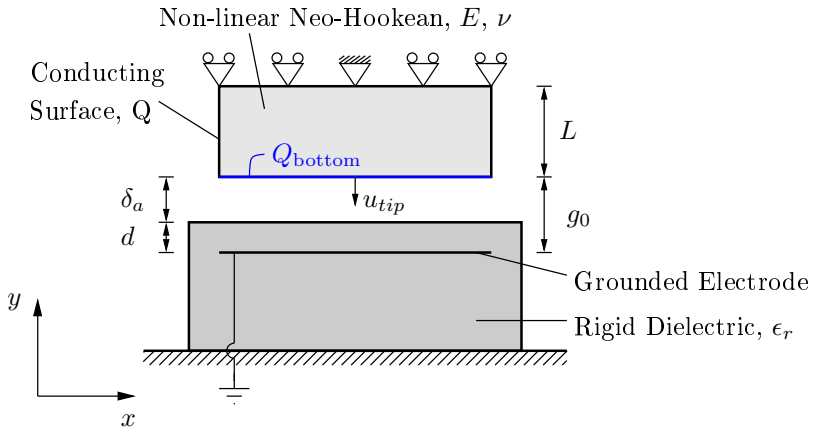

Figure 4.3: Pull-in example: schematic.

By considering a plane strain two-dimensional problem, one can derive an approximate solution

$$\mu\left(\lambda_y - \lambda_y^{-3}\right) = \frac{\sigma_f^2}{2\epsilon_0}\,, \tag{4.49}$$

where λ_y is the stretch in the y-direction and σ_f is a uniform charge density applied at the bottom edge. The material is assumed to be incompressible, no fringing fields are added, and the side-edge forces are neglected. We calculate the tip displacement as

$$u_{tip} = (\lambda_y - 1)L\,, \tag{4.50}$$

and for each surface charge density the corresponding voltage on the conductor

$$\bar{\Phi} = \frac{d + \epsilon_r \delta_a}{\epsilon_0 \epsilon_r}\sigma_f\,, \tag{4.51}$$

with $\delta_a = (g_0 - d - u_{tip})$ being the air-gap between dielectric and conductor, d the dielectric thickness above the electrode, and g_0 the initial distance between electrode and conducting bottom edge at zero load (see Fig. 4.3).

As becomes clear from the analytical approximation, it is advantageous to consider the charge loading case, since a unique solution for the tip displacement can be found at each load σ_f in (4.49), (4.50), and subsequently one solves for the voltage via (4.51). A direct solution for a given $\bar{\Phi}$ features a non-unique tip displacement, which is a well-known effect as discussed for example in [106, p. 134]: once the voltage reaches a critical value there is an unstable equilibrium point, beyond which any device is *pulled-in* towards the electrode. In our example, one can estimate this point at

$$u_{tip}^{PI} = \frac{1}{3\epsilon_r}\left[d + \epsilon_r(g_0 - d)\right]\,, \tag{4.52}$$

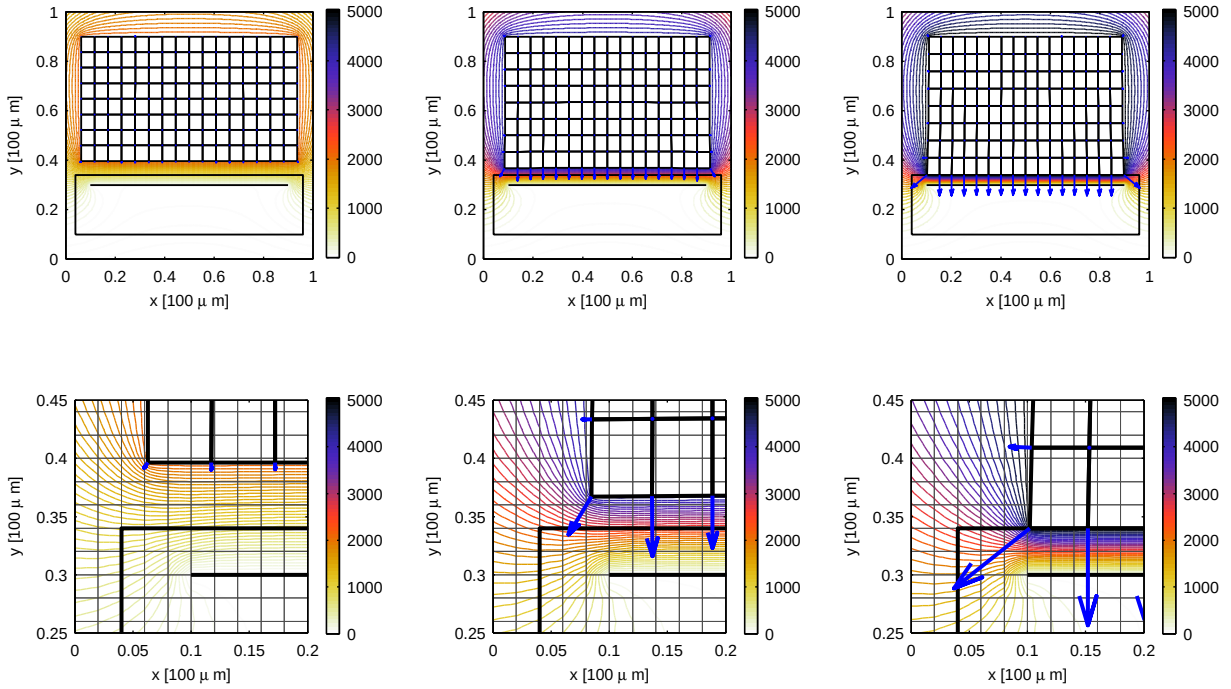

Figure 4.4: Pull-in example: (top) mechanical mesh, electro-static force vector and electrical potential contour; (bottom) detailed mechanical (bold) mesh and electrical (fine) mesh with electro-static force vector and electrical potential contour at various load-steps.

Q [C]:	3.0	5.0	6.5	7.5	8.0	8.5	8.9	11.0	13.0
Q_{bottom} [C]:	1.93	3.29	4.40	5.24	5.77	6.38	6.92	8.61	10.17
$\bar{\Phi}$ [kV]:	2.11	3.37	4.07	4.27	4.14	3.73	3.46	4.28	5.05

Table 4.1: Pull-in example: charge load parameters and floating potential $\bar{\Phi}$.

which reduces to

$$u_{tip}^{PI} = \frac{1}{3} g_0 \,, \tag{4.53}$$

if $\epsilon_r = 1$, which is consistent to what is found in [106, p. 135].

For the numerical example we assume a rubber-like material ($E = 20$ MPa, $\nu = 0.45$) with length $L = 50$ μm and width 80 μm. Moreover we assume $g_0 = 10$ μm, $d = 4$ μm, and $\epsilon_r = 1$. The finite element model uses 128 quadrilateral elements for the mechanical body $\mathcal{R}$ featuring a bi-linear interpolation, and 50×50 quadrilateral elements for the electrical potential field interpolation in combination with the high-order IB-DG method. We increase the total charge on the conducting surface until the material is stretched down to contact with the dielectric substrate. The corresponding charge accumulation on the bottom-edge

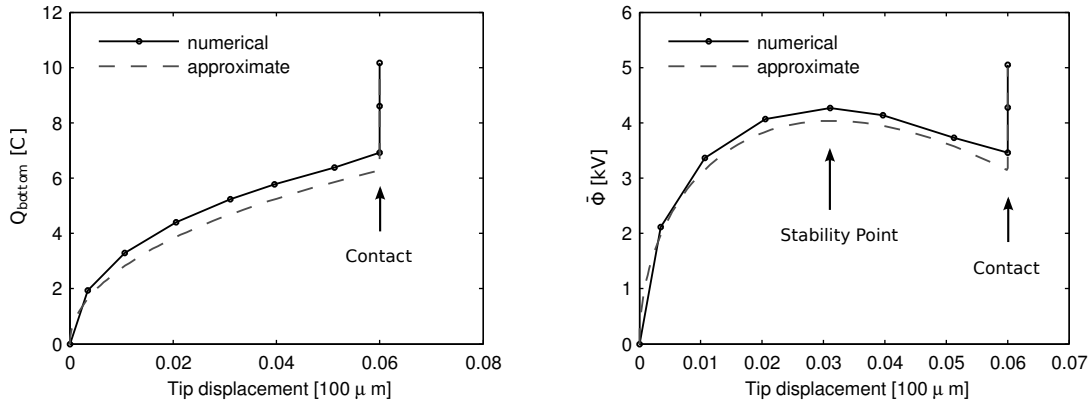

Figure 4.5: Pull-in example: (left) tip displacement versus charge Q_{bottom}; (right) tip displacement at corresponding voltages.

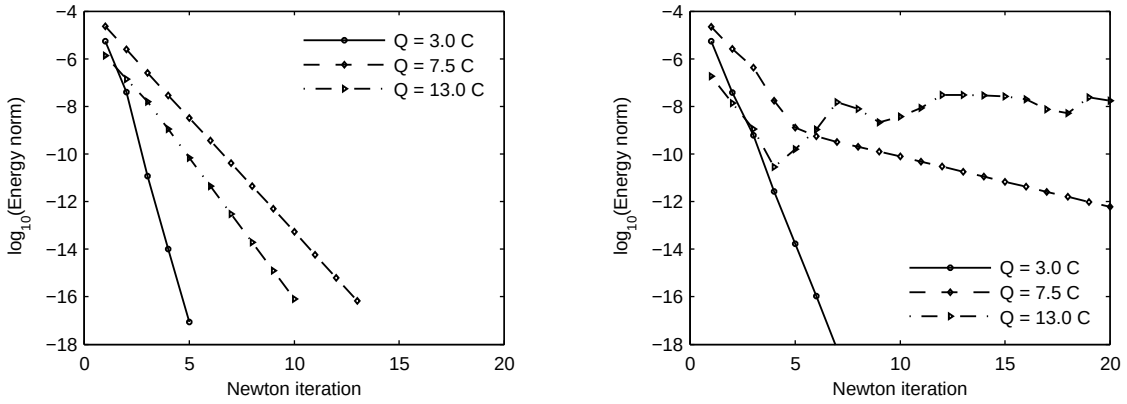

Figure 4.6: Pull-in example: (left) typical convergence curves of global Newton algorithm when using the high-order IB-DG at small load ($Q = 3$ C), close to stability point ($Q = 7.5$ C) and during contact ($Q = 13$ C); (right) convergence issues of low-order immersed boundary method.

Q_{bottom} (see Fig. 4.3), as well as the floating potential $\bar{\Phi}$ are summarized in Table 4.1. [1] As a penalty parameter we use $\kappa_p = 10^3$, which we found to be sufficient to insure less than 10 nm penetration. Our solution follows Alg. 4.1 for the quasi-static case. In this example no electrical field will be inside the upper block, and thus only the force due to the outer field as arising from the Maxwell-traction must be considered. We compute this force by the high-order immersed boundary method as illustrated in the previous example.

By looking at typical results in Fig. 4.4, we observe how the high-order IB-DG nicely interpolates the potential around the corner, and handles the boundary motion well across several elements until contact. This is a major advantage of the immersed boundary method: since no elements distort or collapse, one can handle large boundary motions and topological changes without any remeshing. Note that this simulation will fail with most classical electro-mechanical solution techniques such as ALE methods, since the closing of the air gap will result in highly distorted elements, or collapsing elements respectively.

In Fig. 4.6(left) we plot typical convergence plots for various loading cases at small load, close to the stability point and during contact. At low loads, convergence by twelve orders of magnitude during four to five Newton steps is achieved. At higher loads, we observe slower (linear) convergence, which is due to the stronger electro-mechanical coupling. [2]

The use of a higher-order immersed boundary method as opposed to low-order methods becomes essential in this problem, since only the accurate resolution of the singular gradient at the corner will deliver any physically meaningful results. Moreover, inaccuracies in the gradient calculation and the resulting oscillation of the boundary traction as the boundary moves across several elements can result in numerical issues to obtain convergence during the Newton-Raphson solution procedure [Fig. 4.6(right)]. As observed in Fig. 4.6(right), the convergence may be slower or completely fail (e.g. $Q = 13$ C).

4.8 Nanotube Vibration

Our next example deals with a carbon nanotube that is excited by an external electrical field. Carbon nanotubes possess very unique and promising characteristics for use as NEMS resonators [13, 14, 15, 4, 16]. In this study we suppose that the carbon nanotube is a conductor. After certain corrections when extracting material properties, the use of continuum mechanics is still justified for such systems [17], and various mechanical models exist [107, 108]. We focus here on the efficient computational treatment of a cyclic motion. In particular, we will look at the excitation of the first three eigen-modes of a nanotube as sketched in

[1] By applying a charge load one can easily simulate the full pull-in up to and including the contacting stage. See Section 3.3, 3.4 and 4.2 for the treatment of the electro-static BVP in the case of charge loading. In this case, one obtains the floating potential $\bar{\Phi}$ as solution unknown, which is plotted Fig. 4.5(right). If in contrast one wishes to solve the solution for a given potential load directly, continuation methods such as the arc-length method must be employed in order to pass the limit point.

[2] Note that in Alg. 4.1 we utilize a staggered scheme by an electro-mechanical operator split; a monolithic scheme that accounts for the full tangent of coupling terms in the nonlinear solution iteration will improve the convergence rates whenever strong electro-mechanical coupling occurs.

Fig. 4.7. In this study we consider a nanotube with a sharp corner. While carbon nanotubes may be closed smoothly at the tip, the cut-nanotube imposes a greater challenge on the computational treatment due the arising singularity in the electrical field at the corner (see Section 5.4).

As sketched in Fig. 4.7, we assume that the nanotube is mechanically clamped and electrically grounded. A separate input voltage V_i at an external electrode creates a capacitive force across the gap, such that the nanotube will vibrate in the corresponding resonance mode. The input voltage is given by

$$V_i(t) = V_{\text{DC}} + V_{\text{AC}} \sin \omega_i t \,, \tag{4.54}$$

with the constant part V_{DC}, the alternating amplitude V_{AC}, and frequencies ω_i, $i = 1, 2, 3$. We find ω_i by the eigen-analysis as presented in Section 5.1. For the numerical example we consider the nanotube length of 80 nm and a diameter of 8 nm. The initial gap to the electrode is 46 nm, and we assume a nonlinear Neo-Hookean material as in (2.41) with $E = 1$ TPa, $\nu = 0.31$, $\rho = 1$ g/cm^3. The resulting eigen-frequencies are summarized in Tab. 4.2 in accordance with an ultra-high frequency resonator [18]. We assume a mass-proportional damping $\mathbf{D} = \alpha_M \mathbf{M}$, with $\alpha_M \in \{5 \cdot 10^9 \text{ s}^{-1}, 10 \cdot 10^9 \text{ s}^{-1}\}$. Then, the damping ratios are given by $\xi_i = \alpha_M/(2\omega_i)$ as tabulated in Tab. 4.2 for Modes 1-3.

Note in this study we limit ourselves to a 20×2 finite element grid for the mechanical motion in order to calculate the transient response, which already sets a limit of > 1443 time-steps per cycle according to (4.40) for the fundamental mode in the explicit case. One would need to consider a mesh refinement, and/or the use of enhanced elements or incompatible modes in order to gain more accurate results in such a bending dominated problem. Such methods are well established, and we refer to [109] for a brief historical account and references therein. The implicit method is more efficient in this example for the simulation of the lower modes since it is unconditionally stable, and larger time-steps may be used as long as accuracy is preserved. For the higher modes, the requirement (4.40) imposes less restriction on the stability region, and the explicit method will be more efficient in comparison to the mid-point rule as we observed higher accuracy for similar time-step sizes (see Table 4.2 for the different time-steps per cycle $2\pi/(\omega_i \Delta t_n)$ used in the explicit integration). For the electrical field we use a 25×25 Eulerian finite element grid, in combination with the high-order IB-DG method to accurately evaluate the singularity of the boundary traction around the nanotube corner.

Since in our case we employ mass-proportional damping, the damping ξ_i becomes smaller for a fixed α_M at higher modes. Thus, the number of cycles to overcome the transient phase to a steady state is relatively higher at higher modes. In this work we assume that a steady state is reached when the residual (5.18) will decay by six orders of magnitude after releasing the system from zero initial conditions. The corresponding number of cycles N to overcome the transient phase are tabulated in Tab. 4.2: $N_1 = 40$ cycles for Mode 1, $N_2 = 238$ cycles for Mode 2, and $N_3 = 621$ cycles for Mode 3 at $\alpha_M = 5 \cdot 10^9$ s^{-1}; $N_1 = 20$ cycles for Mode 1, $N_2 = 119$ cycles for Mode 2, and $N_3 = 310$ cycles for Mode 3 at $\alpha_M = 10 \cdot 10^9$ s^{-1}. Please refer to Section 5.4 and 5.6 for a more careful discussion of the steady state notion.

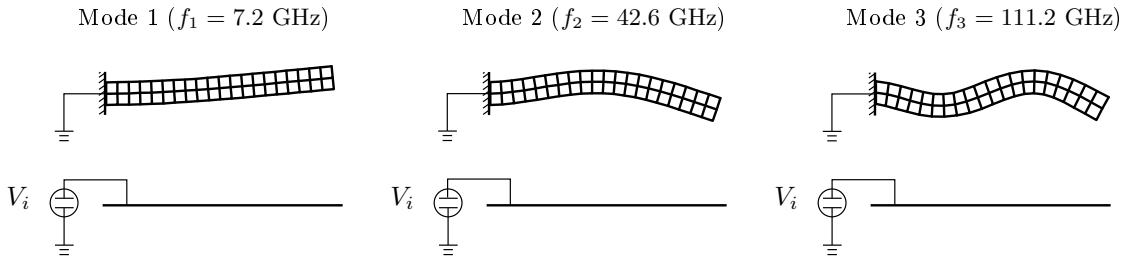

Figure 4.7: Nanotube vibration schematic.

	$\omega_i/2\pi$[GHz]	$2\pi/(\omega_i \Delta t_n)$	$\xi_{i,1}$	N_1	$\xi_{i,2}$	N_2
Mode 1:	7.2	1444	$1.1 \cdot 10^{-1}$	20	$5.6 \cdot 10^{-2}$	40
Mode 2:	42.6	244	$1.9 \cdot 10^{-2}$	119	$9.4 \cdot 10^{-3}$	238
Mode 3:	111.2	96	$7.2 \cdot 10^{-3}$	310	$3.6 \cdot 10^{-3}$	621

Table 4.2: Nanotube vibration example: eigenfrequencies, explicit time-step size and number of cycles N to reach steady state during the transient solution for Mode 1-3 at various damping ratios ξ.

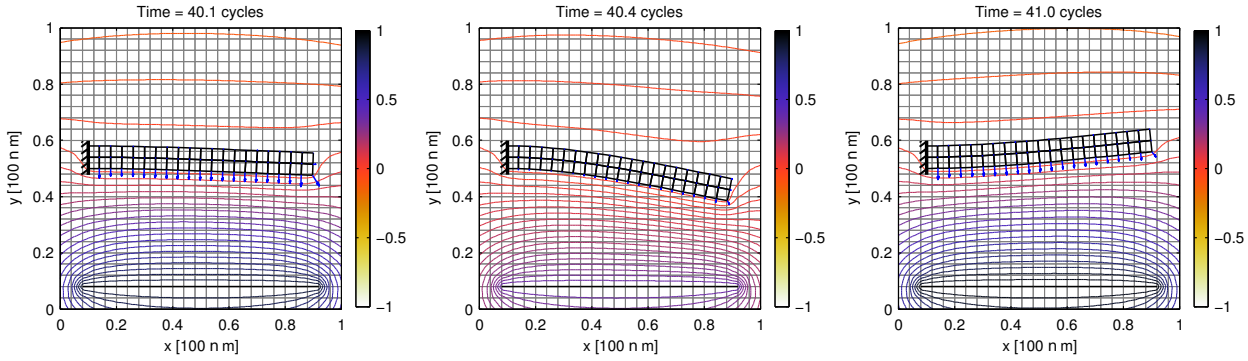

Figure 4.8: Nanotube vibration, Mode 1: deformed mechanical (bold) mesh, electrical (fine) mesh, contour of electrical potential, and Maxwell boundary traction at $V_{\mathrm{DC}} = 60$ V and $V_{\mathrm{AC}} = 40$ V for various time instants.

When we release the system from zero initial conditions, we observe a typical result for the first mode with $\xi_1 = 5.6 \cdot 10^{-2}$, $V_{\mathrm{DC}} = 60$ V and $V_{\mathrm{AC}} = 40$ V after 40 cycles in Fig. 4.8. One can observe the deformed mechanical mesh, the electrical potential field, as well as the Maxwell boundary traction at various time instants.[3] Note that the boundary force around the corner stems from a singular charge distribution. In accordance to what has been observed in Section 4.7, we stress that a higher-order immersed boundary method becomes necessary for any accurate and physically meaningful results. Moreover, the use of such a high-order accurate method is needed in order to obtain convergence of the residual as discussed in Section 5.4.

In Fig. 4.9 we monitor the vertical tip displacement and velocity for the case $\alpha_M = 5 \cdot 10^9$ s^{-1} and the load $V_{\mathrm{DC}} = 60$ V and $V_{\mathrm{AC}} = 40$ V. The results over time and the corresponding phase portraits are plotted for Mode 1-3 when we release the nanotube from zero initial conditions. The displacement of Mode 1 reaches about -0.9 ± 11 nm, and a velocity of ± 68 mm/s at steady state after 40 cycles [Fig. 4.9(top)]. Looking at the higher modes, the amplitude of the displacement at steady state decreases to about -0.9 ± 0.9 nm for Mode 2 after 238 cycles [Fig. 4.9(middle)], and -0.9 ± 0.2 nm for Mode 3 after 621 cycles [Fig. 4.9(bottom)]; the velocity decreases to about ± 33 mm/s for Mode 2, and ± 19 mm/s for Mode 3. Note that the simulation of the higher modes becomes more expensive, as the number of cycles to overcome the transient phase increase due to the lower damping. For even lower damping or finer meshes, the simulation time to overcome the transient phase will impose severe limitations on the design process. Please refer to Chapter 5, where a novel method is discussed in order to solve for cyclic steady states more efficiently.

4.9 Reso-switch

Let us now examine a micro-electro-mechanical disk resonator, which is excited in the wine-glass mode by a forced vibration, such that dynamic contact occurs with a rigid electrode as sketched in Fig. 4.10. Such high-Q on-chip resonators or dynamic switches show high potential for the replacement of transistors, e.g. for power-amplification, due the superior quality factors [9, 10, 11, 12]. The system, as sketched in Fig. 4.10(left,middle), is a model similar to the resonance switch (reso-switch) in the work by [3].

As sketched in Fig. 4.10, we assume that the driving electrodes are operated at a periodic input voltage V_i, and the resulting capacitive force brings the disk into a resonance vibration mode. The voltage at the disk is kept constant at V_D. During this vibration mode, the disk will periodically switch contact with the output electrodes, where a voltage V_o is measured. No contact along the input axis occurs due to a larger air-gap in comparison to the output axis. During off-mode, an electrical charge Q assembles on the electrodes, whereas a current i flows when the disk touches the electrodes, or during electrical breakdown.

[3] Note that such large motions can be easily tracked with the immersed boundary method, and no remeshing or motion of the electrical mesh is required– as becomes necessary when using a Lagrangian or arbitrary Eulerian-Lagrangian (ALE) approach.

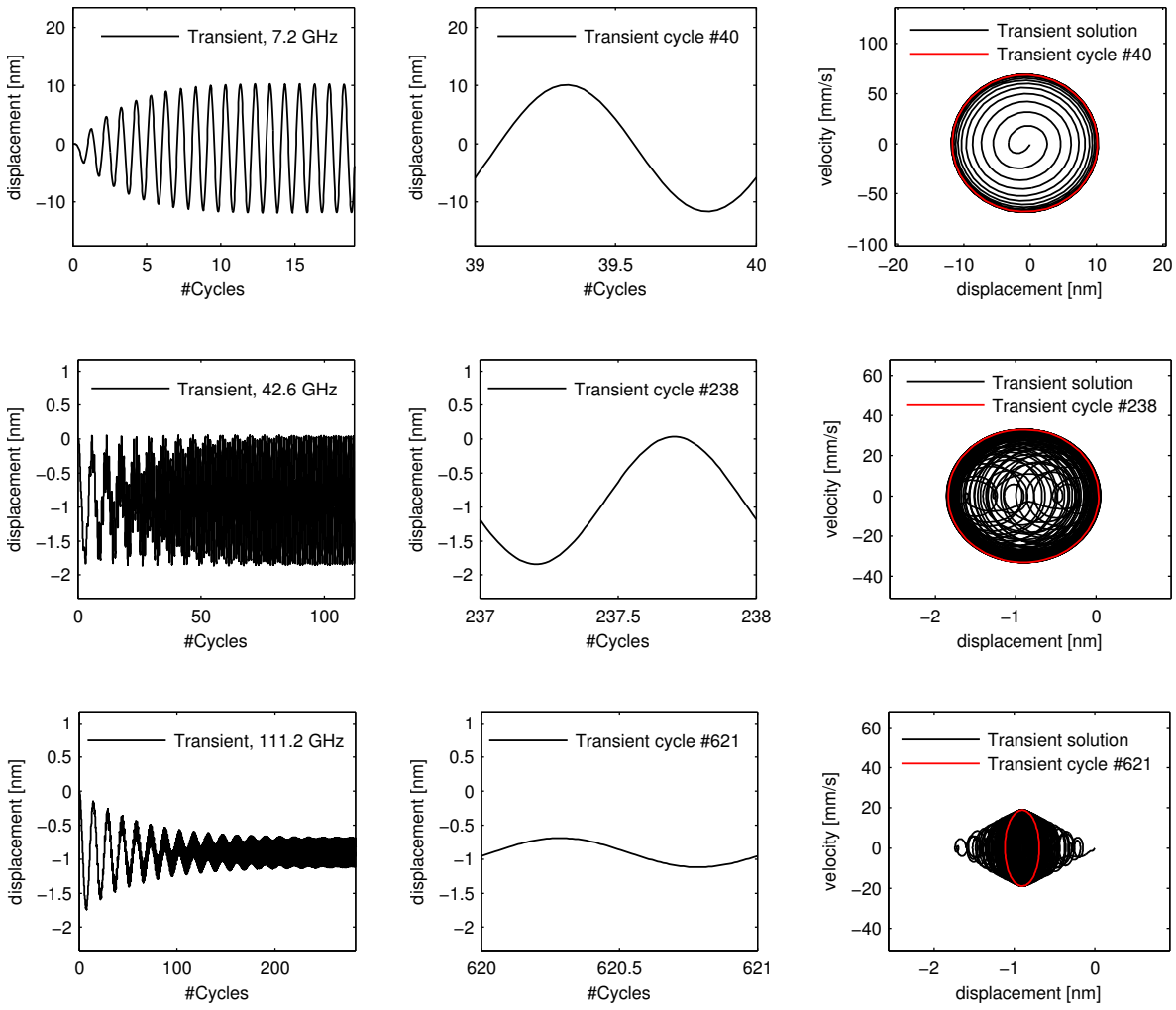

Figure 4.9: Nanotube vibration: transient solution of the normalized tip-displacement and and velocity for (top) Mode 1, (middle) Mode 2, (bottom) Mode 3.

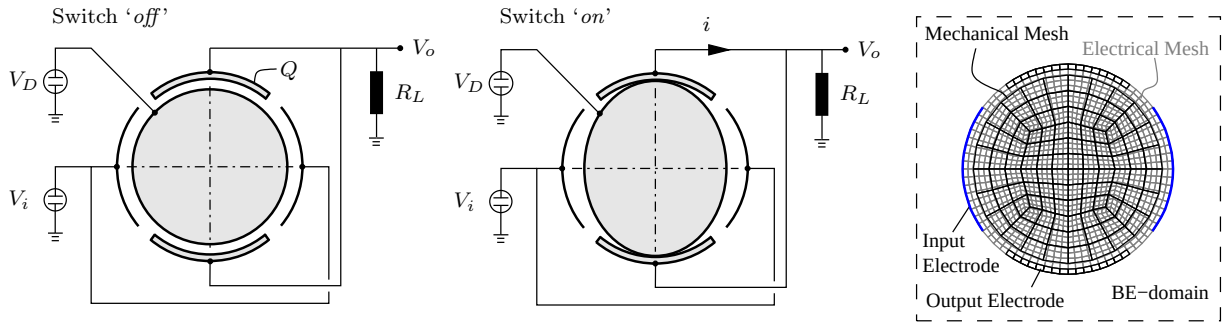

Figure 4.10: Reso-switch example: (left) schematic *off*-mode; (middle) schematic *on*-mode; (right) mechanical (bold) mesh, electrical (fine) mesh, input/output electrodes, and boundary element (BE) domain.

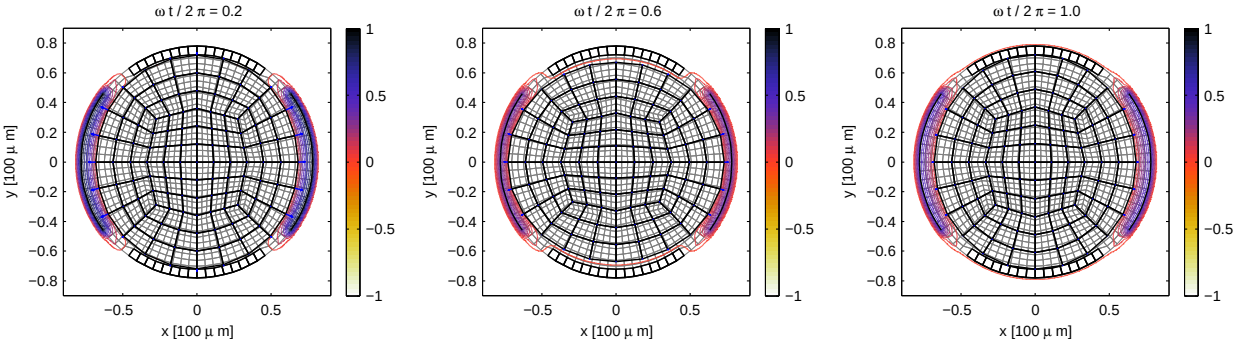

Figure 4.11: Reso-switch results: deformed mechanical (bold) mesh, electrical (fine) mesh, contour of electrical potential, and Maxwell boundary traction for *Load 1* at various time instants during '*off*'- and '*on*'-mode.

In the context of finite elements, we find the eigenmodes numerically by a standard subspace iteration [110, p.156]. We use symmetry boundary conditions as sketched in Fig. 4.10(left,middle) for the mechanical deformation of the disk, 108 quadrilateral elements with a bi-linear interpolation [see Fig. 4.10(right)], and a plane stress nonlinear Neo-Hookean material model as derived from (2.41) with standard material properties of Ni: $E = 179$ GPa, $\nu = 0.31$, $\rho = 8.9$ g/cm^3. For a disk radius $R = 70$ μm and thickness 4 μm, we obtain the fundamental frequency $f_0 = 14.8$ MHz.

For the electrical field computation, we use a background mesh with 1200 quadrilateral elements that cover the domain of interest as sketched in Fig. 4.10(right). The electrode boundaries are aligned with the background mesh, and the boundary motion of the disk is captured by the immersed boundary method. We apply a resonance load at the input

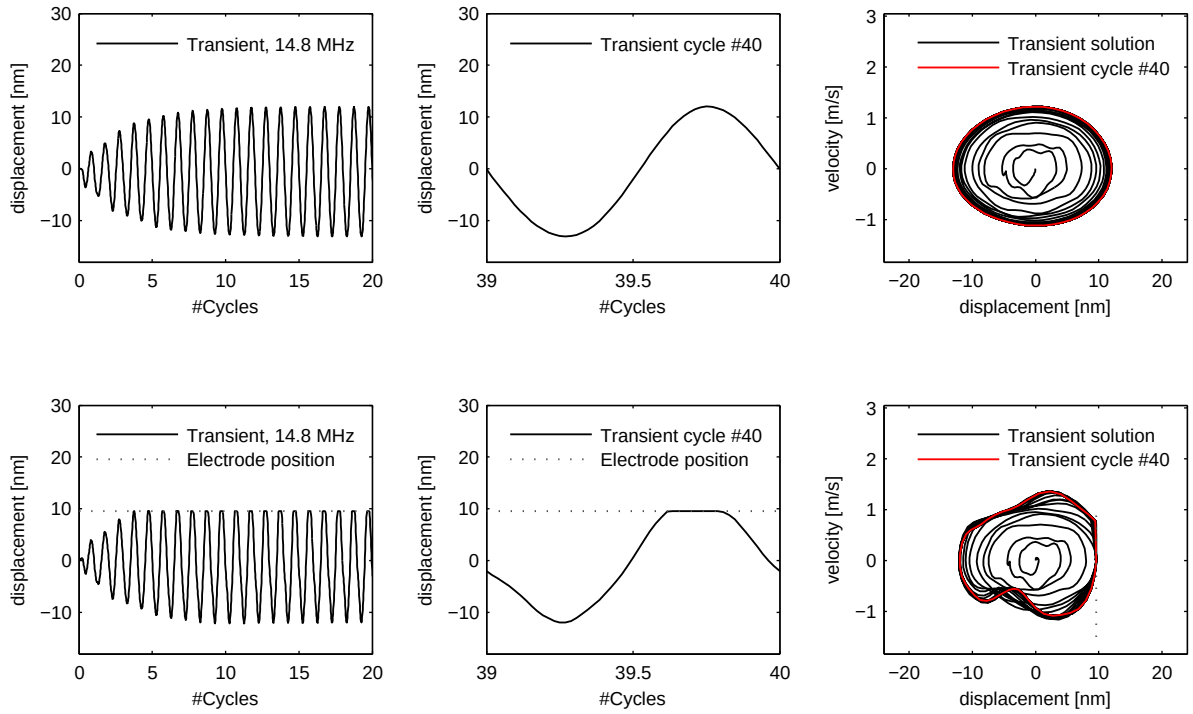

Figure 4.12: Reso-switch example: transient solution of the top-disk-node displacement and velocity for (top) *Load 2*, and (bottom) *Load 3*.

electrodes:

$$V_i(t) = V_{\rm DC} + V_{\rm AC} \sin \omega t \,, \tag{4.55}$$

where $\omega = 2\pi f_0$, the bias-voltage is given by $V_{\rm DC}$, and the load amplitude is $V_{\rm AC}$. At the output electrodes we assume $V_o = V_D$ when the disk is in contact or during electrical breakdown (*on*-mode), and otherwise calculate V_o from the requirement

$$\frac{dQ}{dt} = \frac{V_o}{R_L} \,, \tag{4.56}$$

where the output load $R_L = 220\ \Omega$ and the total charge Q on both output electrodes is calculated from the electrical field (see Section 4.10). The damping is assumed to be mass-proportional with $\mathbf{D} = \alpha_M \mathbf{M}$, such that the damping ratio is $\xi = \alpha_M/(2\omega)$. In the following example we test the case $\xi = 5.6 \cdot 10^{-2}$ and look at three loading cases.

Load 1. We will first excite the disk at a magnified load of $V_{DC} = 90$ kV, $V_{AC} = 60$ kV and $V_D = 6$ kV from zero initial conditions in order demonstrate the performance of the immersed boundary method during steady contact in Fig. 4.11. The initial gap between the output electrodes and the disk in this example is assumed to be $g_0 = 2.2\ \mu$m, and the initial gap between the input electrodes and the disk is assumed to be 6 μm. In Fig. 4.11

we plot typical results of the mechanical displacement, the electrical potential contour and the Maxwell boundary traction at various time instants during '*off*'- and '*on*'-mode.[4]

Load 2. We will now excite the disk at a load $V_{DC} = 6.45$ kV, $V_{AC} = 4.3$ kV and $V_D = 240$ V from zero initial conditions, with the initial gap to the output electrodes being $g_0 = 2.2$ μm, and the initial gap between the input electrodes and the disk being 6 μm. With this load and damping there will be no contact with the output electrodes, as the displacement does not sufficiently ramp up. We monitor the displacement and velocity of the top-end node of the disk in Fig. 4.12(top). One observes that a steady state is reached after about 40 cycles ramp-up, with the displacement of -0.5 ± 12.5 nm, and a velocity of 0.05 ± 1.15 m/s.

Load 3. Finally, we will excite the disk at a load $V_{DC} = 6.45$ kV, $V_{AC} = 4.3$ kV and $V_D = 240$ V from zero initial conditions, with the initial gap to the output electrodes being $g_0 = 9.6$ nm, and the initial gap between the input electrodes and the disk being 6 μm. As the output electrodes are closer to the disk, the disk starts to impact into the output electrodes after about 5 cycles ramp-up [see Fig. 4.12(bottom)]. In Fig. 4.12(bottom) we monitor the displacement and velocity of the top-end node of the disk. After 40 cycles, we observe the displacement and velocity during steady contact, where the displacement oscillates in $[-11.9, 9.6]$ nm, and the velocity in $[-1.1, 1.4]$ m/s. In this example one observes about 15% persistent contact during one loading cycle.

We notice that a stronger impact will result in larger oscillations upon release of the disk, and a highly non-linear phase-portrait. This is in accordance to what has been observed in App. B for the disk-impact example. For the present set of parameters as in *Load 3*, a steady contact state has been observed. However, depending on the damping of the system and the magnitude of the mechanical impact, a chaotic state may be reached. A careful analysis of such steady contact conditions is a logical next step in further advancing the subject at hand, but will be left to a future work.

In this example, we promote the use of the (explicit) centered-difference method with 52 steps per cycle, which satisfies the critical time-step estimate (4.40) and provides sufficient accuracy for the presented example. The use of the implicit method, while unconditionally stable, did not improve upon accuracy at the same time-step size. Note however, that a reduced mesh-size of the mechanical mesh, an increased p-wave speed, or a device operating at a lower resonance frequency, may require a much smaller time-step to satisfy the stability criteria (4.40), and the implicit method may improve upon efficiency in such cases. Please refer to Chapter 5 for a more detailed discussion on the efficient simulation of electro-mechanical devices operating at resonance.

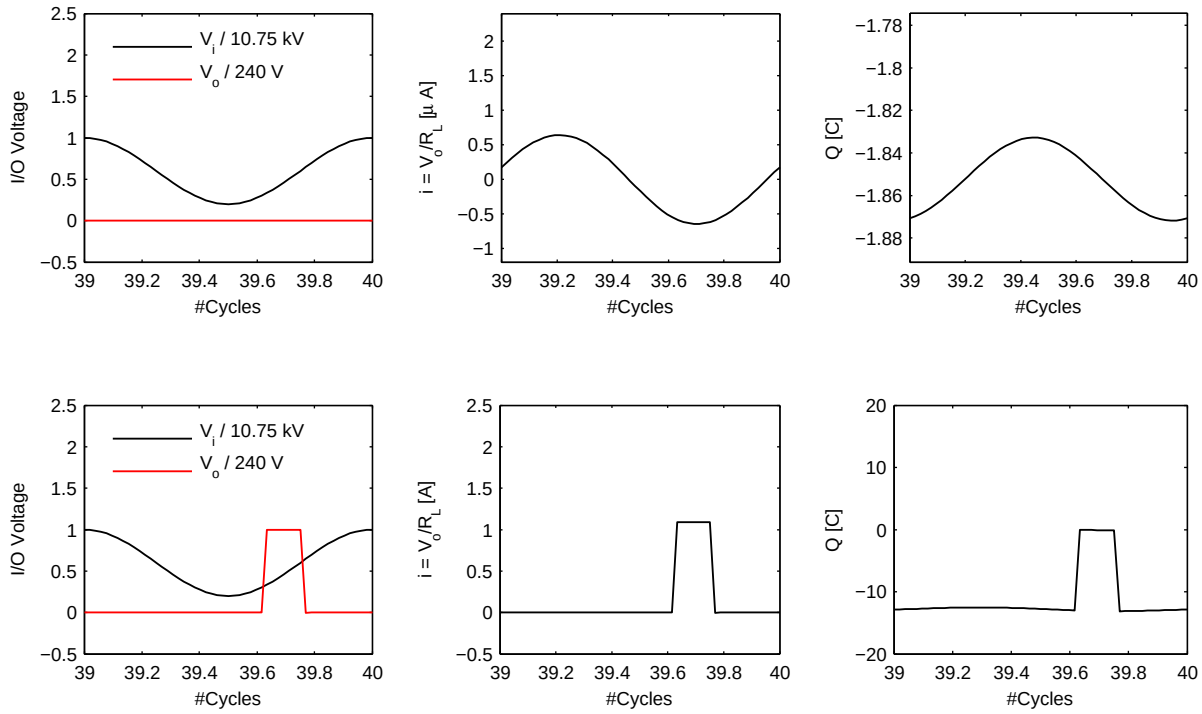

Figure 4.13: Reso-switch example: input voltage V_i, output voltage V_o, electrical current flow i, and charge Q on output electrodes for (top) *Load 2*, and (bottom) *Load 3*.

4.10 Electrical Contact

As mentioned in the previous section, the electrical boundary conditions for the resonant switch during impact need careful consideration. During contact, the voltage $V_o = V_D$, and otherwise we find V_o as a floating potential, where we have to take into account the dynamics of the accumulated charge Q on the output electrodes according to (4.56). In this work we discretize (4.56) by a backward Euler scheme, such that

$$Q_{n+1} = Q_n + \frac{\Delta t_n}{R_L} V_{o,n+1} \,, \tag{4.57}$$

and thus the charge loading problem at the new time-step can be formulated in terms of the known value Q_n, and the unknown $V_{o,n+1}$ which we solve for. The electrical current through the output load R_L is given by $i = \dot{Q} = V_o/R_L$. We observe the input voltage V_i, the output voltage V_o, the electrical current flow i, and the charge Q for loading cases *Load 2* and *3* in Fig. 4.13.

[4] Note that the immersed boundary method can handle the closing of the gap during impact very well, whereas traditional methods in the Lagrangian context will encounter issues, as elements will collapse or an expensive remeshing will be required.

In Fig. 4.13(top), we find that during *Load 2* there is only a very small oscillation in the voltage V_o and current $i = V_o/R_L \in [-0.6, 0.6]$ μA. This is due to the dynamics of the total charge Q on the output electrodes driven by the mechanical motion of the disk, and the electrical field respecting Eq. (4.57). In Fig. 4.13(top,right) we observe $Q \in [-1.87, -1.83]$ C. Note that the charge Q is strictly negative, as a result from the (positive) electrical boundary conditions on the disk and input electrode, and the grounding of the output load.

In Fig. 4.13(bottom) for *Load 3*, there is a jump in the output voltage to $V_o = 240$ V during contact of the disk with the output electrode. Consequently the electrical current jumps to $i = V_o/R_L = 1.1$ A during contact. The electrical charge on the output electrodes drops to a residual value $Q = -0.06$ C, which is determined from the capacitive configuration of the input electrodes. We observe a duty-cycle of $\Delta t_{on}/T = 0.15$ in this example. As the disk releases, the voltage V_o and current i drop back to a small oscillation around zero as in *Load 2*, whereas the charge Q will accumulate to around $Q = 13$ C [Fig. 4.13(bottom,right)].

Note that the accumulated negative charge Q on the output electrode during '*off*'-mode is larger for *Load 3* as compared to *Load 2*. This is due to the closer location of the output electrode to the disk, while the electrical boundary conditions remained unchanged. Moreover note that the time-constant of the charge accumulation on the electrode is much faster in this example in comparison to the disk-vibration period. Thus the dynamics of the charge Q is quasi-instantly correlated to the disk-motion. An increased capacitive configuration, however, may change the output dynamics of the voltage V_o or the current i upon release of the disk, as has been experimentally observed in [12]. The effect of various geometries on the charge accumulation, as well as additional capacitors at the output circuit will be left to future studies.

Typical devices as in [3] are designed with a much lower damping as compared to the present example. We will consider further examples featuring lower damping values in Section 5.5. The computational treatment by a classical time-stepping through the transient phase from zero initial conditions as we discussed here will become very expensive, or even impossible when the damping is very low and the system size increases. In the following chapter we will discuss a numerical method in order to find cyclic steady states more efficiently, with substantial speed-ups especially for low damping values.

Chapter 5

Cyclic Steady States

Many electro-mechanical systems are designed to operate at resonance, where the ramp-up simulation to steady state is computationally very expensive– especially when low damping is present. In this chapter, we present an efficient method to solve for cyclic steady states of electro-mechanical devices excited at resonance. The proposed method relies on a Newton-Krylov shooting scheme for the direct calculation of the cyclic steady state, as opposed to a naive transient time-stepping from zero initial conditions as presented in Chapter 4. The presented benchmark examples will include the first three fundamental modes of the vibrating nanotube, as well as the micro-electro-mechanical disk resonator in dynamic steady contact from Chapter 4.

5.1 Modal Decomposition

We will first discuss a traditional modal analysis as in [103, p.580]. This analysis will help us define the cyclic steady state notion, and will serve as an alternative semi-analytical approach to benchmark the numerical methods at small deformation (see Section 5.6). To this end, let us assume that a mechanical system following equations (4.24) and (4.25) is excited at a frequency ω by a driving potential

$$\bar{\Phi}(t) = \Phi_0 + \tilde{\Phi}\cos\omega t\,, \tag{5.1}$$

where Φ_0 is a constant potential, and $\tilde{\Phi}$ the amplitude of the oscillating part. Then we find the first-order approximation to the displacement

$$\mathbf{U} \approx \mathbf{U}_0 + \tilde{\mathbf{U}}\,, \tag{5.2}$$

with a constant part of the displacement $\mathbf{U}_0$, and a time-dependent part of the displacement $\tilde{\mathbf{U}}$. We find $\mathbf{U}_0$ and the constant electrical potential $\mathbf{\Phi}_0$ from the quasi-static solution of (4.26), (4.27) for a constant load $\bar{\Phi} = \Phi_0$. The time-dependent part of the displacement approximation $\tilde{\mathbf{U}}$ is then obtained from the linearized equations (4.24) around the state

$(\mathbf{U}_0, \mathbf{\Phi}_0, \Phi_0)$,

$$\mathbf{M}\ddot{\tilde{\mathbf{U}}} + \mathbf{D}\dot{\tilde{\mathbf{U}}} + \mathbf{K}_U\tilde{\mathbf{U}} = \mathbf{F}_\Phi \cos\omega t\,, \tag{5.3}$$

where $\mathbf{K}_U = \frac{\partial \mathbf{R}}{\partial \mathbf{U}}(\mathbf{U}_0, \mathbf{\Phi}_0, \Phi_0)$, and $\mathbf{F}_\Phi = -\frac{\partial \mathbf{R}}{\partial \Phi}(\mathbf{U}_0, \mathbf{\Phi}_0, \Phi_0)\tilde{\Phi}$. Following [103, p.580], we find the real eigenpairs $(\omega_i, \bar{\mathbf{U}}_i)$ corresponding to the undamped, homogeneous system

$$\mathbf{K}_U\bar{\mathbf{U}}_i = \omega_i^2\mathbf{M}\bar{\mathbf{U}}_i\,, \tag{5.4}$$

such that the solution to (5.3) can be written as

$$\tilde{\mathbf{U}} = \sum_{i=1}^{n} \bar{\mathbf{U}}_i y_i(t)\,, \tag{5.5}$$

where $\bar{\mathbf{U}}_i$ are the eigenvectors, and y_i the scalar modal participation factor. Rayleigh damping of the form $\mathbf{D} = \alpha_M\mathbf{M} + \beta_K\mathbf{K}_U$ is assumed here. Then equations (5.3) can be de-coupled as

$$m_i\ddot{y}_i + d_i\dot{y}_i + k_i y_i = f_i \cos\omega t\,, \tag{5.6}$$

with $m_i = \bar{\mathbf{U}}_i^T\mathbf{M}\bar{\mathbf{U}}_i$, $d_i = \bar{\mathbf{U}}_i^T\mathbf{D}\bar{\mathbf{U}}_i$, $k_i = \bar{\mathbf{U}}_i^T\mathbf{K}_U\bar{\mathbf{U}}_i$ and $f_i = \bar{\mathbf{U}}_i^T\mathbf{F}_\Phi$. Let us assume that the eigenvectors are normalized, such that $m_i = 1$. By noting that $k_i = \omega_i^2 m_i$, and introducing $\xi_i = d_i/(2\omega_i)$, we rewrite (5.6) as

$$\ddot{y}_i + 2\omega_i\xi_i\dot{y}_i + \omega_i^2 y_i = f_i \cos\omega t\,, \tag{5.7}$$

to which analytical solutions exist for given initial conditions $y_{i0} = \bar{\mathbf{U}}^T\mathbf{M}\tilde{\mathbf{U}}_0$ and $\dot{y}_{i0} = \bar{\mathbf{U}}^T\mathbf{M}\dot{\tilde{\mathbf{U}}}_0$ (see e.g. [103, p.582]). In particular, for zero initial conditions and when the system is under-damped with $0 < \xi < 1$, the homogeneous solution will decay exponentially with time-constant $1/(\omega_i\xi_i)$, and the overall solution is given by

$$y_i = \frac{f_i}{\omega_i^2} V_h \exp\left(-\tau_i\xi_i\right)\cos\left(\tau_i\sqrt{1-\xi_i^2} - \varphi_h\right) + \frac{f_i}{\omega_i^2} V_p \cos\left(\eta_i\tau_i - \varphi_p\right), \tag{5.8}$$

$$V_h = -V_p\frac{\cos\varphi_p}{\cos\varphi_h}\,, \tag{5.9}$$

$$\varphi_h = \arctan\frac{\xi_i\cos\varphi_p + \eta_i\sin\varphi_p}{\sqrt{1-\xi_i^2}\cos\varphi_p}\,, \tag{5.10}$$

$$V_p = \left[(1-\eta_i^2)^2 + (2\xi_i\eta_i)^2\right]^{-1/2}\,, \tag{5.11}$$

$$\varphi_p = \arctan\frac{2\eta_i\xi_i}{1-\eta_i^2}\,, \tag{5.12}$$

with $\eta_i = \omega/\omega_i$, $\tau_i = \omega_i t$, which attains its maximum at $\eta_i = \sqrt{1-2\xi_i^2}$.

5.2 Direct Solution of Cyclic Steady States

While the solution as presented in the previous section can be very efficient for systems that operate in the linear regime, the consideration of the fully coupled nonlinear equations (4.24), (4.25) becomes necessary for large deformations, or when contact occurs. In the following we assume that the damping is sufficient such that the system will reach a cyclic steady state for a harmonic load as in (5.1), and such that the eigenvalues as obtained from the linear analysis are close to the resonance modes of the nonlinear system. In order to find cyclic steady state solutions for the nonlinear coupled system excited at $\omega = \omega_i$, we then consider a method as advocated in [111], and that has been recently applied to cyclic steady states of treaded rolling bodies [112]. In our case the period is given by $T = 2\pi/\omega$. Consider the mechanical state $\mathbf{X} = [\mathbf{U}; \dot{\mathbf{U}}]$. The problem reads: Given a period T, find $\mathbf{X}_0$ such that

$$\mathbf{H}(\mathbf{X}_0) = \mathbf{X}(T) - \mathbf{X}_0 = \mathbf{0}\,, \tag{5.13}$$

where $\mathbf{X}(T)$ evolves according to (4.24), (4.25) with initial conditions $\mathbf{X}_0$.[1] The solution to (5.13) will be found using the Newton-Raphson method, which requires the linearized mechanical equilibrium:

$$\mathbf{M}\delta\ddot{\mathbf{U}} + \mathbf{D}\delta\dot{\mathbf{U}} + \frac{\partial \mathbf{R}}{\partial \mathbf{U}}(\mathbf{U}, \mathbf{\Phi})\delta\mathbf{U} = \mathbf{0}\,. \tag{5.14}$$

Now the method reads: Given $\mathbf{X}_0^i$, we update $\mathbf{X}_0^{i+1} = \mathbf{X}_0^i + \delta\mathbf{X}_0^i$, where we find $\delta\mathbf{X}_0^i$, such that

$$D\mathbf{H}[\mathbf{X}_0^i](\delta\mathbf{X}_0^i) = -\mathbf{H}(\mathbf{X}_0^i)\,. \tag{5.15}$$

Here the operator reads

$$D\mathbf{H}[\mathbf{X}_0](\delta\mathbf{X}_0) = \delta\mathbf{X}(T) - \delta\mathbf{X}_0\,, \tag{5.16}$$

where $\delta\mathbf{X}(T)$ evolves according to the linearized equation (5.14) with initial conditions $\delta\mathbf{X}_0$ along the path $\mathbf{X}(t)$ that evolves according to (4.24), (4.25) with initial conditions $\mathbf{X}_0$.

In order to assemble the operator $D\mathbf{H}[\mathbf{X}_0]$ in each Newton step, one may iteratively calculate each column $D\mathbf{H}[\mathbf{X}_0]_{:,i}$ via

$$D\mathbf{H}[\mathbf{X}_0]_{:,i} = D\mathbf{H}[\mathbf{X}_0](\mathbf{e}_i)\,, \tag{5.17}$$

with basis vectors $\mathbf{e}_i \in \mathbb{R}^N$, $i = 1, \ldots, N$. While this gives the full operator for a direct solution of (5.15), the assembly via (5.17) is expensive. As advocated in [112], we employ the generalized minimal residual method (GMRES). To this end let us denote $A = D\mathbf{H}[\mathbf{X}_0^i]$, $b = -\mathbf{H}(\mathbf{X}_0^i)$ and $x = \delta\mathbf{X}_0^i$, so that for each Newton step 'i' we wish to solve $Ax = b$. Then one computes the m-th order Krylov subspace $\text{span}\{b, Ab, A^2b, \ldots, A^{m-1}b\}$ by a standard Arnoldi iteration. The minimizer of the residual $||Ax - b||_2$ over this subspace gives the

[1] Note that one could also treat the period T as an additional unknown to solve for, but here we assume T as a given parameter matching the excitation frequency of the external load.

approximate solution which we set to $\delta\mathbf{X}_0^i$. For each Newton step, one has to evolve (5.13) according to (4.24), (4.25) with initial conditions $\mathbf{X}_0^i$. Subsequently, one evolves $(m-1)$ times the linearized equations (5.16) according to (5.14), with multiple initial conditions $b, Ab, \ldots, A^{m-2}b$. In this work we find the dimension m, by requiring $||Ax - b|| < \delta||b||$ during the Arnoldi iteration, where $\delta = 10^{-3}$ as in [112]. The algorithm is summarized in Alg. 5.1. We refer to [113] for a more detailed discussion on GMRES and Arnoldi iterations.

Cyclic Steady State Solution

Given $\mathbf{X}_0^0 = [\mathbf{U}_0^0, \dot{\mathbf{U}}_0^0]$.
LOOP i

1. Calculate $\mathbf{H}(\mathbf{X}_0^i)$ according to (5.13).
2. Iteratively form m-th order Krylov subspace by an Arnoldi iteration and evolving $D\mathbf{H}[\mathbf{X}_0^i](.)$ according to (5.16).
3. Find the minimizer $\tilde{\mathbf{X}}$ of the residual $||D\mathbf{H}[\mathbf{X}_0^i](\tilde{\mathbf{X}}) + \mathbf{H}(\mathbf{X}_0^i)||_2$ over this subspace by a least-square approximation.
4. Set $\delta\mathbf{X}_0^i = \tilde{\mathbf{X}}$.
5. Check convergence $||\delta\mathbf{X}_0^i||_2/||\mathbf{X}_0^i||_2 < TOL$ and update $\mathbf{X}_0^{i+1} = \mathbf{X}_0^i + \delta\mathbf{X}_0^i$.

Algorithm 5.1: Cyclic steady state solution via GMRES.

5.3 Critical Time-step

In the following examples we will consider that a cyclic steady state is reached, when the relative L2-norm of $\mathbf{H}(t_n) = \mathbf{X}(t_n) - \mathbf{X}(t_n - T)$ after a period T,

$$\text{Residual} = \sqrt{\frac{\sum_i |X_i(t_n) - X_i(t_n - T)|^2}{\sum_i |X_i(t_n)|^2}}\,, \tag{5.18}$$

is converged by six orders of magnitude. All accuracy considerations have been done within this scope. Note that another tolerance setting will change the accuracy requirements on the discretization, and results will differ from the current study.

In order to obtain accurate results and optimum convergence rates, it is crucial to ensure a converged discretization in the time-domain. Such estimates can be obtained by noting the period accuracy of the time-stepper as discussed for example in [114]. In our examples we require the finite element solution at steady state to be converged by six orders of magnitude. Given the damping ratio ξ, we find the number of time-steps per cycle $T/\Delta t_n$ for the centered-difference scheme and for the mid-point rule by monitoring the residual (5.18), such that convergence is achieved. In addition, the requirement (4.40) must be met for the explicit case.

	$\xi_{i,1}$	1	2	3	4	5	6
Mode 1:	$1.1 \cdot 10^{-1}$	$1.0 \cdot 10^{0}$	$3.2 \cdot 10^{-3}$	$1.0 \cdot 10^{-4}$	$3.1 \cdot 10^{-6}$	$5.3 \cdot 10^{-9}$	
Mode 2:	$1.9 \cdot 10^{-2}$	$1.0 \cdot 10^{0}$	$2.8 \cdot 10^{-2}$	$5.4 \cdot 10^{-5}$	$3.9 \cdot 10^{-7}$		
Mode 3:	$7.2 \cdot 10^{-3}$	$1.0 \cdot 10^{0}$	$6.2 \cdot 10^{-1}$	$7.1 \cdot 10^{-3}$	$1.7 \cdot 10^{-4}$	$1.3 \cdot 10^{-6}$	$9.2 \cdot 10^{-8}$
	$\xi_{i,2}$	1	2	3	4	5	6
Mode 1:	$5.6 \cdot 10^{-2}$	$1.0 \cdot 10^{0}$	$5.1 \cdot 10^{-3}$	$5.0 \cdot 10^{-4}$	$7.9 \cdot 10^{-6}$	$2.3 \cdot 10^{-7}$	
Mode 2:	$9.4 \cdot 10^{-3}$	$1.0 \cdot 10^{0}$	$2.4 \cdot 10^{-2}$	$1.3 \cdot 10^{-4}$	$1.9 \cdot 10^{-6}$	$7.5 \cdot 10^{-8}$	
Mode 3:	$3.6 \cdot 10^{-3}$	$1.0 \cdot 10^{0}$	$2.6 \cdot 10^{-1}$	$4.9 \cdot 10^{-3}$	$1.2 \cdot 10^{-4}$	$1.3 \cdot 10^{-5}$	$4.4 \cdot 10^{-8}$

Table 5.1: Nanotube vibration example: residual convergence $||\delta \mathbf{X}_0^i||_2/||\mathbf{X}_0^i||_2$, $i = 1, \ldots, 6$ of Alg. 5.1 for Mode 1-3 and various damping ratios ξ.

5.4 Nanotube Vibration – revisited

Our first example deals with the a carbon nanotube vibration as discussed in Section 4.8. We employ the same material and simulation parameters from the previous discussion for the transient solution. In addition, we employ the direct steady state solution following Alg. 5.1 to satisfy (5.13).

Remember that in Section 4.8 we have tested various modes of excitation, for damping values $\xi_i = \alpha_M/(2\omega_i)$, $i = 1, \ldots, 3$, as resulting from a damping matrix $\mathbf{D} = \alpha_M \mathbf{M}$, with $\alpha_M \in \{5 \cdot 10^9 \text{ s}^{-1}, 10 \cdot 10^9 \text{ s}^{-1}\}$. In Fig. 5.1 we review the vertical tip displacement and velocity as we release the system from zero initial conditions for the case $\alpha_M = 5 \cdot 10^9 \text{ s}^{-1}$ and the load $V_{\text{DC}} = 60$ V and $V_{\text{AC}} = 40$ V at various modes. As we have noted, the number of cycles to reach a steady state for the transient solution is increased at the higher modes, due to the lower damping present.

We now employ Alg. 5.1 in order to find solutions to (5.13) more efficiently. After finding the initial conditions $\mathbf{X}_0$ according to Alg. 5.1, we have evolved equations (4.24) and (4.25) with these initial conditions over one period T in order to compare the results to the transient solution as obtained in Section 4.8. In Fig. 5.1, we monitor the vertical tip displacement and velocity for Mode 1-3 at $\xi_1 = 5.6 \cdot 10^{-2}$, $\xi_2 = 9.4 \cdot 10^{-3}$, and $\xi_3 = 3.6 \cdot 10^{-3}$ respectively. The direct solution via Alg. 5.1 shows excellent agreement when compared to the full time-stepping trough the transient phase from zero initial conditions. In this plot we have labeled various time-instants $1 - 5$ in the steady state displacement [Fig. 5.1(third column)], as well as in the phase portrait [Fig. 5.1(fourth column)].

As mentioned before, we consider a system to have reached a steady state is reached when the residual (5.18) has dropped by six orders of magnitude. In Fig. 5.2(top) we plot the residual of the transient solution [Fig. 5.2(top, left)], as well as the cyclic steady state solution (CSS) via Alg. 5.1 [Fig. 5.2(top,right)] at various damping values. While the number of cycles to reach convergence in the transient solution increases for lower damping values, the number of Newton iterations of the CSS solution remained at about $5 - 6$ Newton

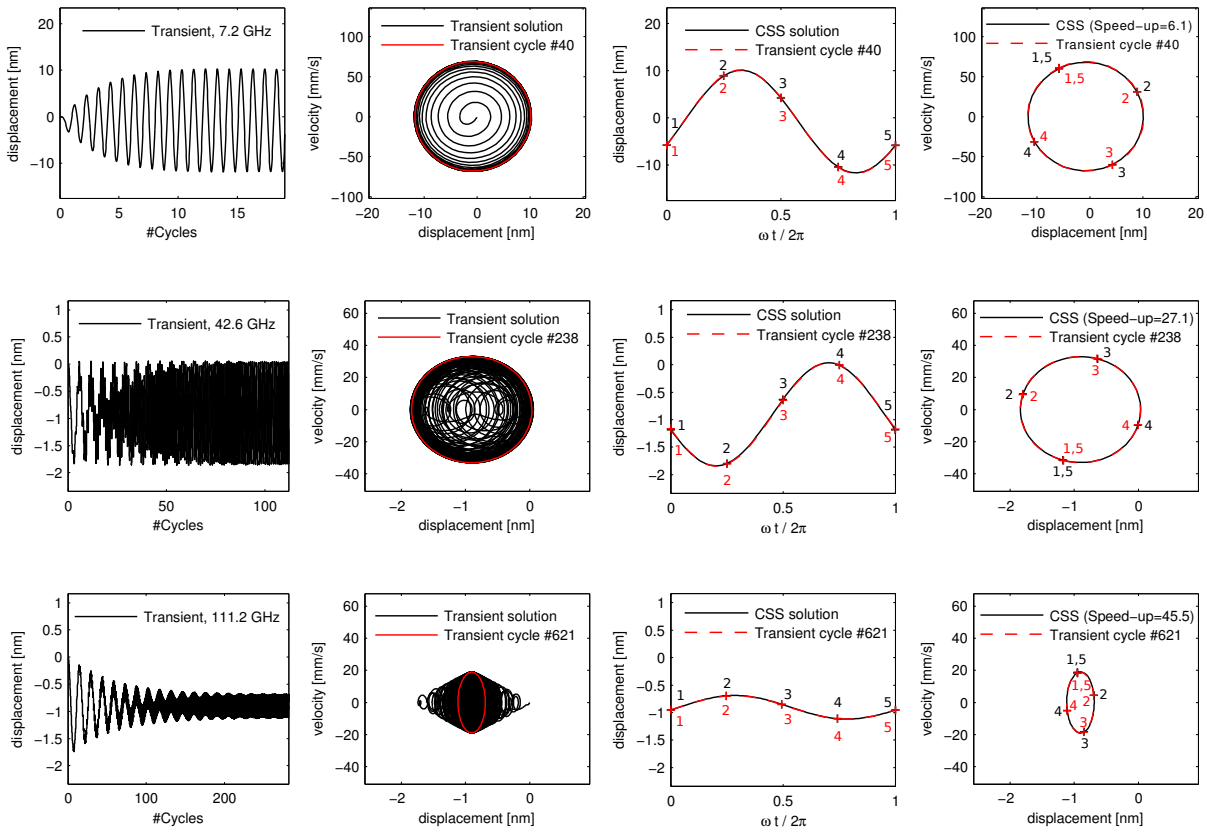

Figure 5.1: Nanotube vibration: transient solution and cyclic steady state solution (CSS) via GMRES (Alg. 5.1) of the tip-displacement and velocity for (top) Mode 1, (middle) Mode 2, (bottom) Mode 3.

iterations. We print the numerical values of the Newton residual of the CSS solution in Table 5.1 for the case $\alpha_M = 5 \cdot 10^9$ s^{-1} as plotted in Fig. 5.2(top,right), as well as for the case $\alpha_M = 10 \cdot 10^9$ s^{-1}. In both cases, we typically encounter convergence by six order of magnitudes within 4 to 6 iterations.

We have measured the speed-up S by the computational time $T_{\text{transient}}$ that is required to evolve equations (4.24) and (4.25) from zero initial conditions until the residual (5.18) is converged by six orders of magnitude, as well as the computational time T_{css} that is required to find convergence of (5.18) by six orders of magnitude via Alg. 5.1:

$$S = \frac{T_{\text{transient}}}{T_{\text{css}}} \,. \tag{5.19}$$

The speed-up is increased at the higher modes, where the number of cycles to reach the steady state is increased for the transient solution. We measured the speed-ups $S = 3.3$ for Mode 1 at $\xi_1 = 1.1 \cdot 10^{-1}$, $S = 6.1$ for Mode 1 at $\xi_1 = 5.6 \cdot 10^{-2}$, $S = 20.6$ for Mode

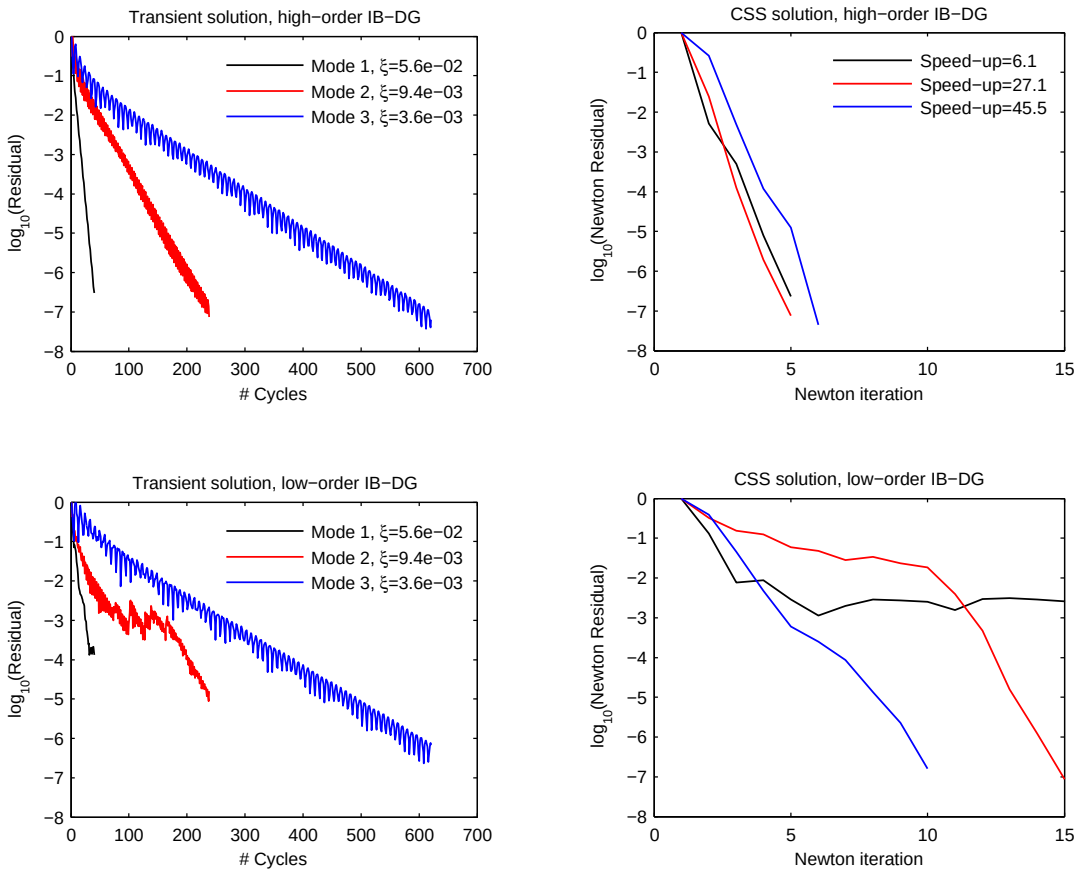

Figure 5.2: Nanotube vibration: (top) convergence of the residual (5.18) when using the high-order IB-DG for (left) the transient solution and (right) the cyclic steady state solution (CSS) via GMRES (Alg. 5.1); (bottom) convergence issues of the low-order immersed boundary method.

2 at $\xi_2 = 1.9 \cdot 10^{-2}$, $S = 27.1$ for Mode 2 at $\xi_2 = 9.4 \cdot 10^{-3}$, and $S = 32.0$ for Mode 3 at $\xi_3 = 7.2 \cdot 10^{-3}$, $S = 45.5$ for Mode 3 at $\xi_3 = 3.6 \cdot 10^{-3}$. Please see Section 5.6 for a further discussion of these results.

We remark that the use of a higher-order immersed boundary method as discussed in Section 4.8 in order to account for the singularity in the electrical field in this example becomes absolutely necessary for (i) any accurate and physically meaningful results; and (ii) in order to obtain convergence during the Newton iteration of the cyclic steady state solution via Alg. 5.1. As can be observed in Fig. 5.2(bottom), the use of a low-order immersed boundary method resulted in reduced or even incomplete convergence of the residual for the transient solution [Fig. 5.2(bottom,left)], as well as for the CSS solution [Fig. 5.2(bottom,right)]. This is consistent to what has been observed in Section 4.7 for the electro-mechanical pull-in in

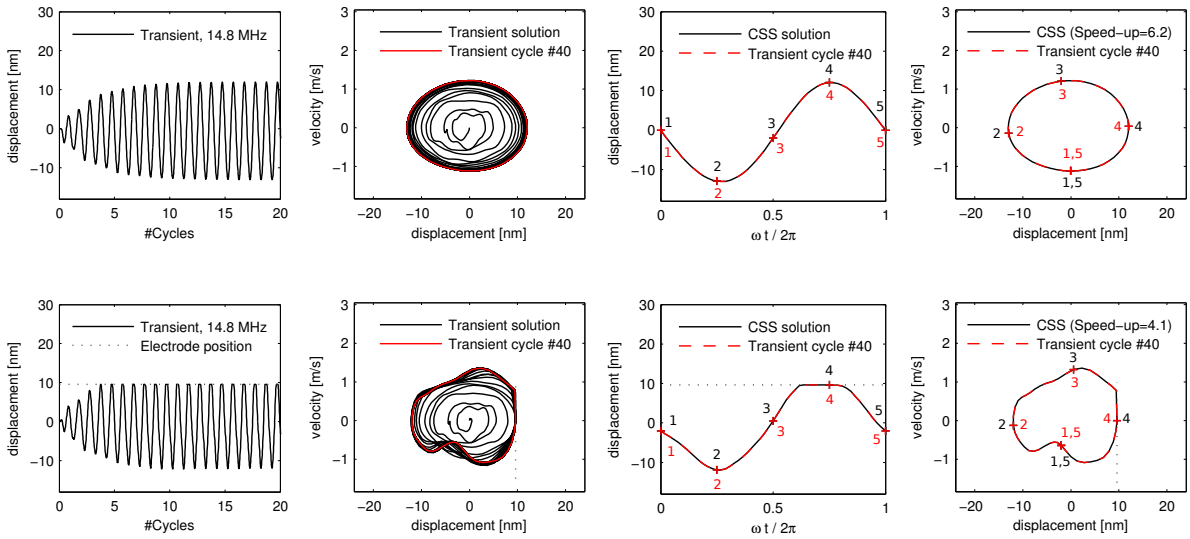

Figure 5.3: Reso-switch example: transient solution and cyclic steady state solution (CSS) via GMRES (Alg. 5.1) of the top-disk-node displacement and velocity for (top) *Load 2*, and (bottom) *Load 3*.

the quasi-static case [see Fig. 4.6(right)].

5.5 Reso-switch – revisited

The second example revisits the micro-electro-mechanical disk resonator as discussed in Section 4.9. We employ the same simulation parameters as in Section 4.9, and in addition we test Alg. 5.1 for a direct steady state solution.

Remember that in Section 4.9 we have tested various loading cases. In particular we have examined *Load 2*, where the bias-voltage $V_{DC} = 6.45$ kV, $V_{AC} = 4.3$ kV, $V_D = 240$ V, and the initial gap to the output electrodes $g_0 = 2.2$ μm. As well as *Load 3*, where the bias-voltage $V_{DC} = 6.45$ kV, $V_{AC} = 4.3$ kV, $V_D = 240$ V, and the initial gap to the output electrodes is $g_0 = 9.6$ nm. For both cases *Load 2* and *3* we have assumed the damping $\xi = 5.6 \cdot 10^{-2}$. In Fig. 5.3 we review the top-disk-node displacement and velocity as we release the system from zero initial conditions during *Load 2* and *3*. As we have noted, there is no contact for *Load 2* [Fig. 5.3(top)], whereas we observe a steady contact state for *Load 3* due to the reduced initial distance g_0 from the disk to the output electrodes [see Fig. 5.3(bottom)].

We now employ Alg. 5.1 in order to find solutions to (5.13). As done in the previous example for the nanotube, we find the initial conditions $\mathbf{X}_0$ according to Alg. 5.1, and we evolve equations (4.24) and (4.25) with these initial conditions over one period T in order to compare the results to the transient solution as obtained in Section 4.9. In Fig. 5.3, we monitor the top-disk-node displacement and velocity for *Load 2* and *3* respectively. As in the

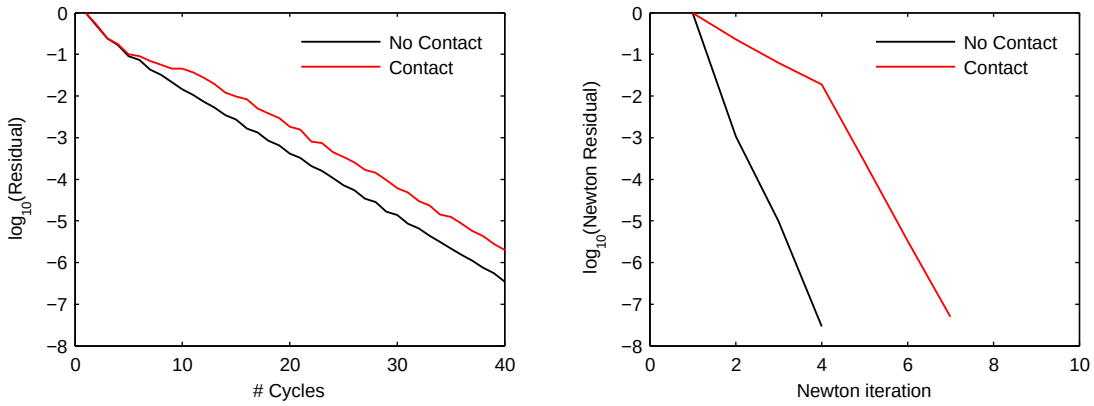

Figure 5.4: Reso-switch example: convergence of the residual (5.18) for *Load 2* in black (no contact), and for *Load 3* in red (contact) during (left) the transient solution from zero initial conditions, and (right) the direct cyclic steady state solution (CSS) via Alg. 5.1.

previous example, the direct solution via Alg. 5.1 shows an equally excellent agreement when compared to the full time-stepping trough the transient phase from zero initial conditions. In this plot we have labeled various time-instants $1-5$ in the steady state displacement [Fig. 5.3(third column)], as well as in the phase portrait [Fig. 5.3(fourth column)]. Note in particular that the CSS algorithm is capable to handle such a highly non-linear response at steady state, involving electro-mechanical impact. To our knowledge, this is a first time demonstration of the CSS solution to electro-mechanical impact problems.

Again we have tracked the residual (5.18) for the transient as well as the CSS solution. In Fig. 5.4 we plot the residual for *Load 2* in black (no contact), and for *Load 3* in red (contact). We observe a slightly slower convergence for *Load 3* to reach a steady contact state during the transient solution when compared to *Load 2*, where no contact occurs [Fig. 5.4(left)]. In this example we required about five more cycles to achieve convergence for *Load 3* as compared to *Load 2* in the transient solution. This is also observed in Fig. 5.4(right) for the CSS solution, where convergence is reached after 7 iterations for *Load 3* involving impact, and convergence is reached after 4 iterations for *Load 2* without impact. The observed speed-up in this example is $S = 6.2$ for *Load 2*, and slightly lower $S = 4.1$ for *Load 3*.

Note that for *Load 2* and *3* we have assumed a damping value $\xi = 5.6 \cdot 10^{-2}$. We now test the numerical solutions for $V_{DC} = 6.45$ kV, $V_{AC} = 4.3$ kV, $V_D = 240$ V, and the initial gap to the output electrodes $g_0 = 2.2$ μm as in *Load 2*, but with varying damping values $\xi \in \{1.4 \cdot 10^{-2}, 2.8 \cdot 10^{-2}, 5.6 \cdot 10^{-2}, 2.2 \cdot 10^{-1}\}$. As the damping values become lower, we have to adjust the number of time-steps in order to achieve convergence of the residual due to the higher accuracy requirements (see Section 5.3). In this study we have used $2\pi/(\omega \Delta t_n) = 36$ steps per cycle for $\xi = 2.2 \cdot 10^{-1}$, 52 steps per cycle for $\xi = 5.6 \cdot 10^{-2}$, 72 steps per cycle for $\xi = 2.8 \cdot 10^{-2}$, and 104 steps per cycle for $\xi = 1.4 \cdot 10^{-2}$. Typical convergence plots for

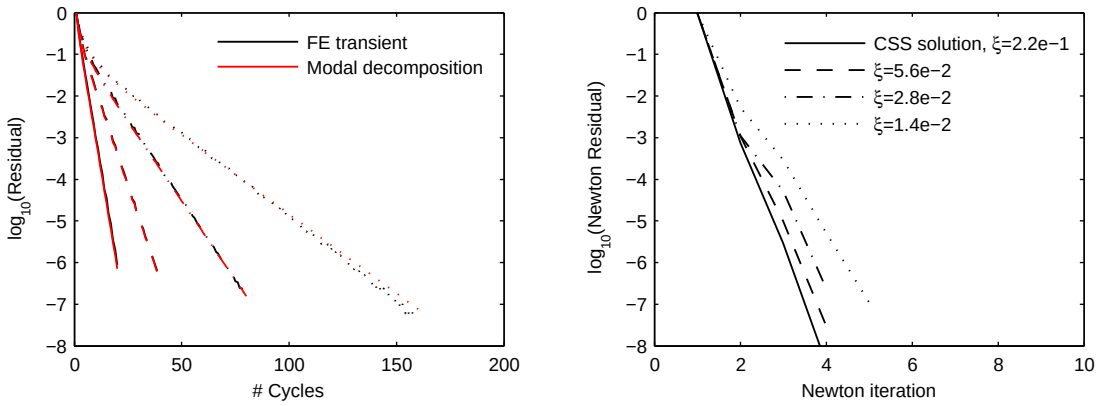

Figure 5.5: Reso-switch example: (left) convergence of the residual for the transient solution (black) and the modal decomposition analysis (red) at various damping ratios as indicated in the right figure; (right) convergence of the residual of the direct cyclic steady state solution (CSS) via Alg. 5.1 for various damping ratios ξ.

the transient solution are shown in Fig. 5.5(left), and for the CSS solution in Fig. 5.5(right). Similar observations as with the nanotube vibration example are made: while the transient solution requires significantly more cycles to reach a steady state at lower damping values, the CSS solution is converged within 4 to 5 Newton steps. Thus the observed speed-ups are higher at lower damping values. In accordance with (5.19) we have measured $S = 3.5$ at $\xi = 2.2 \cdot 10^{-1}$, $S = 6.2$ at $\xi = 5.6 \cdot 10^{-2}$, $S = 11.2$ at $\xi = 2.8 \cdot 10^{-2}$, and $S = 16.7$ at $\xi = 1.4 \cdot 10^{-2}$. We will summarize all performance tests done for the reso-switch example, as well as for the nanotube vibration in the following section.

5.6 Performance of the GMRES algorithm and Computational Speed-up

As mentioned in Section 5.3, it is crucial for all performance tests to adjust the time-step size for a given numerical time-integration scheme in order to achieve optimum convergence of the residual (5.18). In the small deformation case, one can test the validity of the numerical time-integration by comparing the transient solution from zero initial conditions to the modal decomposition analysis as presented in Section 5.1. In the reso-switch example without contact, we have plotted the residual for the transient solution (black) and the modal decomposition analysis (red) in Fig. 5.5(left) for various damping parameters. The evolution of the modal equations in this case has been done analytically by (5.8). We found that the first fundamental mode is sufficient to match the results from the full transient numerical

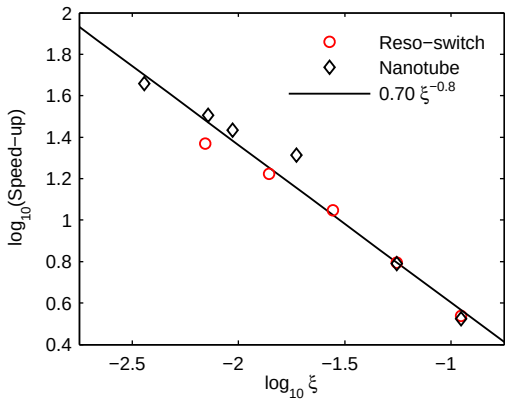

Figure 5.6: Speed-up of the direct cyclic steady state solution (CSS) via Alg. 5.1 versus a classical transient time-stepping from zero initial conditions.

solution; i.e. we approximate

$$\tilde{\mathbf{U}} \approx \bar{\mathbf{U}}_1 y_1(t)\,, \tag{5.20}$$

see also Eq. (5.5). As shown in Fig. 5.5(left), the transient solution and the modal decomposition analysis via (5.20) show very good agreement. Note again, that the modal decomposition analysis can only be used for systems that operate in the linear regime. In our case we have used the analysis to benchmark the numerical time-integrator as in Fig. 5.5(left).

As we have noted in the nanotube vibration, as well as the reso-switch example, the measured speed-ups are higher for lower damping values ξ. This is mainly due to the increased number of cycles to reach a steady state for the transient solution, whereas the Newton algorithm via Alg. 5.1 has been demonstrated to be relatively unaffected by ξ. In Fig. 5.6 we plot all speed-ups for various tests of the nanotube vibration, as well as the reso-switch. We observe power law computational speed-ups of the CSS solution in comparison to a transient solution of the form

$$S = 0.7\xi^{-0.8}\,, \tag{5.21}$$

where we have measured S according to (5.19) for the different test cases.

As mentioned in Section 5.2, we have investigated two ways to assemble the tangent operator for the direct steady state solution. While the full tangent assembly as in (5.17) will deliver most accurate results, the use of GMRES will significantly speed-up the calculation during the iterative Newton solution. In accordance with [112], we use the tolerance $||Ax - b||/||b|| < 10^{-3}$ in order to determine the number of Arnoldi iterations for each Newton step. Note that in our examples we observed that the number of Arnoldi iterations increases for lower damping values, and thus the computational speed-up shows only sub-linear growth.

Note moreover that we have only tested the cases for $\xi > 10^{-3}$ using our second order accurate time-integration. For smaller ξ, one may benefit from higher-order time-integration schemes, facing the decreased tolerances on the accuracy requirement. Such integration

schemes must be developed in the context of electro-mechanical impact, and one has to assure that the energy is conserved in the algorithmic treatment of the impact event, which is still subject to current research.

Chapter 6

Conclusion and Future Works

We have developed a high-order Eulerian-Lagrangian finite element framework for the simulation of electro-mechanical systems. While the mechanical motion is solved on a moving Lagrangian grid, the electrical field is solved on a fixed Eulerian frame with embedded boundary conditions. The method relies on a newly developed high-order immersed boundary discontinuous-Galerkin method that tracks the mechanical motion of the interface.

The immersed boundary method as presented in Chapter 3 is based on a high-order boundary representation, as well as a high-order field approximation in a small band of elements cut by the boundary. The boundary shape is approximated locally by possibly nonlinear geometric primitives. We have developed elements for straight-, circular-, and corner-boundaries in two dimensions. Consequently, the field approximation is spanned by shape functions that are motivated by the analytical solution of the underlying PDE in the proximity of the corresponding boundary features. Employing this higher-order solution space has several advantages compared to low-order approximations. As a main argument to use it appears that (i) Dirichlet boundary conditions along Γ can be strongly enforced, (ii) the gradient interpolation is more accurate than low-order embedded boundary methods, (iii) no oscillations occur in the gradient and no post-processing is required to obtain smooth results, and (iv) singularities in the PDE can be incorporated in a natural way. All enhanced elements are coupled together and to the rest of the standard FE domain via DG. The DG-based immersed boundary method is very robust, and we performed several benchmark tests to demonstrate the performance and convergence. The method is also efficient, in the sense that a higher-order interpolation is employed only around the boundary where a high accuracy for the gradient field is needed, whereas the remainder of the domain may utilize low-order approximations. We do require heuristic parameters to deal with intersection adaption and singularities. However, the method has been found to be relatively insensitive to these. Moreover, our DG method does feature a stabilization term α, as in most immersed boundary methods there is a stabilization needed at some point. In this work we choose α following a convergence study to obtain optimum results. While this gave us very accurate results in the discussed examples, the selection of α is done by the user's choice, and future work may consider alternative DG methodologies that provide for accu-

racy and stability with an automated stability parameter. The focus of this work is on the enhancement of the gradient accuracy along higher-order immersed boundary shapes, which has been successfully adopted. We note that the basic idea is very simple in two dimensions and can be extended to more complicated boundary shapes, or other types of PDEs. In order to deal with three space dimensions, the basic strategy will remain the same, but an extended library of geometric primitives, and boundary intersection scenarios will become necessary. While the development of such libraries requires clearly more effort in the three-dimensional setup as compared to the present two-dimensional work, there is a finite set of cases in the end. Once these libraries have been created, we believe that the proposed methodology has good potential to improve upon robustness and accuracy in comparison to current immersed boundary technologies, especially if higher-order boundary features are present or singularities in the field have to be resolved.

As a main focus of this work, we have applied the immersed boundary method to a coupled Eulerian-Lagrangian finite element method to solve for electro-mechanical problems. We put a special focus on (i) the accurate treatment of the coupling forces in the presence of non-linear boundary features, (ii) the treatment of singularities in the electrical field and the resulting Maxwell traction around corners, (iii) the quasi-static, as well as implicit and explicit solution for dynamically coupled electro-mechanical problems with non-conforming meshes, (iv) the incorporation of energy-conserving dynamical contact algorithms, and (v) the treatment of electrical boundary conditions during electro-mechanical impact. The high-order boundary treatment has been shown to be necessary in order to obtain accurate surface tractions as arise due to the electrical field, as well as in order to obtain convergence during the global Newton-Raphson iteration. In particular, for an analytical benchmark example in the presence of a corner, the error in the traction has been improved from about 40% using a low-order method to less than 1% using the higher-order method. The solution of the coupled equations is carried out by means of an operator split, where in each iteration step the electrical field is solved for a fixed mechanical boundary position, and the resulting electrical forces consecutively drive the mechanical motion. This staggered approach has been demonstrated to deliver linear convergence rates. A boundary motion over several elements of the (fixed) electrical mesh has been demonstrated, which appears to be one of the main advantages of the presented mixed Eulerian-Lagrangian formulation, versus traditional solution strategies such as ALE or the boundary element method: large mesh-motions and topological changes will not result in any mesh distortion, or ill-conditioned equations, and no remeshing will become necessary. The incorporation of mechanical contact in the quasi-static as well as dynamical setting thus follows naturally, and has been demonstrated for a resonant switch that is operated at resonance in a cyclic steady contact state.

Finally, we have presented a numerical method to efficiently find the cyclic steady state response of electro-mechanical devices that are excited at resonance. The method is based on a Newton-Krylov shooting scheme, and features a full-field simulation of the mechanical deformation and the electrical field, incorporating dynamical impact. The proposed direct method to solve for cyclic steady states has been demonstrated for two NEMS/MEMS examples, including the vibration of a carbon nanotube at ultra-high frequencies > 1 GHz,

and the excitation of a wine-glass disk resonator in a forced vibration, as well as in dynamic steady contact state. For the presented examples, we show excellent agreement of the direct solution of the cyclic steady state in comparison to the transient solution from zero initial conditions. The computational speed-up of the discussed examples scales inversely with the damping ξ according to $S = 0.7\xi^{-0.8}$, where we tested $\xi > 10^{-3}$.

Further extensions of the current work are envisioned to three dimensional problems, the development of monolithic solution schemes, as well as the incorporation of dynamical contact algorithms for two elastic bodies. While such enhancements clearly require some more effort, the presented technology appears to have high potential to improve upon existing technologies, especially when highly nonlinear coupling terms arise, such as due to singular forces or impacting bodies. We note that, due to the strict accuracy requirements, the presented second order time-integration schemes will become very expensive for damping ratios $\xi < 10^{-3}$. The development of higher-order time-integration schemes in the context of energy-conserving electro-mechanical impact algorithms may improve upon efficiency. A further incorporation of modern material models to simulate electro-active polymers or carbon nanotubes will benefit a most realistic physical simulation. Especially the use of micro-macro models in this context seems promising. Additionally, the methodology will allow for the incorporation and coupling to other physical effects of thermal nature, or due to external fluid flow. In general, we confirm that the high-order Lagrangian-Eulerian finite element approach with immersed boundary methods as presented in this study sets the stage for great flexibility in the enhanced multi-physics simulation capabilities.

Bibliography

[1] M. Chandhok, S. Goyal, S. Carson, S.-J. Park, G. Zhang, A.M. Myers, M.L. Leeson, M. Kamna, F.C. Martinez, A.R. Stivers, G.F. Lorusso, J.V. Hermans, E. Hendrickx, S. Govindjee, G. Brandstetter, and T.A. Laursen. Compensation of overlay errors due to mask bending and non-flatness for EUV masks. *Proc. SPIE*, 7271:72710G–1–12, 2009.

[2] M. Nataraju, J. Sohn, A.R. Mikkelson, K.T. Turner, R.L. Engelstad, and C.K. Van Peski. EUV mask and chuck analysis: simulation and experimentation. *Proceedings of SPIE*, 6151:61510C–1–11, 2006.

[3] Y. Lin, T. Riekkinen, W.-C. Li, E. Alon, and C.T.-C. Nguyen. A Metal Micromechanical Resonant Switch for On-Chip Power Applications. *IEEE IEDM11*, pages 497–500, 2011.

[4] J.A. Weldon, B.J. Alemán, A. Sussman, W. Gannett, and A.K. Zettl. Sustained mechanical self-oscillations in carbon nanotubes. *Nano Letters*, 10:1728–1733, 2010.

[5] F. Cirak and M. West. Decomposition contact response (DCR) for explicit finite element dynamics. *International Journal for Numerical Methods in Engineering*, 64:1078–1110, 2005.

[6] ITRS. International Technology Roadmap for Semiconductors. *http://public.itrs.net/*, 2013.

[7] G. Brandstetter and S. Govindjee. Analytical treatment of the deformation behavior of extreme-ultraviolet-lithography masks during electrostatic chucking. *Journal of Micro/Nanolithography, MEMS, and MOEMS*, 11(4):043005–1–10, 2012.

[8] G. Brandstetter and S. Govindjee. Particle contamination effects in extreme ultraviolet lithography: enhanced theory for the analytical determination of critical particle sizes. *Journal of Micro/Nanolithography, MEMS, and MOEMSJournal of Micro/Nanolithography, MEMS, and MOEMS*, 11(2):023011–1–8, 2012.

[9] M.A. Abdelmoneum, J. Wang, M.U. Demirci, and C.T.-C. Nguyen. Stemless wineglass-mode disk micromechanical resonators. In *Proceedings, 16th Int. IEEE Micro Mechanical Systems Conf., Kyoto, Japan*, pages 698–701, 2003.

[10] Y. Lin, W.-C. Li, Z. Ren, and C.T.-C. Nguyen. The micromechanical resonant switch ("Resoswitch"). *Tech. Digest, 2008 Solid-State Sensor, Actuator, and Microsystems Workshop, Hilton Head, South Carolina*, pages 40–43, 2008.

[11] Y. Lin, R. Liu, W.-C. Li, M. Akgul, and C.T.-C. Nguyen. A Micromechanical resonant charge pump. In *Solid-State Sensors, Actuators and Microsystems (TRANSDUCERS & EUROSENSORS XXVII)*, pages 1727–1730, Barcelona, Spain, 2013.

[12] Y. Lin, R. Liu, W.-C. Li, and C.T.-C. Nguyen. Polycide contact interface to suppress squegging in micromechanical resoswitches. In *Micro Electro Mechanical Systems (MEMS), 2014 IEEE 27th International Conference*, pages 1273–1276, San Francisco, CA, 2014.

[13] S. Iijima. Helical microtubules of graphitic carbon. *Nature*, 354:56–58, 1991.

[14] P.G. Collins, A.K. Zettl, H. Bando, A. Thess, and R.E. Smalley. Nanotube Nanodevice. *Science*, 278:100–103, 1997.

[15] K. Jensen, J. Weldon, H. Garcia, and A.K. Zettl. Nanotube Radio. *Nano Letters*, 7:3508–3511, 2007.

[16] B.J. Alemán, A. Sussman, W. Mickelson, and A.K. Zettl. A Carbon Nanotube-based NEMS Parametric Amplifier for Enhanced Radio Wave Detection and Electronic Signal Amplification. *Journal of Physics: Conference Series*, 302:012001–1–6, 2011.

[17] S. Govindjee and J.L. Sackman. On the use of continuum mechanics to estimate the properties of nanotubes. *Solid State Communications*, 110:227–230, 1999.

[18] K. Jensen, H.B. Peng, and A.K. Zettl. Limits of Nanomechanical Resonators. In *Nanoscience and Nanotechnology*, pages 06EX411C–68–71, 2006.

[19] B.E. Artz and L.W. Cathey. A finite element method for determining structural displacements resulting from electrostatic forces. In *IEEE Solid State Sensor and Actuator Workshop, Hilton Head, SC*, volume 1, pages 190–193, 1992.

[20] H.U. Schwarzenbach, J.G. Korvink, M. Roos, G. Sartoris, and E. Anderheggen. A micro electro mechanical CAD extension for SESES. *Journal of Micromechanics and Microengineering*, 3:118–122, 1993.

[21] U. Beerschwinger, N.G. Milne, S.J. Yang, R.L. Reuben, A.J. Sangster, and H. Ziad. Coupled Electrostatic and Mechanical FEA of a Micromotor. *Journal of Microelectromechanical Systems*, 3(4):162–171, 1994.

[22] K. Nabors and J. White. Fastcap: A multipole accelerated 3-D capacitance extraction program. *IEEE Transactions on Computer-Aided Design of Integrated Circuits and Systems*, 10(11):1447–1459, 1991.

[23] S.D. Senturia, R.M. Harris, B.P. Johnson, S. Kim, K. Nabors, M.A. Shulman, and J. White. A Computer-Aided Design System for Microelectromechanical Systems (MEMCAD). *Journal of Microelectromechanical Systems*, 1(1):3–13, 1992.

[24] X. Cai, H. Yie, P.M. Osterberg, J.R. Gilbert, S.D. Senturia, and J. White. A Relaxation/Multipole-Accelerated Scheme for Self-Consistent Electromechanical Analysis of Complex 3-D Microelectromechanical Structures. *IEEE*, pages 283–286, 1993.

[25] H. Yie, X. Cai, and J. White. Convergence properties of Relaxation versus the Surface-Newton Generalized-Conjugate Residual Algorithm for Self-consistent Electromechanical Analysis of 3-D Micro-Electro- Mechanical Structures. *IEEE*, pages 137–140, 1994.

[26] N.R. Aluru and J. White. An efficient numerical technique for electromechanical simulation of complicated microelectromechanical structures. *Sensors & Actuators: A. Physical*, 58:1–11, 1997.

[27] J.R. Gilbert, G.K. Ananthasuresh, and S.D. Senturia. 3D Modeling of Contact Problems and Hysteresis in Coupled Electro-Mechanics. *IEEE*, pages 127–132, 1996.

[28] F. Shi, P. Ramesh, and S. Mukherjee. Simulation Methods for Micro-Electro-Mechanical Structures (MEMS) with Application to a Microtweezer. *Computer and Structures*, 56(5):769–783, 1995.

[29] G. Li and N.R. Aluru. A Lagrangian Approach for Electrostatic Analysis of Deformable Conductors. *Journal of Microelectromechanical Systems*, 11(3):245–254, 2002.

[30] S. Mukherjee, Z. Bao, M. Roman, and N. Aubry. Nonlinear mechanics of MEMS plates with a total Lagrangian approach. *Computers and Structures*, 83:758–768, 2005.

[31] R. Ghosh and S. Mukherjee. Fully Lagrangian Modeling of Dynamics of MEMS With Thin Beams - Part I: Undamped Vibrations. *Journal of Applied Mechanics*, 76:051007–1–10, 2009.

[32] R. Ghosh and S. Mukherjee. Fully Lagrangian Modeling of Dynamics of MEMS With Thin Beams - Part II: Damped Vibrations. *Journal of Applied Mechanics*, 76:051008–1–9, 2009.

[33] D.K. Vu and P. Steinmann. A 2-D coupled BEM-FEM simulation of electroelastostatics at large strain. *Computer Methods in Applied Mechanics and Engineering*, 199:1124–1133, 2010.

[34] D.K. Vu and P. Steinmann. On 3-D coupled BEM-FEM simulation of nonlinear electroelastostatics. *Computer Methods in Applied Mechanics and Engineering*, 204:82–90, 2012.

[35] P. Steinmann. Computational Nonlinear Electro-Elasticity - Getting Started. In R. W. Ogden and D. J. Steigmann, editors, *Mechanics and Electrodynamics of Magneto- and Electro-Elastic Materials*, pages 181–230. Springer-Verlag, Wien, New York, 2011.

[36] T.J.R. Hughes, W.K. Liu, and T.K. Zimmermann. Lagrangian-Eulerian finite element formulation for incompressible viscous flows. *Computer Methods in Applied Mechanics and Engineering*, 29:329–349, 1981.

[37] J. Donea. Arbitrary Lagrangian-Eulerian Finite Element Methods. In T. Belytschko and T.J.R. Hughes, editors, *Computational Methods for Transient Analysis*, chapter 10, pages 473–516. North-Holland, Amsterdam, 1983.

[38] A. Collenz, F. De Bona, A. Gugliotta, and A. Soma. Large deflections of microbeams under electrostatic loads. *Journal of Micromechanics and Microengineering*, 365:365–373, 2004.

[39] V. Rochus, D. J. Rixen, and J.-C. Golinval. Monolithic modelling of electro-mechanical coupling in micro-structures. *International Journal for Numerical Methods in Engineering*, 65:461–493, 2006.

[40] Z. Gao, A. Tuncer, and A.M. Cuitiño. Modeling and simulation of the coupled mechanical-electrical response of soft solids. *International Journal of Plasticity*, 27:1459–1470, 2011.

[41] Comsol. MEMS Module Users Guide, 2005.

[42] I.P.F. Harouche and C. Shafai. Simulation of shaped comb drive as a stepped actuator for microtweezers application. *Sensors & Actuators: A*, 123-124:540–546, 2005.

[43] A. Andreykiv and D.J. Rixen. Numerical modelling of electromechanical coupling using fictitious domain and level set methods. *International Journal for Numerical Methods in Engineering*, 80:478–506, 2009.

[44] V. Rochus, L. Van Miegroet, D.J. Rixen, and P. Duysinx. Electrostatic simulation using XFEM for conductor and dielectric interfaces. *International Journal for Numerical Methods in Engineering*, 85:1207–1226, 2011.

[45] G. Brandstetter and S. Govindjee. A high-order immersed boundary discontinuous-Galerkin method for Poisson's equation with discontinuous coefficients and singular sources. *International Journal for Numerical Methods in Engineering*, 101:847–869, 2015.

[46] A. Kovetz. *Electromagnetic Theory*. Oxford University Press, Oxford, 2000.

[47] D.J. Steigmann. On the Formulation of Balance Laws for Electromagnetic Continua. *Mathematics and Mechanics of Solids*, 14:390–402, 2010.

[48] A. Ask, A. Menzel, and M. Ristinmaa. Phenomenological modeling of viscous electrostrictive polymers. *International Journal of Non-Linear Mechanics*, 47:156–165, 2012.

[49] C. Miehe, D. Rosato, and B. Kiefer. Variational principles in dissipative electro-magneto-mechanics: A framework for the macro-modeling of functional materials. *International Journal for Numerical Methods in Engineering*, 86:1225–1276, 2011.

[50] W. Noll. On the Continuity of the Solid and Fluid States. *Indiana University Mathematics Journal*, 4:3–81, 1955.

[51] S. Rudykh and G. DeBotton. Stability of anisotropic electroactive polymers with application to layered media. *Zeitschrift fuer Angewandte Mathematik und Physik (ZAMP)*, 62:1131–1142, 2011.

[52] J. Edmiston and D.J. Steigmann. Analysis of Nonlinear Electrostatic Membranes. In R.W. Ogden and D.J. Steigmann, editors, *Mechanics and Electrodynamics of Magneto- and Electro-Elastic Materials*, pages 153–180. Springer, Udine, 2011.

[53] A.J. Lew and G.C. Buscaglia. A discontinuous-Galerkin-based immersed boundary method. *International Journal for Numerical Methods in Engineering*, 76:427–454, 2008.

[54] C.S. Peskin. Flow Patterns Around Heart Valves: A Numerical Method. *Journal of Computational Physics*, 10:252–271, 1972.

[55] C.S. Peskin. The immersed boundary method. *Acta Numerica*, 11:479–517, 2002.

[56] R.J. LeVeque and Z. Li. The Immersed Interface Method for Elliptic Equations with Discontinuous Coefficients and Singular Sources. *Journal on Numerical Analysis*, 31:1019–1044, 1994.

[57] R. Glowinski, T.-W. Pan, and J. Périaux. A fictitious domain method for Dirichlet problem and applications. *Computer Methods in Applied Mechanics and Engineering*, 111:283–303, 1994.

[58] R. Glowinski, T.-W. Pan, T.I. Hesla, D.D. Joseph, and J. Périaux. A distributed Lagrange Multiplier/Fictitious Domain Method for Flows around Moving Rigid Bodies: Application to Particulate Flow. *International Journal for Numerical Methods in Fluids*, 30:1043–1066, 1999.

[59] N. Moës, J.E. Dolbow, and T. Belytschko. A Finite Element Method for Crack Growth without Remeshing. *International Journal for Numerical Methods in Engineering*, 46:131–150, 1999.

[60] T. Belytschko and T. Black. Elastic Crack Growth in Finite Elements with Minimal Remeshing. *International Journal for Numerical Methods in Engineering*, 45:601–620, 1999.

[61] H. Ji and J.E. Dolbow. On strategies for enforcing interfacial constraints and evaluating jump conditions with the extended finite element method. *International Journal for Numerical Methods in Engineering*, 61:2508–2535, 2004.

[62] R. Rangarajan, A.J. Lew, and G.C. Buscaglia. A discontinuous-Galerkin-based immersed boundary method with non-homogeneous boundary conditions and its application to elasticity. *Computer Methods in Applied Mechanics and Engineering*, 198:1513–1534, 2009.

[63] I. Babuska. Error-Bounds for Finite Element Method. *Numerische Mathematik*, 16:322–333, 1971.

[64] N. Moës, E. Béchet, and M. Tourbier. Imposing Dirichlet boundary conditions in the extended finite element method. *International Journal for Numerical Methods in Engineering*, 67:1641–1669, 2006.

[65] E. Béchet, N. Moës, and B. Wohlmuth. A stable Lagrange multiplier space for stiff interface conditions within the extended finite element method. *International Journal for Numerical Methods in Engineering*, 78:931–954, 2009.

[66] M. Hautefeuille, C. Annavarapu, and J.E. Dolbow. Robust imposition of Dirichlet boundary conditions on embedded surfaces. *International Journal for Numerical Methods in Engineering*, 90:40–64, 2012.

[67] J. Nitsche. Über ein Variationsprinzip zur Lösung von Dirichlet-Problemen bei Verwendung von Teilräumen, die keinen Randbedingungen unterworfen sind. *Abhandlungen aus dem Mathematischen Seminar der Universität Hamburg*, 36:9–15, 1971.

[68] A. Hansbo and P. Hansbo. An unfitted finite element method, based on Nitsche's method, for elliptic interface problems. *Computer Methods in Applied Mechanics and Engineering*, 191:5537–5552, 2002.

[69] P. Heintz and P. Hansbo. Stabilized Lagrange multiplier methods for bilateral elastic contact with friction. *Computer Methods in Applied Mechanics and Engineering*, 195:4323–4333, 2006.

[70] H.M. Mourad, J.E. Dolbow, and I. Harari. A bubble-stabilized finite element method for Dirichlet constraints on embedded interfaces. *International Journal for Numerical Methods in Engineering*, 69:772–793, 2007.

[71] J.E. Dolbow and L.P. Franca. Residual-free bubbles for embedded Dirichlet problems. *Computer Methods in Applied Mechanics and Engineering*, 197:3751–3759, 2008.

[72] J.E. Dolbow and I. Harari. An efficient finite element method for embedded interface problems. *International Journal for Numerical Methods in Engineering*, 78:229–252, 2009.

[73] J. Oliver, S. Hartmann, J.C. Cante, R. Weyler, and J.A. Hernández. A contact domain method for large deformation frictional contact problems. Part 1: Theoretical basis. *Computer Methods in Applied Mechanics and Engineering*, 198:2591–2606, 2009.

[74] S. Hartmann, J. Oliver, R. Weyler, J.C. Cante, and J.A. Hernández. A contact domain method for large deformation frictional contact problems. Part 2: Numerical aspects. *Computer Methods in Applied Mechanics and Engineering*, 198:2607–2631, 2009.

[75] E. Burman and P. Hansbo. Fictitious domain finite element methods using cut elements: I. A stabilized Lagrange multiplier method. *Computer Methods in Applied Mechanics and Engineering*, 199:2680–2686, 2010.

[76] K.W. Cheng and T.-P. Fries. Higher-order XFEM for curved strong and weak discontinuities. *International Journal for Numerical Methods in Engineering*, 82:564–590, 2010.

[77] R. Gracie, H. Wang, and T. Belytschko. Blending in the extended finite element method by discontinuous Galerkin and assumed strain methods. *International Journal for Numerical Methods in Engineering*, 74:1645–1669, 2008.

[78] F.B. Hildebrand. *Advanced Calculus for Applications*. Prentice-Hall, Inc., Englewood Cliffs, N.J., 1962.

[79] J. Douglas, Jr. and T. Dupont. Interior Penalty Procedures for Elliptic and Parabolic Galerkin Methods. *Computing Methods in Applied Sciences (Second International Symposium, Versailles, 1975), Lecture Notes in Physics*, 58:207–216, 1975.

[80] M.F. Wheeler. An Elliptic Collocation-Finite Element Method with Interior Penalties. *SIAM Journal on Numerical Analysis*, 15:152–161, 1978.

[81] D.N. Arnold. An Interior Penalty Finite Element Method with Discontinuous Elements. *SIAM Journal on Numerical Analysis*, 19:742–760, 1982.

[82] F. Bassi and S. Rebay. A High-Order Accurate Discontinuous Finite Element Method for the Numerical Solution of the Compressible Navier-Stokes Equations. *Journal of Computational Physics*, 131:267–279, 1997.

[83] B. Cockburn and C.-W. Shu. The Local Discontinuous Galerkin Method for Time-Dependent Convection-Diffusion Systems. *SIAM Journal on Numerical Analysis*, 35:2440–2463, 1998.

[84] J. Peraire and P.-O. Persson. The compact discontinuous Galerkin (CDG) method for elliptic problems. *SIAM Journal on Scientific Computing*, 30:1806–1824, 2008.

[85] A. Embar, J.E. Dolbow, and I. Harari. Imposing Dirichlet boundary conditions with Nitsche's method and spline-based finite elements. *International Journal for Numerical Methods in Engineering*, 83:877–898, 2010.

[86] C. Annavarapu, M. Hautefeuille, and J.E. Dolbow. A robust Nitsche's formulation for interface problems. *Computer Methods in Applied Mechanics and Engineering*, 225-228:44–54, 2012.

[87] C. Annavarapu, M. Hautefeuille, and J.E. Dolbow. Stable imposition of stiff constraints in explicit dynamics for embedded finite element methods. *International Journal for Numerical Methods in Engineering*, 92:206–228, 2012.

[88] S.E. Mousavi and N. Sukumar. Generalized Duffy transformation for integrating vertex singularities. *Computational Mechanics*, 45:127–140, 2010.

[89] P. Laborde, J. Pommier, Y. Renard, and M. Salaün. High-order extended finite element method for cracked domains. *International Journal for Numerical Methods in Engineering*, 64:354–381, 2005.

[90] E. Béchet, H. Minnebo, N. Moës, and B. Burgardt. Improved implementation and robustness study of the X-FEM for stress analysis around cracks. *International Journal for Numerical Methods in Engineering*, 64:1033–1056, 2005.

[91] A. Johansson and M.G. Larson. A high order discontinuous Galerkin Nitsche method for elliptic problems with fictitious boundary. *Numerische Mathematik*, 123:607–628, 2013.

[92] L.D. Landau and E.M. Lifshitz. *Electrodynamics of Continuous Media*. Butterworth-Heinemann, Burlington, MA, USA, 2008.

[93] S.D.A. Hannot. *Modeling Strategies for Electro-Mechanical Microsystems with Uncertainty Quantification*. PhD thesis, TU Delft, 2010.

[94] J.C. Simo and T.A. Laursen. An Augmented Lagrangian Treatment of Contact Problems Involving Friction. *Computers and Structures*, 42:97–116, 1992.

[95] N.J. Carpenter, R.L. Taylor, and M.G. Katona. Lagrange constraints for transient finite element surface contact. *International Journal for Numerical Methods in Engineering*, 32:103–128, 1991.

[96] R.L. Taylor and P. Papadopoulos. On a finite element method for dynamic contact/impact problems. *International Journal for Numerical Methods in Engineering*, 36:2123–2140, 1993.

[97] M.W. Salveson and R.L. Taylor. Solution of Dynamic Contact Problems by Implicit/Explicit Methods. *Technical Report UCRL-CR-125780, Lawrence Livermore National Laboratory*, pages 1–22, 1996.

[98] T.A. Laursen and V. Chawla. Design of energy conserving algorithms for frictionless dynamic contact problems. *International Journal for Numerical Methods in Engineering*, 40:863–886, 1997.

[99] F. Armero and E. Petocz. Formulation and analysis of conserving algorithms for frictionless dynamic contact/impact problems. *Computer Methods in Applied Mechanics and Engineering*, 158:269–300, 1998.

[100] T.A. Laursen and G.R. Love. Improved implicit integrators for transient impact problems - geometric admissibility within the conserving framework. *International Journal for Numerical Methods in Engineering*, 53:245–274, 2002.

[101] P. Hauret and P. Le Tallec. Energy-controlling time integration methods for nonlinear elastodynamics and low-velocity impact. *Computer Methods in Applied Mechanics and Engineering*, 195:4890–4916, 2006.

[102] R. Bravo, J.L. Perez-Aparicio, and T.A. Laursen. An enhanced energy conserving time stepping algorithm for frictionless particle contacts. *International Journal for Numerical Methods in Engineering*, 85:1415–1435, 2011.

[103] O.C. Zienkiewicz, R.L. Taylor, and J.Z. Zhu. *The Finite Element Method: Its Basis and Fundamentals*. Butterworth-Heinemann, New York, 6 edition, 2005.

[104] T.J.R. Hughes. *The Finite Element Method: Linear Static and Dynamic Finite Element Analysis*. Prentice-Hall, Inc., Englewood Cliffs, N.J., 1987.

[105] T. Belytschko, R.L. Chiapetta, and H.D. Bartel. Efficient large scale non-linear transient analysis by finite elements. *International Journal for Numerical Methods in Engineering*, 10:579–596, 1976.

[106] S.D. Senturia. *Microsystem Design*. Kluwer Academic Publishers, New York, 2002.

[107] K.P.A. Saffar, N. Jamilpour, A.R. Najafi, G. Rouhi, A.R. Arshi, and A. Fereidoon. A Finite Element Model for estimating Young's Modulus of Carbon Nanotube Reinforced Composites Incorporating Elastic Cross-Links. *World Academy of Science, Engineering and Technology*, 47:219–222, 2008.

[108] A. Kis and A.K. Zettl. Nanomechanics of carbon nanotubes. *Philosophical Transactions of the Royal Society A*, 366:1591–1611, 2008.

[109] F. Armero. Assumed Strain in Finite Element Methods. In L.P. Franca, T.E. Tezduyar, and A. Masud, editors, *Finite Element Methods: 1970's and Beyond*, pages 46–61. CIMNE, Barcelona, Spain, 2004.

[110] J.W. Demmel. *Applied Numerical Linear Algebra*. SIAM Society for Industrial and Applied Mathematics, Philadelphia, 1997.

[111] D.M. Ambrose and J. Wilkening. Computing Time-Periodic Solutions of Nonlinear Systems of Partial Differential Equations. In *Proceedings of Hyperbolic Problems: Theory, Numerics, and Applications. Beijing, China, 2010*, pages 237–280. Higher Education Press, 2012.

[112] S. Govindjee, T. Potter, and J. Wilkening. Cyclic steady states of treaded rolling bodies. *International Journal for Numerical Methods in Engineering*, 99:203–220, 2014.

[113] D.A. Knoll and D.E. Keyes. Jacobian-free Newton-Krylov methods: a survey of approaches and applications. *Journal of Computational Physics*, 193:357–397, 2004.

[114] G.L. Goudreau and R.L. Taylor. Evaluation of Numerical Methods in Elastodynamics. *Computer Methods in Applied Mechanics and Engineering*, 2:69–97, 1972.

[115] G. Beer, I. Smith, and C. Duenser. *The Boundary Element Method with Programming*. Springer Verlag, Wien, 2008.

Appendix A

Far Field Boundary Condition via Boundary Element Method

We briefly outline our approach to the far field boundary condition we employ at the boundary of the computational domain of interest. To this end we use the boundary element method which relies upon the boundary integral equation, for each $\mathbf{x}_i \in \mathcal{W}$,

$$c\,\Phi_{\mathcal{W}}(\mathbf{x}_i) - \int_{\partial\mathcal{W}} \Phi_{\mathcal{W}} q^*_{\mathcal{W}} \mathrm{da} = -\int_{\partial\mathcal{W}} q_{\mathcal{W}} \Phi^*_{\mathcal{W}} \mathrm{da}\,, \tag{A.1}$$

where

$$\Phi^*_{\mathcal{W}} = \begin{cases} \frac{1}{2\pi\epsilon_{\mathcal{W}}} \ln\frac{1}{r}\,, & \text{in 2D}\,, \\ \frac{1}{4\pi\epsilon_{\mathcal{W}} r}\,, & \text{in 3D}\,, \end{cases} \tag{A.2}$$

with $r = \|\mathbf{x} - \mathbf{x}_i\|$, $q^*_{\mathcal{W}} = -\epsilon_{\mathcal{W}} \nabla\Phi^*_{\mathcal{W}} \cdot \mathbf{n}_{\mathcal{W}}$ and c being a constant depending on the location of the collocation point $\mathbf{x}_i$. If $\mathbf{x}_i$ is inside $\mathcal{W}$, then $c = 1$. If $\mathbf{x}_i$ is on $\partial\mathcal{W}$, then c depends on the smoothness of the boundary (see e.g. [115, p.107])– for a smooth boundary one has $c = 0.5$.

We consider the discretization of the boundary integral equation (A.1). In this context we will use a point collocation method where we assume that (A.1) holds strongly for $\mathbf{x}_i$ at all nodal points of the mesh $\partial\mathcal{W}^h$. This results in

$$[\Delta\mathbf{Q}]\,\tilde{\mathbf{\Phi}}_{\mathcal{W}} = [\Delta\mathbf{\Phi}]\,\tilde{\mathbf{q}}_{\mathcal{W}}\,, \tag{A.3}$$

where the i-th row corresponds to collocation point $\mathbf{x}_i$:

$$[\Delta\mathbf{Q}]_{i,:}\,\tilde{\mathbf{\Phi}}_{\mathcal{W}} = c\,\tilde{\Phi}_{\mathcal{W}i} - \sum_e \left[\int_{\partial\mathcal{W}_e} q^*_{\mathcal{W}}(\mathbf{x}_i, \xi)\tilde{\mathbf{N}}_e(\xi)\mathrm{da}(\xi)\right] \tilde{\mathbf{\Phi}}_{\mathcal{W}e} \tag{A.4}$$

$$[\Delta\mathbf{\Phi}]_{i,:}\,\tilde{\mathbf{q}}_{\mathcal{W}} = -\sum_e \left[\int_{\partial\mathcal{W}_e} \Phi^*_{\mathcal{W}}(\mathbf{x}_i, \xi)\tilde{\mathbf{N}}_e(\xi)\mathrm{da}(\xi)\right] \tilde{\mathbf{q}}_{\mathcal{W}e}\,, \tag{A.5}$$

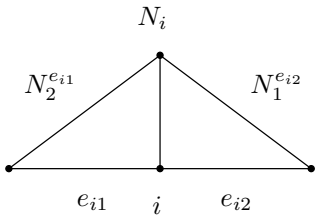

Figure A.1: Coupling finite element and boundary element method.

and $\tilde{\mathbf{N}}_e(\xi)$ are standard shape function matrices. Note the notation (e.g. 2D)

$$\Phi^*_{\mathcal{W}}(\mathbf{x}_i, \xi) = \frac{1}{2\pi\epsilon_{\mathcal{W}}} \ln \frac{1}{\|\mathbf{x}(\xi) - \mathbf{x}_i\|}\,, \tag{A.6}$$

where ξ is the integration parameter such that $\mathbf{x}(\xi)$ maps to the element integration domain. The matrices $[\Delta\mathbf{Q}]$, $[\Delta\mathbf{\Phi}]$ are fully populated. We highlight three facts: First, the integrals involve singular functions and special care must be taken in order to evaluate them correctly via numerical Gauss or modified Gauss quadrature rules (see [115, p.139]). Second, note that the diagonal terms of $[\Delta\mathbf{Q}]$ can be easily obtained by summing up all other coefficients in the corresponding row and changing the sign ([115, p.135], rigid body motion argument); this saves us a strongly singular integration plus the computation of the factor c. And lastly, note that for an infinite domain one must consider the so called *azimuthal integral*, that is the integration over the (semi-)sphere with infinite radius ([115, p.136]). This will only give a contribution to the strongly singular integral; i.e. the diagonal terms of $[\Delta\mathbf{Q}]$. In the case of an infinite domain this requires one to add $+1$ to the diagonal, whereas in the semi-infinite case one adds $+0.5$.

In our experience the piecewise constant boundary element discretization performs satisfactorily and is particularly easy to implement. We assume that the BE-nodes are in the middle of each surface patch, and that the constant potential equals the average of the attached domain mesh interpolation. Using constant elements allows for an analytical integration of the singular integrals. In particular note that $[\Delta\mathbf{Q}]_{i,i} = 1.5$ as arising from the azimuthal integral, whereas the strongly singular integral vanishes in this case. Moreover

$$[\Delta\mathbf{\Phi}]_{i,i} = -\int_{\Gamma_{BEi}} \Phi^*_{\mathcal{W}}(\mathbf{x}_i, \xi)\mathrm{da}(\xi) = -2\int_0^{l/2} \frac{1}{2\pi\epsilon_{\mathcal{W}}} \ln\frac{1}{\xi}\mathrm{d}\xi = -\frac{l}{2\pi\epsilon_{\mathcal{W}}}\left[\ln\frac{2}{l} + 1\right]\,, \tag{A.7}$$

where l is the length of the boundary element. For the off-diagonal terms, a standard 4-point Gauss quadrature is used.

We couple the boundary elements to the standard finite elements as in [115, Ch.16]. One can write (A.3) as

$$\tilde{\mathbf{q}}_{\mathcal{W}} = \tilde{\mathbf{K}}_{BE}\tilde{\mathbf{\Phi}}_{\mathcal{W}}\,, \tag{A.8}$$

featuring the 'pseudo'-stiffness matrix

$$\tilde{\mathbf{K}}_{BE} = [\tilde{\mathbf{q}}_1, \tilde{\mathbf{q}}_2, \ldots, \tilde{\mathbf{q}}_{N_b}]\,, \tag{A.9}$$

where $\tilde{\mathbf{q}}_i$ is the solution to

$$[\Delta\mathbf{\Phi}]\,\tilde{\mathbf{q}}_i = [\Delta\mathbf{Q}]_{:,i}\,, \tag{A.10}$$

with $[\Delta\mathbf{Q}]_{:,i}$ being the i-th column of the matrix $[\Delta\mathbf{Q}]$. In order to obtain an expression for the finite element flux vector $\mathbf{f}_{BE}$, we note that $q_{\mathcal{V}} = -q_{\mathcal{W}}$ along Γ_{BE}. Thus one can write the equivalent nodal flux at Node i as

$$f_{BEi} = -\sum_{\{e_i\}}\sum_{n=1}^{nbe}\left[\int_{\partial\mathcal{V}_{e_i}\cap\Gamma_{BE}} N_j^{e_i}\tilde{N}_n^{be(e_i)}\mathrm{da}\right]\tilde{q}_{\mathcal{W}n}^{be(e_i)}\,, \tag{A.11}$$

where $\{e_i\}$ ranges over the adjacent elements of node i, $be(e_i)$ is the boundary element number corresponding to the adjacent finite element e_i, and one takes the local finite element shape function $N_j^{e_i}$ associated with the j-th node in the element numbering which corresponds to the i-th global node (see Fig. A.1). We write (A.11) as

$$\mathbf{f}_{BE} = -\mathbf{N}\tilde{\mathbf{q}}_{\mathcal{W}}\,. \tag{A.12}$$

Finally $\mathbf{\Phi}_{\mathcal{W}} = \mathbf{\Phi}_{\mathcal{V}}$, and we use the projection $\mathbb{P}$, such that

$$\tilde{\mathbf{\Phi}}_{\mathcal{W}} = \mathbb{P}\mathbf{\Phi}_{\mathcal{W}}\,, \tag{A.13}$$

relates the BE interpolation to the FE nodal values. We summarize

$$\mathbf{f}_{BE} = -\mathbf{N}\tilde{\mathbf{K}}_{BE}\mathbb{P}\mathbf{\Phi}_{\mathcal{V}} = -\mathbf{K}_{BE}\mathbf{\Phi}_{\mathcal{V}}\,, \tag{A.14}$$

where

$$\mathbf{K}_{BE} = \mathbf{N}\tilde{\mathbf{K}}_{BE}\mathbb{P} \tag{A.15}$$

is the boundary element stiffness (non-symmetric).

Appendix B

Dynamical Impact

Further details on the dynamic contact treatment in this study are discussed here. We limit ourselves to frictionless contact, and a node-to-rigid-surface contact driver. For illustration, let us look at Fig. B.1(a), where the gap function at a node A becomes

$$g_A = (\mathbf{x}_A - \bar{\mathbf{x}}) \cdot \bar{\mathbf{n}}\,, \tag{B.1}$$

and we find $\bar{\mathbf{x}}$ such that

$$||\mathbf{x}_A - \bar{\mathbf{x}}|| = \min_{\mathbf{x}\in\Gamma_{master}} ||\mathbf{x}_A - \mathbf{x}|| \tag{B.2}$$

is the minimum distance of the slave node $\mathbf{x}_A$ to the boundary Γ_{master}. By differentiation, and noting that $\dot{\mathbf{n}} \cdot (\mathbf{x}_A - \bar{\mathbf{x}}) = 0$, we have

$$\dot{g}_A = (\dot{\mathbf{x}}_A - \dot{\bar{\mathbf{x}}}) \cdot \bar{\mathbf{n}}\,, \tag{B.3}$$

which is the gap-rate at a node A. As mentioned before, in order to ensure (4.21) and (4.22) in the implicit setting, we use a penalty method with the penalty potential U given by (4.34). In a naive way, one is tempted to calculate the contact pressure $p_{n+1/2}$ at $t = t_{n+1/2}$ as $p_{n+1/2} = -U'(g_{n+1/2})$, where $g_{n+1/2} = g(\mathbf{x}(t_{n+1/2}))$. As is well known, such a choice may result in an energy increase or loss during impact that renders the solution meaningless. Following [99], we advocate an alternative scheme in combination with the mid-point rule, where the contact pressure $p_{A,n+1/2}$ for node A at $t = t_{n+1/2}$ is calculated by

$$p_{A,n+1/2} = \begin{cases} -\frac{U(g_{A,n+1}) - U(g_{A,n})}{g_{A,n+1} - g_{A,n}}\,, & \text{if } g_{A,n+1} \neq g_{A,n}\,, \\ -U'\left(\frac{1}{2}(g_{A,n} + g_{A,n+1})\right)\,, & \text{otherwise}\,, \end{cases} \tag{B.4}$$

as in (4.35). This scheme will ensure energy conservation upon release of the impacting body, as will be observed in the upcoming example. Note that the use of the real gap function g_A in this setting is applicable as the rigid surface is fixed in space. We refer to [99] for further details of the formulation– in particular, when two *elastic* bodies are in contact.

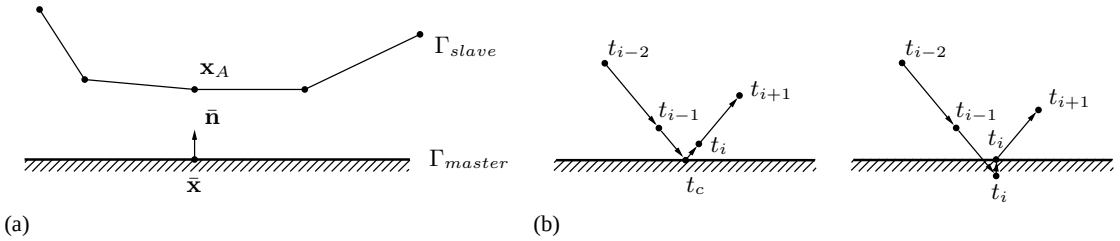

Figure B.1: Node-to-rigid-surface contact: (a) master and slave segments; (b) approximation of time-impact resolution for the explicit contact predictor-corrector scheme [5].

In the explicit case, the impact-time t_c is approximated as sketched in Fig. B.1(b): the equations of motion are advanced for one step $(t_{i-1}, t_i^-]$ by a predictor-step without consideration of contact. In the case of penetration, one projects all penetrating nodes of the slave-surface to the master-facets by a closest-point projection: $\mathbf{x}_{t_i^-} \to \mathbf{x}_{t_i}$, where $\mathbf{x}_{t_i}$ are the projected nodal positions. Subsequently, as outlined in Alg. 4.3, the post-impact velocities of penetrating nodes are found such that the gap rate $\dot{g}_A = 0$ according to (B.3) for all contacting nodes A. The direct enforcement of the Kuhn-Tucker constraint (4.21) and persistency condition (4.22) can be done in our case as the position of the rigid surface is assumed to be fixed. Whenever two *elastic* bodies are in contact, a method that takes into account the momentum conservation must be employed as done in [5].

We illustrate the performance of the dynamical contact algorithms for a disk-impact example under conservative loading. Consider a disk subject to a constant body-force g as sketched in Fig. B.2(top, left). For the benchmark example we use a plane stress nonlinear Neo-Hookean material model as derived from (2.41) featuring $E = 17'900$ GPa, $\nu = 0.31$, $\rho = 8.9$ g/cm^3, and a disk radius of $R = 70$ μm. For the finite element model we use 108 quadrilateral elements and a bi-linear interpolation. The initial gap to contact is 12 nm, and the external force is $4 \cdot 10^{12}$ m/s^2. The elastic modulus and external force are non-physical, and only serve us to test the numerical method under extreme conditions. For the implicit method we employ a penalty parameter $\kappa_p = 3 \cdot 10^{12}$. The explicit method does not require any parameter, whereas the penalty parameter as used in the implicit version has noticeable effects on the penetration and has to be adjusted by the user for a given problem. The explicit formulation, in contrast, requires a bound on the maximum allowable time-step following (4.40). In our example we use $\Delta t_n = 0.167$ ns for both methods, whereas the implicit method is stable and accurate with much bigger time-steps. By looking at the results in Fig. B.2(bottom, left), we monitor the vertical displacement of the bottom disk-node over the normalized time $t/33$ ns for 200 time-steps. As the disk bounces into the rigid foundation, both methods enforce nicely the geometric constraint until the disk lifts back off. For the implicit method we notice slight oscillations during persistent contact. The total energy is well preserved [Fig. B.2(top, right)], and only a minimal loss in energy ($< 1\%$) [Fig. B.2(bottom, right)] during impact occurs for both methods. Note that the implicit method restores all energy upon release, which is a typical feature of the method proposed

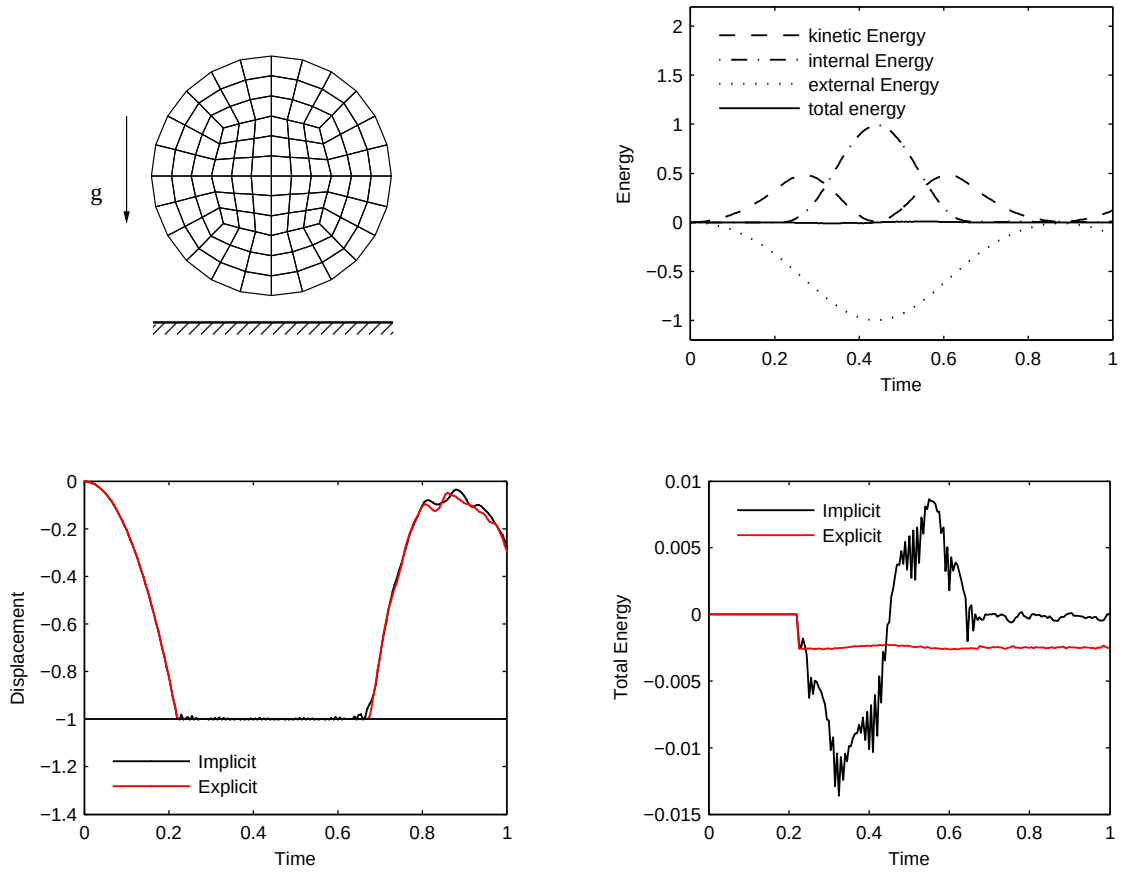

Figure B.2: Disk impact example.

by [99] (see also the discussion in [102]). As the disk impacts into the rigid foundation, a shock wave is introduced and will persist due to reflections at the domain boundary as we have no damping added to the system. We observe some small vibrations of the disk upon release, which results in an incomplete recovering of the initial state, due to the conversion of the potential energy into internal energy.